University of California

Los Angeles

# Polarimetry at the Brookhaven AGS Using Proton-Carbon Coulomb-Nuclear Interference

A dissertation submitted in partial satisfaction

of the requirements for the degree

Doctor of Philosophy in Physics

by

**Jeffery James Wood**

2005

The dissertation of Jeffery James Wood is approved.

Huan Z. Huang

George Igo

Ronald Miech

Bernard Nefkens

Charles Whitten, Jr., Committee Chair

University of California, Los Angeles

2005

*To Mom and Dad*

*You made me truly believe I can achieve anything which I set my mind to.*

# Table of Contents

# List of Figures

# List of Tables

# Acknowledgments

I was very fortunate to receive much help and support from so many people during my graduate education. It would be difficult to name them all here, but I sincerely appreciate the efforts of all who contributed to this work. That being said, there are a few people and groups that I would like to explicitly recognize. First, I would like to thank my adviser Chuck Whitten. I really enjoyed our interaction, and I cannot imagine there being a better adviser for me. I want to thank George Igo for his candid advice and for first suggesting that I join the CNI Polarimetry Group. In addition, I would like to thank all present and past members of the UCLA Igo-Whitten-Huang research group. Comments and suggestions from group members have been invaluable. My office mates have dispensed their knowledge to me and also helped keep my spirits high. All the members of the UCLA group have contributed to creating a constructive learning environment and support system without which I would have been lost.

I would like to thank all the members of the CNI Polarimetry Group. Thank you for letting me be a part of your team. I enjoyed working with you all. I specifically want to thank Alessandro Bravar. I learned a great deal from working with you. Many thanks go to members of Brookhaven's Collider-Accelerator Division (C-AD). I want thank Haixin Huang and rest of the AGS accelerator physicists. I would like to recognize the work of several groups within C-AD: the vacuum support group for keeping us up and running and safe, the operations group for helping to run our polarimeter, and the controls group for helping with software development. Thanks go to the UCLA machine shop. I appreciate the support I received from members of the STAR collaboration, particularly members of the Spin Physics Working Group. Also, thank you to the members

of the BNL Instrumentation Division who helped design, produce, and prepare our detectors and electronics.

Finally, I am thankful for the tremendous support and inspiration from my family, particularly from my parents, Lynn and Tony; my brother, Brian; and my sister, Andrea. Stacey Tierney thank you for your love and encouragement. I have so many friends I would like to thank for helping me keep things in perspective. I am very lucky to have been surrounded by such a wonderful group of colleagues, family, and friends. Thank you all.

# Vita

| | |
|---|---|
| 4 Oct. 1976 | Born, Ft. Wayne, Indiana, USA. |
| 1999 | B.A. Physics and Mathematics<br>Indiana University<br>Bloomington, IN |
| 1999 - 2000 | Teaching Assistant<br>Department of Physics<br>University of California Los Angeles |
| 2001 | M.S. Physics<br>University of California Los Angeles<br>Los Angeles, CA |
| 2000 - 2005 | Graduate Research Assistant<br>Intermediate Energy Physics and Relativistic Heavy Ion Group<br>University of California Los Angeles |

# Presentations

J.Wood, CNI Polarimetry for the RHIC Spin Program, *American Physical Society-East Lansing, Michigan*, 2002.

J.Wood, CNI Polarimetry at RHIC Update, *American Physical Society-Tucson, Arizona*, 2003.

Abstract of the Dissertation

# Polarimetry at the Brookhaven AGS Using Proton-Carbon Coulomb-Nuclear Interference

by

**Jeffery James Wood**

Doctor of Philosophy in Physics

University of California, Los Angeles, 2005

Professor Charles Whitten, Jr., Chair

A program to study the spin structure of the proton at the Relativistic Heavy Ion Collider (RHIC) requires a fast, reliable method of measuring beam polarization. One method of polarimetry used at RHIC measures asymmetries from $pC$ elastic scattering at very low momentum transfer, $-t$, in the Coulomb-Nuclear Interference (CNI) region. Progress of the RHIC Spin Program had been limited by low beam polarization production from the Alternating Gradient Synchrotron (AGS), the injector for RHIC. In 2003 a $pC$ CNI polarimeter was installed in the AGS to provide vital diagnostics needed to minimize depolarization effects. This polarimeter is a powerful tool for studying spin dynamics during acceleration and characterizing polarization losses at specific beam energies. The $-t$ dependence of the analyzing power of the $pC$ CNI process has also been studied at a number of beam energies in the AGS. A description of the AGS $pC$ CNI polarimeter as well as polarization and analyzing power measurement results are presented.

# CHAPTER 1

# Introduction

## 1.1 Overview of the RHIC Spin Program

The nonintuitive nature of proton spin makes for an intriguing area of study in physics. We recognize that the proton is composed of quarks, antiquarks and gluons, and all properties of the proton must somehow be built up from these components. Intuition suggests that the proton spin be predominately carried by its three valence quarks. However, a series of deep inelastic scattering experiments in the 1980s and 1990s have provided surprising results regarding the spin structure of the proton. Only a fraction of the proton spin is carried by the quarks and antiquarks [1]. The spin of the proton must therefore be mainly carried by the gluons and/or orbital angular momentum. This surprising result has motivated the foundation of an experimental program to further our knowledge of proton spin.

The Relativistic Heavy Ion Collider (RHIC) at Brookhaven National Laboratory provides a unique environment for the study of proton spin. RHIC consists of two synchrotron accelerator rings, referred to as the blue ring and the yellow ring. The design goals for RHIC are to collide 70% polarized proton beams at energies up to $\sqrt{s} = 500$ GeV and luminosity of $\mathcal{L} = 2 \times 10^{32}\text{cm}^{-2}\text{s}^{-1}$. The two large detectors at RHIC, STAR and PHENIX, are committed to pursuing the

proton spin program. These experiments will measure asymmetries in the production of photons, jets, and $W$ and $Z$ bosons. These measurements will provide information about the spin-dependent gluon density functions as well as flavor sensitive polarized quark and antiquark distributions. Significant progress toward these experimental goals has already been made during the first three polarized proton runs at RHIC. However, definitive measurements have been hindered by low beam polarization and low integrated luminosity.

At the STAR and PHENIX detectors, asymmetries can be measured for any combination of one or both beams polarized either transversely or longitudinally. The single spin transverse asymmetry, $A_N$ defined below, can be measured by colliding a transversely polarized beam with an unpolarized beam.

$$A_N = \frac{1}{P}\frac{N_\uparrow - N_\downarrow}{N_\uparrow + N_\downarrow}, \tag{1.1}$$

where $N_\uparrow$ and $N_\downarrow$ are the number of observed events with the beam transversely polarized up and down. $P$ is the beam polarization. In practice, both circulating beams are polarized with an alternating pattern of spin direction up and spin direction down proton bunches. A single spin asymmetry can then be studied by summing yields from both spin states for one of the beams. By measuring a known single spin asymmetry specific beam polarization at an experimental interaction region can be monitored.

For measurements probing the spin structure of the proton, longitudinal polarization is required. The parity violating asymmetry, $A_L$, that compares production from the two helicity states of one longitudinally polarized beam is defined below:

$$A_L = \frac{1}{P}\frac{N_+ - N_-}{N_+ + N_-}. \tag{1.2}$$

$N_+$ and $N_-$ represent the number of observed events with the polarized proton beam in the + and - helicity states. $P$ is again the beam polarization. Knowledge of the beam polarization is essential for doing these asymmetry measurements. Also, a large beam polarization is preferable. The statistical uncertainty of $A_L$ is proportional to $1/\sqrt{N_+ + N_-}$ and to $1/P$. At RHIC the design goal is to achieve a 70% polarized beam. A lower beam polarization would require a longer running time to achieve the same statistical uncertainty. This effect is amplified for the two-spin asymmetry, $A_{LL}$, where both beams are polarized.

$$A_{LL} = \frac{1}{P_1 P_2} \frac{(N_{++} + N_{--}) - (N_{+-} + N_{-+})}{(N_{++} + N_{--}) + (N_{+-} + N_{-+})}, \tag{1.3}$$

where $N_{+-}$ represents the number of observed events with the first beam in the + helicity state and the second beam in the - helicity state. The statistical uncertainty of $A_{LL}$ is approximately given by $1/(P_1 P_2) \times 1/\sqrt{N}$ where $N$ is the total number of observed events.

## 1.2 Polarimetry for the RHIC Spin Program

A reliable method of measuring beam polarization is essential to the success of the RHIC spin program. Some of the desirable polarimetry characteristics are discussed below. A method of polarimetry that provides measurements rapidly is preferred. Rapid measurements are needed at RHIC in order to monitor polarization fluctuations over time and under different running conditions. If rapid measurements are desired, then the polarimetry process must have a high event rate. This allows a small statistical uncertainty to be achieved in a short measurement time. Also, a process with a larger asymmetry is preferred to one with a lesser asymmetry. A larger asymmetry process will have a smaller relative sta-

tistical uncertainty than a smaller asymmetry for the same number of measured events. An ideal process for polarimetry would have a high rate process as well as a large asymmetry.

Another important consideration in choosing a polarimetry technique is the feasibility of the method. The ability to translate a measured quantity into a meaningful polarization value is essential. For a transversely polarized beam on an unpolarized target, the beam polarization is given by $P = \varepsilon/A_N$, where $\varepsilon$ is the measured left-right asymmetry. In order to obtain polarization information from such a process, $A_N$, also known as the analyzing power, must be known from either calculation or previous measurements. The method of polarimetry must also be doable in the experimental environment at RHIC. Any process that could cause significant degradation to the proton beam should be avoided as this could effect accelerator performance and any subsequent experimental measurements. So, making a measurement and translating the result into polarization must be feasible for a useful polarimetry technique.

The method of polarimetry used at RHIC is based on proton-carbon, $pC$, elastic scattering at very low momentum transfer squared, $-t$, in the Coulomb-Nuclear Interference (CNI) region. A thin ($\sim 5\mu\text{g/cm}^2$) carbon target is inserted into the circulating polarized proton beam. Recoil carbon nuclei near 90° from elastic scattering are detected with silicon detectors, and a left-right asymmetry is calculated. The analyzing power for $pC$ elastic scattering has been measured in experiment E950 for a beam energy of 21.7 GeV [2]. The measured analyzing power from E950 is shown in Figure 1.1. The analyzing power is not particularly large but has a reasonable value of a few percent. One major advantage of this technique is the large cross section for $pC$ elastic scattering in the CNI region. This allows for polarization measurements with a high degree of statistical accu-

racy over a relatively short time interval. For the 2003 run with typically $4 \times 10^{12}$ protons in each RHIC ring, the CNI polarimeters collected $2 \times 10^{7}$ recoil carbons in about 20 seconds [3]. This short measurement time was sufficient to achieve a reasonable statistically uncertainty of $< 10\%$. Brief measurement times help to limit the time that carbon target is inserted into the proton beam. Insertion of the target has been observed to result in small levels of beam degradation, *i.e.* beam emittance growth and loss of luminosity. To summarize, $pC$ CNI elastic scattering has a moderately sized analyzing power, a large event rate and limited beam degradation. These traits make this technique a useful method of polarimetry. There is, however, a large relative error of $\pm 30\%$ due to uncertainty in the E950 analyzing power measurement.

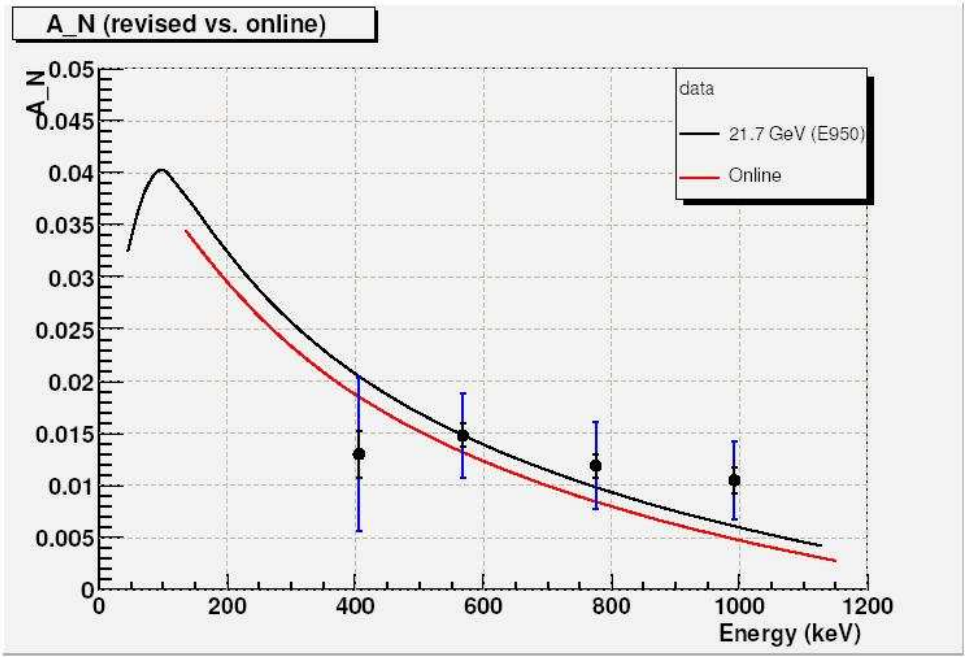


Figure 1.1: Analyzing power for proton-carbon elastic scattering for 21.7 GeV protons versus recoil carbon energy. The points with error bars are data from the E950 experiment. The two curves are fits to the data by L. Trueman [4]. The lower curve is an early fit, which was used to calibrate the RHIC CNI polarimeters during 2003. The upper curve is a revised fit used for 2004 data.

The uncertainty in the polarization measurements contribute to the overall systematic scale uncertainty of all the spin-dependent experimental measurements at RHIC. The asymmetry measurements probing the spin structure of the proton require more accurate polarization values than the CNI method can currently provide. This problem has been addressed by the installation of a polarized hydrogen jet target polarimeter at the RHIC. With the polarized $H$ jet polarimeter, absolute beam polarization is expected to be measured within $\pm 5\%$. This polarimeter will also provide an absolute calibration of the CNI polarimeters installed in each of the RHIC rings. At the time of writing this document, the polarized $H$ jet polarimeter has taken its first data, but the analysis to provide a calibration of $A_N$ for the CNI polarimeters is not complete.

In addition to the practical issue of polarimetry, the $pC$ CNI polarimeters also provide information about the spin dependence of hadronic interactions. The spin-dependent hadronic contribution to $pC$ elastic scattering can be inferred from the shape of the analyzing power $-t$ dependence. The E950 experiment measured a nonzero spin-dependent hadronic contribution at a beam momentum of 21.7 GeV/$c$. The AGS $pC$ CNI polarimeter can measure the analyzing power at 21.7 GeV/$c$ (as well as several other beam momenta in the AGS range). In doing so the AGS $pC$ CNI polarimeter can confirm the E950 measurement and improve on the accuracy. The measurement of a spin-dependent hadronic contribution to $pC$ elastic scattering could have important consequences on the quark structure of the nucleon. For example, a spin-dependent hadronic contribution non-vanishing at high beam energies is consistent with models proposing the existence of diquarks inside the nucleon [5].

## 1.3 Thesis Arrangement

The CNI polarimeters in RHIC have been in operation since December 2001. During the first polarized proton collision running period, the CNI polarimeters measured an average of 11% (16%) polarization in the blue (yellow) ring after accelerating the beam to 100 GeV [6]. This is well below the design goal of 70% polarization. The polarized proton source typically produces beams of about 70-80% polarization. Therefore, the beam must become depolarized during the transport and acceleration to the top energy in RHIC. The polarization loss during the acceleration in RHIC is expected to be small. Much of the polarization loss is expected to occur during an earlier acceleration stage in the injector to RHIC, the Alternating Gradient Synchrotron (AGS). A CNI polarimeter was installed in the AGS in October 2002 with the goal of improving the diagnostics and ultimately increasing the polarization output to RHIC. The polarization output from the AGS has already improved significantly from the first polarized proton run and further improvement is expected.

This thesis describes the details of the experimental setup and the measurement results of the AGS CNI polarimeter. The formalism to describe the elastic scattering of a polarized proton beam from a carbon target is defined in Chapter 2. Theoretical expectations of the analyzing power for this process are also discussed. In Chapter 3 the production and transport of polarized proton beams at the RHIC facility are described. Beam depolarization conditions and techniques to avoid them are explored as well. The set up of hardware and the data acquisition system is discussed in Chapter 4. Chapter 5 explains the analysis methods used to extract asymmetries from the data. Results from measurements and conclusions are presented in Chapters 6 and 7.

# CHAPTER 2

# Formalism and Theory

## 2.1 Hadronic Scattering Formalism

The CNI polarimetry method makes use of proton-carbon elastic scattering at low momentum transfer. The asymmetry from this process depends on the interference of the spin-dependent electromagnetic interaction (dominated by the one-photon exchange) and the spin-independent hadronic interaction. The dominant contribution from the electromagnetic interaction is calculable, and the hadronic contribution can be determined from the total cross section. This description of the process is valid assuming there is no spin-dependent hadronic contribution, that is to say there is no hadronic spin-flip amplitude. However, a nonzero hadronic spin-flip amplitude has been observed for proton-carbon elastic scattering in the E950 experiment [2]. In this chapter the relation of the hadronic spin-flip amplitude to the experimentally observable analyzing power, $A_N$, is described.

The formal framework used to describe proton-carbon elastic scattering in the CNI region of low momentum transfer is developed. The helicity amplitude formalism [7] is used to provide a general description of the elastic scattering of hadrons and the associated experimental observables. Of particular interest for this process is the contribution of the spin-flip amplitude from the hadronic

interaction. High-energy hadronic interactions at low momentum transfers have been successfully described using the phenomenology of Regge pole exchange [8]. Using this framework the expectations and implications of a nonzero hadronic spin-flip amplitude are developed.

Reasonably sized analyzing powers of a few percent have been measured for proton-proton [9] and proton-carbon [2] elastic scattering at small momentum transfer of $10^{-3} < -t < 10^{-2}(\mathrm{GeV}/c)^2$. The analyzing power is defined as the left-right asymmetry of the cross sections in the scattering plane normal to the beam polarization,

$$A_N = \frac{\sigma_L^{\uparrow} - \sigma_R^{\uparrow}}{\sigma_L^{\uparrow} + \sigma_R^{\uparrow}}, \tag{2.1}$$

where $\sigma_{L(R)}^{\uparrow}$ is the cross section for the scattering to the left (right) of the beam axis with polarization in the up direction. This analyzing power is predominately caused by the interference between the electromagnetic (Coulomb) spin-flip amplitude and the hadronic (nuclear) non-flip amplitude. The spin-dependent contribution to the hadronic interaction can be extracted from the shape of the analyzing power versus $-t$. A nonzero spin-dependent hadronic contribution at high energies carries important implications for the structure of the nucleon. For $pp$ scattering the analyzing power has been measured at high energies [9]. An explicit expression for the $pp$ analyzing power and the results of this measurement are presented in Section 2.2. The E950 experiment measured a nonzero spin-dependent hadronic contribution at a medium-high energy in the AGS. An expression for $A_N$ for $pC$ elastic scattering is developed and the E950 results are discussed in Section 2.3.

## 2.2 Proton-Proton Elastic Scattering

For the case of $pp$ elastic scattering five independent helicity amplitudes are necessary to describe the interaction [10]:

$$\begin{aligned}
\phi_1 &= \langle ++ \mid \mathcal{T} \mid ++ \rangle, \\
\phi_2 &= \langle ++ \mid \mathcal{T} \mid -- \rangle, \\
\phi_3 &= \langle +- \mid \mathcal{T} \mid +- \rangle, \\
\phi_4 &= \langle +- \mid \mathcal{T} \mid -+ \rangle, \\
\phi_5 &= \langle ++ \mid \mathcal{T} \mid +- \rangle,
\end{aligned} \tag{2.2}$$

where $|\lambda_A \lambda_B\rangle$ ($\lambda_{A,B} = +, -$) is the two particle helicity state in the center-of-mass system. $\mathcal{T}$ is a matrix operator dependent on the Mandelstam variables $s$ and $t$. In the notation of Jacob and Wick [11], $\mathcal{T}$ is related to $\mathcal{S}$, the transformation matrix of the interaction, by $\mathcal{S} = 1 + i\mathcal{T}$. The $\phi_1$ and $\phi_3$ are non-flip amplitudes. The $\phi_2$ and $\phi_4$ are double spin-flip amplitudes, and $\phi_5$ is the single spin-flip amplitude. In terms of these amplitudes, the differential cross section, $d\sigma_{pp}/dt$, and the analyzing power, $A_N^{pp}$ can be written:

$$\frac{d\sigma_{pp}}{dt} = \frac{2\pi}{s(s-4m_p^2)}\Big[|\phi_1|^2 + |\phi_2|^2 + |\phi_3|^2 + |\phi_4|^2 + 4|\phi_5|^2\Big], \tag{2.3}$$

$$\frac{d\sigma_{pp}}{dt} A_N^{pp} = -\frac{4\pi}{s(s-4m_p^2)} \mathrm{Im}\Big[(\phi_1 + \phi_2 + \phi_3 - \phi_4)\phi_5^*\Big], \tag{2.4}$$

where $m_p$ is the mass of the proton.

The helicity amplitudes in Equation 2.2 each depend on contributions from both electromagnetic and hadronic interactions. In order to establish the dependence of $A_N^{pp}$ on the hadronic spin-flip amplitude, each amplitude, $\phi_j$ ($j$ = 1-5),

can be decomposed into electromagnetic, $\phi_j^{\rm em}$, and hadronic, $\phi_j^{\rm h}$, parts.

$$\phi_j = \phi_j^{\rm em} + e^{-i\delta_{pp}}\phi_j^{\rm h}. \tag{2.5}$$

The $\delta_{pp}$ is the relative phase between $\phi_j^{\rm em}$ and $\phi_j^{\rm h}$ called the Coulomb phase[1].

The spin dependence of the hadronic amplitude is characterized by the ratio of the spin-flip to the non-flip amplitude. This ratio is usually referred to as the hadronic spin-flip amplitude, $r_5$, and is defined by

$$r_5 = \frac{m_p}{\sqrt{-t}}\frac{\phi_5^{\rm h}}{{\rm Im}\,\phi_+^{\rm h}}, \tag{2.6}$$

$$\phi_+^{\rm h} = \frac{\phi_1^{\rm h} + \phi_3^{\rm h}}{2} \tag{2.7}$$

where $\phi_+^{\rm h}$ is the averaged hadronic non-flip amplitude. For convenience in expressing $A_N^{pp}$, the total cross section, $\sigma_{\rm tot}^{pp}$, is related to $\phi_+^{\rm h}$ at the forward angle (*i.e.* at $t = 0$) via the optical theorem

$$\sigma_{\rm tot}^{pp} = \frac{8\pi}{[s(s-4m_p^2)]^{1/2}}{\rm Im}\,\phi_+^{\rm h}\mid_{t=0}\,. \tag{2.8}$$

Also for convenience, the parameter $\rho_{pp}$ is defined

$$\rho_{pp} = \frac{{\rm Re}\,\phi_+^{\rm h}\mid_{t=0}}{{\rm Im}\,\phi_+^{\rm h}\mid_{t=0}}. \tag{2.9}$$

The analyzing power, $A_N^{pp}$, for $pp$ elastic scattering, as expressed by Buttimore

[1]See Reference [12] by Cahn for an explicit expression for $\delta_{pp}$

*et. al.* [13], is given by

$$\frac{16\pi}{(\sigma_{\rm tot}^{pp})^2}e^{-Bt}\frac{d\sigma_{pp}}{dt}A_N^{pp} = \frac{\sqrt{-t}}{m_p}\Big[(\mu_p-1)(1-\delta_{pp}\rho_{pp})-2(\mathrm{Im}\, r_5-\delta_{pp}\mathrm{Re}\, r_5)\Big]\frac{t_c}{t} -2(\mathrm{Re}\, r_5-\rho_{pp}\mathrm{Im}\, r_5), \quad (2.10)$$

$$\frac{16\pi}{(\sigma_{\rm tot}^{pp})^2}e^{-Bt}\frac{d\sigma_{pp}}{dt} = \left(\frac{t_c}{t}\right)^2 - 2(\rho_{pp}+\delta_{pp})\frac{t_c}{t} + (1+\rho_{pp}^2), \quad (2.11)$$

where $\mu_p$ is proton magnetic moment, $B$ is the nuclear slope parameter, and $t_c = -8\pi Z\alpha/\sigma_{\rm tot}$ with $Z = 1$ for the proton and $\alpha$ being the fine structure constant. The nuclear slope parameter is defined by the logarithmic derivative of the differential cross section at $t = 0$ ($B = |\partial \ln(d\sigma/dt)/\partial t|_{t=0}$). Equations 2.10 and 2.11 contain no contributions from double spin-flip amplitudes. These contributions are expected to vanish rapidly at $t = 0$ as $s \to \infty$ [13].

The expression for $A_N^{pp}$ in Equations 2.10 and 2.11 can be compared to experimental data to determine $\mathrm{Re}\, r_5$ and $\mathrm{Im}\, r_5$. The $-t$ dependence of $A_N^{pp}$ for $pp$ elastic scattering with a polarized proton beam momentum of 200 GeV/$c$ has been measured by the E704 collaboration at Fermilab [9]. The measurement covered the $-t$ range from $1.5\times10^{-3}(\mathrm{GeV}/c)^2$ to $5.0\times10^{-2}(\mathrm{GeV}/c)^2$ as shown in Figure 2.1. The result is consistent with no hadronic spin-flip amplitude. However, a nonzero hadronic spin-flip amplitude is possible within the experimental accuracy of the measurement. The CNI polarimeters at RHIC and the AGS provide the capability to accurately measure this amplitude using $pC$ elastic scattering.

## 2.3 Proton-Carbon Elastic Scattering

The analyzing power for $pC$ elastic scattering at low $-t$ is measured by the CNI polarimeters in the AGS and RHIC. The shape of the analyzing power $-t$ depen-

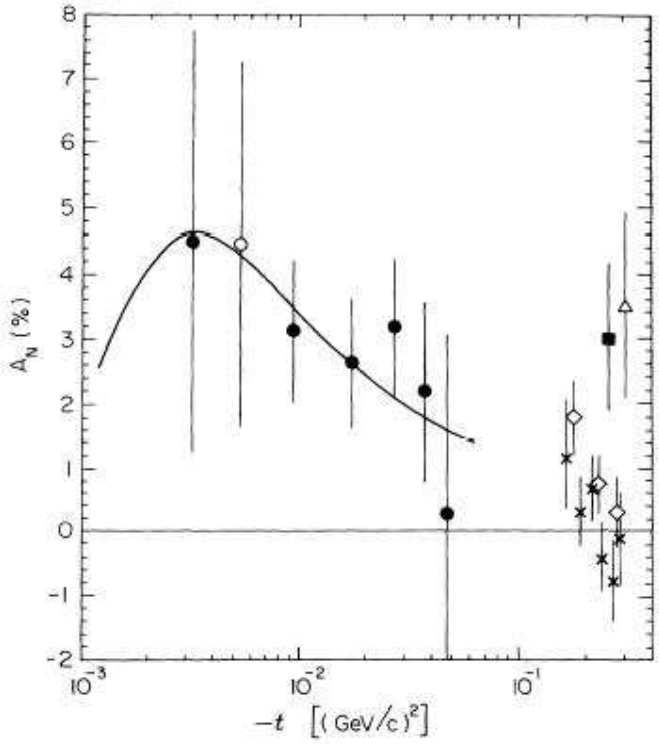


Figure 2.1: $A_N^{pp}$ versus $-t$ for $pp$ elastic scattering. The E704 data measured with a polarized proton beam momentum of 200 GeV/$c$ are indicated by $\bullet$. The other data points are measured at 185 GeV/$c$ ($\circ$) [14], 100 GeV/$c$ ($\diamond$) and 300 GeV/$c$ ($\times$) [15], and 176 $\pm$ 12 GeV/$c$ ($\triangle$) [16]. The black square denotes a measurement at 150 GeV/$c$ using a polarized target [17].

dence gives information about the hadronic spin-flip amplitude. The use of $pC$ scattering has the advantage over $pp$ scattering of separating the Pomeron contribution to the spin-flip amplitude from secondary Reggeon contributions [18]. Pomeron exchange is the dominant contribution to the hadronic interaction in the asymptotic limit $s \to \infty$; whereas, the secondary Regge pole contributions are suppressed by $\sim 1/\sqrt{s}$ [13]. In the medium energy range of the AGS, contributions from secondary Reggeons can be significant. At these energies, exchanges of the isovector Reggeons $\rho$ and $A_2$ are expected to be the dominant contributions to the hadronic spin-flip amplitude [19]. By using an isoscalar target, such as carbon, the isovector Reggeon contributions are eliminated, allowing one to probe the Pomeron spin-flip amplitude at medium energies. This advantage gives insight to the hadronic spin-flip amplitude at the high energy limit, which is of interest for understanding the nucleon constituent quark structure.

The $pC$ elastic scattering can be described by two helicity amplitudes, a spin-flip amplitude, $f_{+-}$, and a non-flip amplitude, $f_{++}$. The analyzing power[2], $A_N$, and differential cross section, $d\sigma_{pC}/dt$, can be written in terms of the amplitudes as follows

$$\frac{d\sigma_{pC}}{dt} A_N = 2\mathrm{Im}(f_{++} f_{+-}^*), \tag{2.12}$$

$$\frac{d\sigma_{pC}}{dt} = |f_{++}|^2 + |f_{+-}|^2. \tag{2.13}$$

As with the $pp$ helicity amplitudes, each amplitude can be expressed in terms of the electromagnetic part, $f^{\mathrm{em}}$, and hadronic part, $f^{\mathrm{h}}$.

$$f_j = f_j^{\mathrm{em}} + e^{-i\delta_{pC}} f_j^{\mathrm{h}}, \tag{2.14}$$

[2]Unless otherwise specified, the notation $A_N$ refers to the analyzing power for $pC$ elastic scattering.

where $j = ++, +-$ and $\delta_{pC}$ is the Coulomb phase. An expression for the Coulomb phase for $pC$ elastic scattering has been derived by Kopeliovich and Tarasov [20]. The Coulomb phase is given by

$$\delta_{pC} = 6\alpha e^{2\omega}[2E_1(2\omega) - E_1(\omega)], \tag{2.15}$$

$$\omega = -t\frac{B}{4}, \tag{2.16}$$

where $E_1(\omega) = \int_\omega^\infty e^{-u}/u du$ is the exponential integral. The nuclear slope parameter, $B$, is approximately equal to 60 $(\mathrm{GeV}/c)^{-2}$ for $pC$ elastic scattering.

The hadronic spin-flip amplitude for $pC$ elastic scattering, $r_5^{pC}$, is expressed in terms of the hadronic parts of the helicity amplitudes,

$$r_5^{pC} = \frac{m_N}{\sqrt{-t}}\frac{f^{\mathrm{h}}_{+-}}{\mathrm{Im}f^{\mathrm{h}}_{++}} \tag{2.17}$$

$$= \frac{1 - i\rho_{pC}}{1 - i\rho_{pN}} r_5, \tag{2.18}$$

where $m_N$ is the nucleon mass and $\rho_{pN}$ is the ratio of real-to-imaginary parts of the hadronic amplitude for proton-nucleon elastic scattering. By the optical theorem, the $pC$ elastic scattering total cross section, $\sigma_{\mathrm{tot}}^{pC}$, is given by

$$\sigma_{\mathrm{tot}}^{pC} = 4\sqrt{\pi}\mathrm{Im}f^{\mathrm{h}}_{++} \mid_{t=0} . \tag{2.19}$$

The ratio of real-to-imaginary parts of the hadronic amplitude, $\rho_{pC}$, is defined for $pC$ elastic scattering by

$$\rho_{pC} = \frac{\mathrm{Re}f^{\mathrm{h}}_{++}}{\mathrm{Im}f^{\mathrm{h}}_{++}}. \tag{2.20}$$

An explicit expression of $A_N$ parametrized in terms of $r_5^{pC}$ has been derived by Kopeliovich and Trueman [18]. $A_N$ and the differential cross section $d\sigma_{pC}/dt$

are written as

$$\frac{16\pi}{(\sigma_{\rm tot}^{pC})^2}\frac{d\sigma_{pC}}{dt}A_N = \frac{\sqrt{-t}}{m_N}F_C^h(t)\Big\{F_C^{em}(t)\frac{t_c}{t}\Big[(\mu_p-1)(1-\delta_{pC}\rho_{pC}) - 2(\mathrm{Im}\, r_5^{pC} - \delta_{pC}\mathrm{Re}\, r_5^{pC})\Big] - 2F_C^h(t)(\mathrm{Re}\, r_5^{pC} - \rho_{pC}\mathrm{Im}\, r_5^{pC})\Big\}, \tag{2.21}$$

$$\frac{16\pi}{(\sigma_{\rm tot}^{pC})^2}\frac{d\sigma_{pC}}{dt} = \left(\frac{t_c}{t}\right)^2[F_C^{em}(t)]^2 - 2(\rho_{pC}+\delta_{pC})\frac{t_c}{t}F_C^h(t)F_C^{em}(t) + \Big(1+\rho_{pC}^2 - \frac{t}{m_p^2}|r_5^{pC}|^2\Big)[F_C^h(t)]^2, \tag{2.22}$$

where $t_c = -8\pi 6\alpha/\sigma_{\rm tot}$ and $F_C^h(t)$ and $F_C^{em}(t)$ are the hadronic and electromagnetic form factors for carbon. From Equation 2.18 the expression for $A_N$ can be related to the hadronic spin-flip amplitude, $r_5$.

The measurement of $A_N$ by the E950 experiment is consistent with an nonzero hadronic spin-flip amplitude. Figure 2.2 shows the data from E950 with a fit using the expressions in Equations 2.21 and 2.22. A theoretical curve corresponding to no hadronic spin-flip amplitude is also shown. From the fit to the data the value of $r_5$ is given by[21]

$$\mathrm{Re}\, r_5 = 0.088 \pm 0.058, \tag{2.23}$$

$$\mathrm{Im}\, r_5 = -0.161 \pm 0.226. \tag{2.24}$$

The $A_N$ has also been measured with the AGS CNI polarimeter. The results and comparison to the E950 measurement are presented in Chapter 6.

Although the measurements at the AGS are made at medium-high energies, they give an indication of the behavior at the high energy asymptotic limit. At high energies the dominant contribution to the hadronic interaction is from

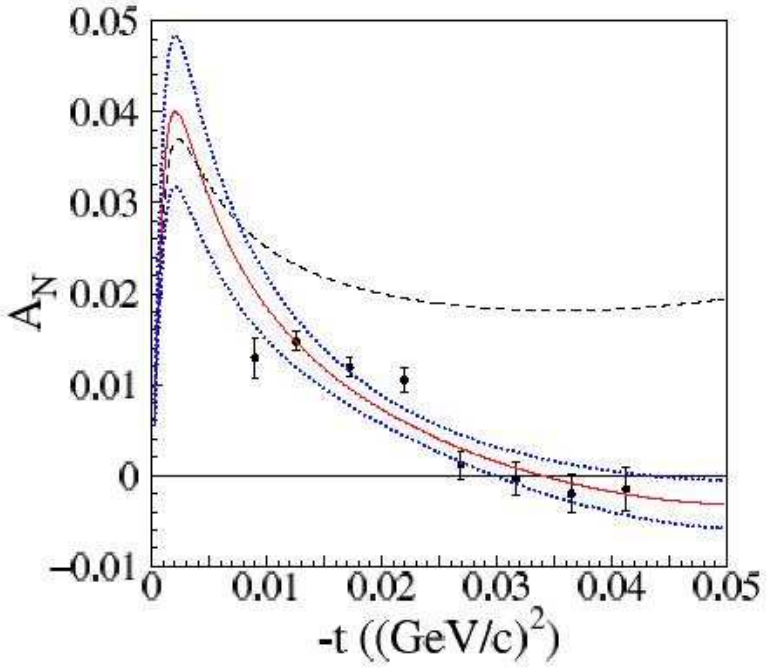


Figure 2.2: Analyzing power, $A_N$, for $pC$ elastic scattering versus $-t$, with a 21.7 GeV/$c$ polarized proton beam. The points represent data from the E950 experiment. The error bars are statistical only. The solid line is a theoretical fit to the data [18], and the dotted lines are the 1-sigma error band of the fit. The dashed line is the theoretical function with no hadronic spin-flip amplitude ($r_5 = 0$).

Pomeron exchange. At medium energies the exchange of other Regge poles is expected to contribute significantly to the hadronic spin-flip amplitude. By using an isoscalar carbon target, these secondary Regge pole contributions are eliminated, allowing one to probe the Pomeron spin-flip amplitude at medium energies. The study of the hadronic spin-flip amplitude is interesting because it carries implications for the quark structure of the nucleon. The hadronic spin-flip amplitude can be related to the isoscalar anomalous magnetic moment of the nucleon [22]. Also, a nonzero hadronic spin-flip amplitude at high energies suggests the possible existence of compact diquarks inside the nucleon [5].

# CHAPTER 3

# Production and Transport of Polarized Beams at RHIC

Before polarized proton beams can be collided in RHIC, they must be transported from the proton source and accelerated to collision energies. To date, colliding beams have been accelerated to energies of 100 GeV, but RHIC design allows for acceleration up to 250 GeV. This acceleration occurs in a number of different stages, and in each stage care must be taken to minimize depolarization effects. The major components used for the acceleration of proton beams at RHIC are diagrammed in Figure 3.1. Figure 3.1 also shows the location of some of the devices which help maintain polarization during the acceleration stages. The acceleration of polarized proton beams at RHIC and the techniques used to avoid depolarization are discussed in the sections below.

## 3.1 Polarized Proton Source and Early Acceleration Stages

The first stage of acceleration begins at the Optically Pumped Polarized Ion Source (OPPIS). The OPPIS uses an electron-cyclotron-resonance source to produce a proton beam of 3-5 keV energy. The protons capture polarized electrons as they pass through a rubidium (Rb) cell. The Rb cell sits in a 2.5 T magnetic field and is optically pumped by a continuous wave laser. The hydrogen atoms then

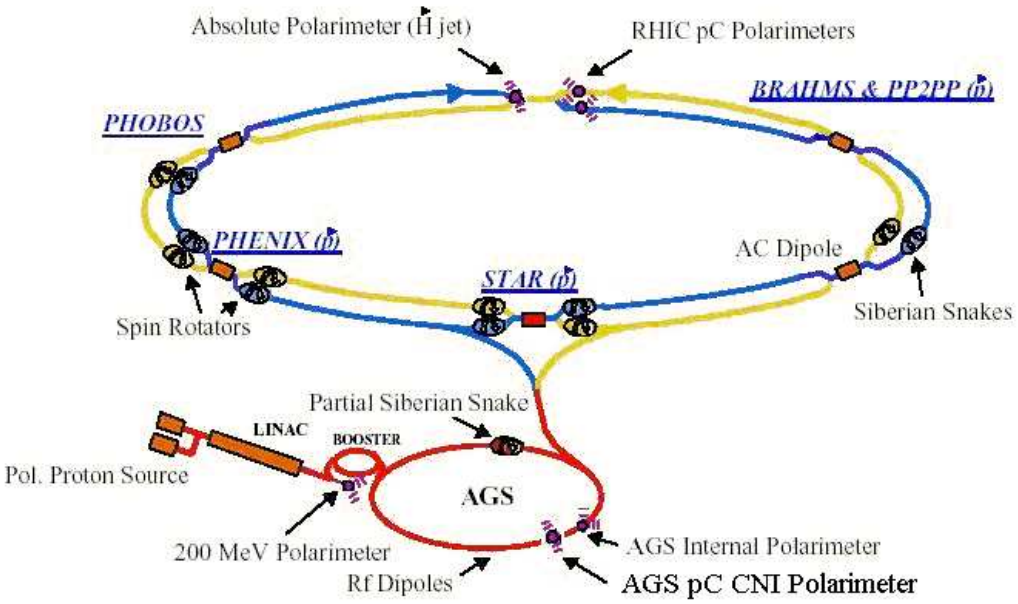


Figure 3.1: Layout of the RHIC facility. Polarized protons are acclerated from the source through a LINAC, a Booster synchrotron, and the AGS before being injected to the RHIC rings. Several of the components used to maintain polarization throughout the acceleration stages are shown. Locations of polarimeters are also noted. The experimental collaborations at RHIC (PHOBOS, PHENIX, STAR, BRAHMS and PP2PP) are labeled near their respective interaction regions.

pass through a region of changing magnetic field called a Sona transition region [23]. In the Sona region, the electron polarization is effectively transfered to the protons. Next, the polarized hydrogen atoms travel through a sodium vapor cell where some of the atoms capture electrons to form a polarized $H^-$ ion beam. The OPPIS has been previously used at the TRIUMF Parity Violation Experiment E497 [24]. A detailed description of the OPPIS can be found in E497 collaborator S. Diane Reitzner's thesis [25]. For RHIC, the OPPIS produces $\sim 0.5 - 1.5$ mA of $H^-$ current with $\sim 100 - 300\mu$s long pulses [26]. Polarization of the $H^-$ beam from the OPPIS is typically greater than 80%.

A radio frequency quadrupole magnet accelerates the polarized $H^-$ beam from the OPPIS up to 760 keV. Then, the beam is accelerated through a linear accelerator (LINAC) to an energy of 200 MeV. Here, the beam polarization can be measured with the so-called 200 MeV polarimeter, or the beam is injected into a synchrotron accelerator called the Booster. The 200 MeV polarimeter uses scintillation detectors in symmetric left and right arms to detect protons scattered from a carbon target. The asymmetry from this process ($p + C \rightarrow p +$ anything) has most recently been calibrated during AGS runs in August and December of 2001 [36]. During running there is a periodic switching of the beam from injection into the Booster to the 200 MeV polarimeter. So, the polarization is monitored for some sample of the beam at the end of the LINAC line. To seperate the beam for injection into the Booster, the $H^-$ ions are stripped of their electrons with a foil. In the Booster, polarized protons are bunched into a single radio frequency (RF) time bucket, and the bunch is accelerated to a total energy of 2.4 GeV. Polarized proton bunches from the Booster are then injected into the AGS, where they are accelerated up to 24.3 GeV in energy.

## 3.2 Spin Dynamics in the AGS

During the acceleration in the AGS, maintaining the beam polarization becomes difficult because many depolarizing resonance conditions are crossed. These conditions cause heterogeneous disturbances in the spin directions of bunched protons. The stable spin direction for protons is aligned (or anti-aligned) with the vertical bending field of AGS. The spin direction of each proton will precess around the vertical axis as it moves through the vertical magnetic field. Horizontal magnetic fields from misaligned dipole magnets and focusing quadrupole magnets can perturb the spin direction away from the stable vertical direction. Depolarizing resonance conditions occur when the spin precession is in phase with effects from horizontal depolarizing fields. The spin dynamics of proton beams in the AGS and devices used to correct for resonance effects are described below.

The orbital motion of protons as they move through the magnetic fields of the AGS is governed by the Lorentz force equation,

$$\frac{d(\gamma m\vec{v})}{dt} = e[\vec{E} + \vec{v} \times \vec{B}], \tag{3.1}$$

where $\vec{v}$ is the proton velocity, and $\vec{E}$ and $\vec{B}$ are the electric and magnetic fields acting on the proton. $\gamma$ is the relativistic Lorentz factor. $m$ and $e$ are the proton mass and charge magnitude. The notation here assumes units where $c = 1$. Assuming the proton motion is dominated by the vertical bending field (*i.e.* for $\vec{E} = 0$ and $\vec{B}_{\parallel} = 0$), the equation becomes

$$\frac{d\vec{v}}{dt} = -\frac{e}{m\gamma}\vec{B}_{\perp} \times \vec{v}. \tag{3.2}$$

The motion of the spin direction vector, $\vec{S}$, of a proton under the influence of

external fields is described by the Thomas-BMT equation [27]. Assuming a purely vertical magnetic field ($\vec{E} = 0, \vec{B}_{\parallel} = 0$), the spin precession in the rest frame of an orbiting proton is given by

$$\frac{d\vec{S}}{dt} = -G\gamma\frac{e}{m\gamma}\vec{B}_{\perp} \times \vec{S}, \tag{3.3}$$

where $G = (g-2)/2 = 1.7928474$ is the anomalous magnetic moment of the proton. By comparing Equations 3.2 and 3.3, one can see that the spin precesses $G\gamma$ times faster than the orbital motion. In other words, the spin precesses $G\gamma$ times for each revolution around the synchrotron. The number of spin precessions per orbital revolution is also called the spin tune $\nu_{sp}$. So, for a completely vertical magnetic field $\nu_{sp} = G\gamma$.

Depolarizing resonance conditions occur when the spin tune is in phase with effects that perturb the proton spin direction. When these resonance conditions occur depends both on properties of the accelerator and of the beam. One type of resonance condition, called an imperfection resonance, is caused by magnet misalignments and closed orbit errors. These resonances occur when the spin tune is equal to an integer, $n$.

$$\nu_{sp} = G\gamma = n. \tag{3.4}$$

Horizontal fields will perturb the spin direction in the same way for each revolution around the machine. The effects will add coherently when the spin tune equals an integer. Over 40 imperfection resonance conditions are crossed in the AGS as the beam is accelerated from an energy of 2.4 GeV ($G\gamma = 4.6$) up to 24.3 GeV ($G\gamma = 46.5$).

To correct for the depolarization from imperfection resonances in the AGS,

a device known as a Siberian snake magnet is used. A Siberian snake works by providing a strong enough magnetic field so that the stable spin direction for all particles rotates by 180°. In the AGS, a solenoidal magnet has been used as a 5% partial Siberian snake [28]. This causes a 5% (9°) rotation of proton spin direction, which is sufficient to cause a total spin flip when crossing imperfection resonances. The spin rotation from the Siberian snake magnetic field must be much greater than the rotation from the resonance condition. If this holds then the spin direction of all particles flip as the resonance is crossed and polarization is preserved.

The 5% partial Siberian snake is useful for overcoming the effects of imperfection resonances in the AGS. However, the strength of this snake is insufficient to overcome the effects of another type of resonance referred to as an intrinsic spin resonance. The intrinsic resonances arise from focusing fields of quadrupole magnets. Vertically focusing and horizontally focusing quadrupole magnets are alternated around the AGS ring to keep the beam focused near the center of the beam pipe. See Figure 3.2 for a diagram of a vertically focusing quadrupole. These magnets cause the protons' trajectory to oscillate vertically and horizontally as they circulate around the machine. This oscillation is called vertical and horizontal betatron motion. The horizontal focusing fields cause depolarization when the vertical betatron motion is in phase with the spin precession. The condition for intrinsic spin resonances is given by

$$\nu_{sp} = G\gamma = n\mathcal{P} \pm \nu_z, \tag{3.5}$$

where $n$ is an integer, $\mathcal{P}$ is the superperiodicity, and $\nu_z$ is the frequency of vertical betatron oscillation. Superperiodicity is defined simply as the number of superperiods in a synchrotron. A superperiod is a repeated section of bending and

focusing magnets. The AGS has 12 superperiods ($\mathcal{P} = 12$). Also, the vertical betatron oscillation frequency, $\nu_z$, is approximately 8.70 in the AGS.

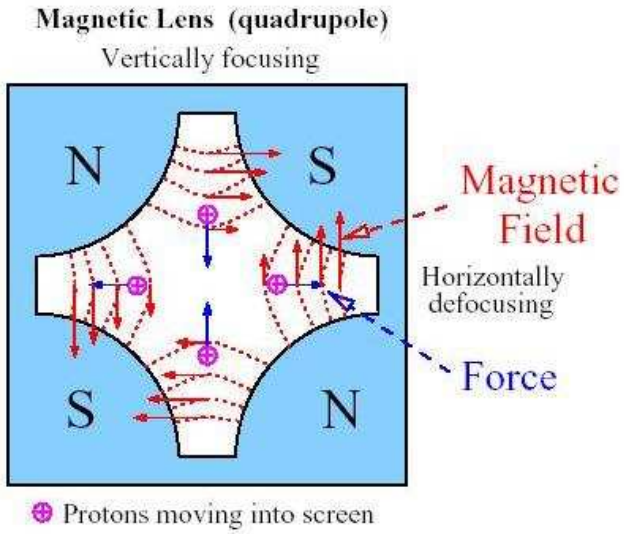


Figure 3.2: Diagram of a vertically focusing quadrupole magnet. The horizontal fields force the protons toward the center of the beam pipe. The vertical fields from this magnet actually tend to defocus the beam horizontally. Vertically focusing and horizontally focusing quadrupoles are positioned alternately around the AGS ring.

When a polarized beam is accelerated through an isolated resonance the polarization loss can be calculated using the Froissart-Stora equation [29]

$$P_f = (2e^{-\pi|\epsilon|^2/2\alpha} - 1)P_i, \tag{3.6}$$

where $P_i$ and $P_f$ are the polarizations before and after crossing the resonance. $\epsilon$ is the resonance strength, defined as the Fourier amplitude of the spin perturbing fields. $\alpha$ is the acceleration rate of the beam, defined as the rate of change of $G\gamma$ with respect to orbit angle around the ring ($\alpha = dG\gamma/d\theta$). If the beam is accelerated with a fast acceleration rate ($\alpha \gg |\epsilon|^2$), then little or no polarization is lost crossing the resonance. There are seven intrinsic resonances that are crossed

during acceleration in the AGS. With the typically fast acceleration rate in the AGS, there are only four strong intrinsic resonances at $0 + \nu_z$, $12 + \nu_z$, $36 - \nu_z$ and $36 + \nu_z$ that cause significant polarization loss [30].

To overcome the effects of the strong intrinsic resonances in the AGS, a pulsed RF dipole magnet is used to induce a full spin flip for all particles as these resonances are crossed. The RF dipole is pulsed in such a way that the vertical betatron oscillation amplitude is increased for all beam particles. The betatron amplitude is proportional to the resonance strength. When the betatron amplitude is made large then all particles are subjected to a very strong resonance. The extra-strong resonance results in a 180° spin flip for all particles and polarization is preserved [30].

The use of the 5% partial Siberian snake and the pulsed RF dipole in the AGS significantly reduce the depolarization effects from imperfection and strong intrinsic resonances. There are also depolarization effects from weak intrinsic resonances and another type of resonance called a coupling resonance. The effect of coupling resonances is essentially the same as that of intrinsic resonances. The spin direction is kicked from vertical beam motion through focusing quadrupole fields. Coupling resonances are associated with the vertical projections of horizontal betatron oscillations. In the AGS the main source of coupling to horizontal betatron motion is due to the field from the solenoidal Siberian snake magnet [31].

For the 2004 running period, the solenoidal Siberian snake magnet was replaced with a helical dipole magnet. This new magnet functioned as a 5% partial Siberian snake while avoiding the strong coupling associated with the solenoid. Consequently, the maximum beam polarization at extraction from the AGS was increased from approximately 40% in 2003 to approximately 50%. The 5% partial snake has been effective in overcoming polarization loss from weak resonance

conditions. A study has shown that a stronger Siberian snake could also be effective in overcoming the strong intrinsic resonances in the AGS [32]. The future use of a super-conducting helical dipole magnet as a 20% partial Siberian snake in the AGS is currently being developed.

## 3.3 Polarimetry at the AGS and RHIC

The effects of depolarizing resonances in the AGS are studied by measuring the beam polarization at a number of different beam energies. Prior to the installation of the AGS CNI polarimeter, polarization was measured solely by an internal polarimeter referred to as the E880 polarimeter, which is described in detail in the appendix of Reference [33]. This polarimeter uses left and right symmetric arms to detect recoil protons from *pp* elastic scattering. Each arm is comprised of an arrangement of plastic scintillation counters and an aluminum wedge-shaped degrader.

The polarimeter was designed so that protons from *pp* elastic scattering would be stopped in 1.5-cm-thick plastic scintillators ($L_3$ and $R_3$ in Figure 3.3), which sit behind the aluminum degrader in each arm. The position of the aluminum wedges are moved as a function of the beam momentum to be consistent with the kinematics of *pp* elastic scattering. The wedges absorb background from lower energy inelastic protons. Veto counters, position-sensitive hodoscopes and other scintillator counters are also used to separate elastically scattered protons from background. During calibration runs in November 2001, forward scintillator counters were also used to further reduce background contamination [34]. The forward counters were used to detect the forward moving elastically scattered proton in coincidence with the recoil proton. Three sets of forward counters were

positioned to detect $pp$ elastic scattering at beam momenta of 2.5 GeV/$c$, 3.9 GeV/$c$, and 6.5 GeV/$c$ ($G\gamma = 4.7$, 7.5, and 12.5). At higher beam momenta, the forward scattered proton does not exit the beam pipe and cannot be detected.

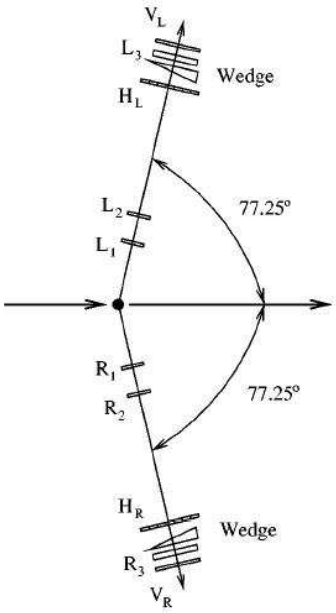


Figure 3.3: Schematic of the E880 polarimeter layout. $L_1$, $L_2$, and $L_3$ ($R_1$, $R_2$, and $R_3$) correspond to scintillators at 27.3 cm, 40.0 cm and 114.0 cm from the target in the left (right) arm. $H_L$ and $H_R$ are seven-element scintillator hodoscopes. $V_L$ and $V_R$ are veto scintillator counters.

For calibration of the E880 polarimeter, both nylon ($C_6H_{11}NO$) and carbon targets were used. The carbon target was used to subtract the non-hydrogen background from the nylon target. The beam polarization was then calculated using the known analyzing power for $pp$ elastic scattering [35]. Once the polarization was known, the analyzing powers of the recoil arms for $p+C_6H_{11}NO$ and $p+C$ were determined. With the high beam intensities available from the OPPIS, the nylon target is damaged very rapidly, so the carbon target is typically used for polarization measurements with the E880 polarimeter.

Polarization measurements with the AGS CNI and E880 polarimeters are both made in similar ways. The beam is accelerated, then held at a particular "flattop" energy. Once at flattop the target is inserted. The beam is held at flattop for $\sim 1.5$ sec before it is dumped. This cycle is repeated until the polarimeter gathers sufficient statistics. At AGS extraction energy (24.3 GeV), analyzing powers for both polarimeters are small ($\sim 1\%$), which means a large number of events must be collected to obtain a statistically significant measurement. At extraction energy the CNI polarimeter has larger event rates than the E880 polarimeter. Consequently, the CNI polarimeter allows for a faster measurement than the E880 polarimeter at extraction energy. A fast measurement time is essential for providing feedback to AGS accelerator physicists as they tune various beam parameters. The CNI polarimeter also has the advantage that a measurement during the beam acceleration can be made. The results from these measurements are discussed in Section 6.1. The addition of the CNI polarimeter has greatly enhanced ability to locate and quantify polarization losses in the AGS.

After extraction from the AGS, the beam is injected into RHIC through a transfer line. With a beam energy of 24.3 GeV the transfer line is nearly spin-transparent [37], and very little polarization is lost. Each RHIC ring can be filled with up to 120 polarized proton bunches from the AGS. After the filling of both rings is complete, the beams are accelerated to 100 GeV. Many spin resonances are crossed during the acceleration in RHIC, but the polarization is maintained by the use of two full Siberian snakes in each ring. Each Siberian snake rotates the proton spin direction by 180° for every revolution around RHIC.

During experimental running the beams are stored for several hours. Typically, polarization measurements in each ring are made with the RHIC CNI polarimeters once at injection energy and approximately once per hour at flattop

energy. These measurements provide the necessary polarization information to the experimenters making spin-dependent measurements. Data from the RHIC CNI polarimeters suggest that the polarization is well maintained while the beams are stored in RHIC. However, some polarization loss is observed from injection energy to flattop energy. Figure 3.4 shows the CNI polarimeter measurements for both the blue and yellow rings during the 2003 run [3]. Both injection energy and flattop energy (100 GeV) measurements are shown. For both rings the mean flattop polarization is less than the mean injection polarization. The discrepancy suggests some polarization loss during RHIC acceleration.

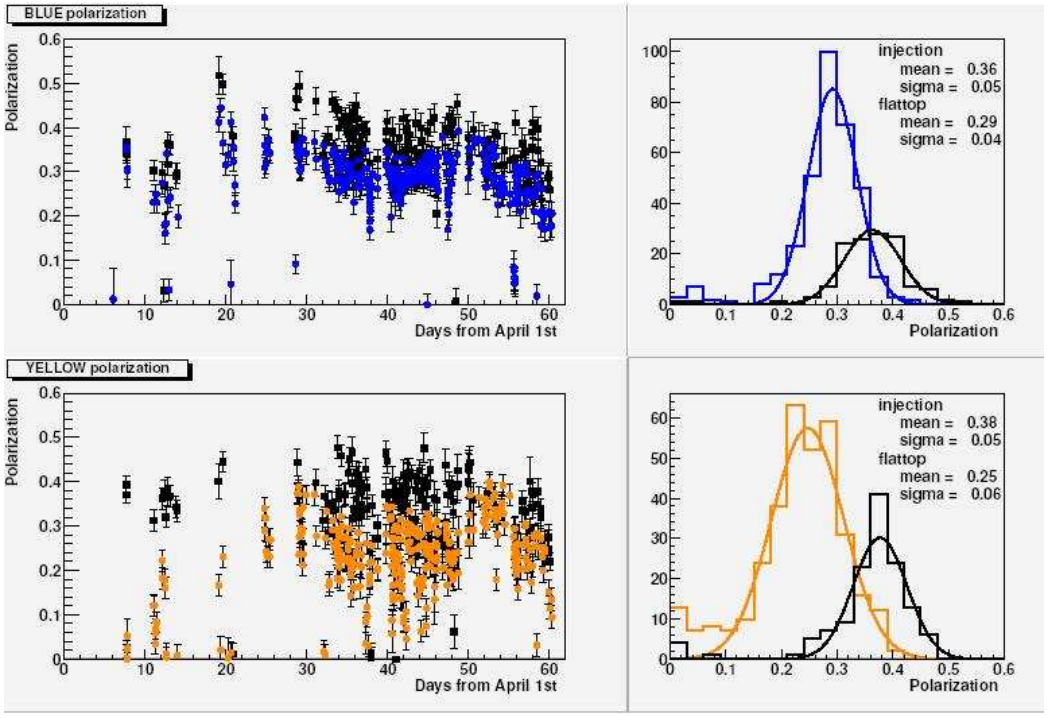


Figure 3.4: RHIC polarization values for the blue and yellow rings during the 2003 run. The plots to the left show the polarization versus day. The round (blue and yellow) points represent measurements taken at beam energy of 100 GeV. The square (black) points correspond to measurements at injection energy. The plots on the right are the projected polarization distributions. These plots show the intial "on-line" polarization values. The values increased by 1-3% after further analysis.

# CHAPTER 4

# Experimental Setup

The AGS CNI polarimeter vacuum chamber, pictured in Figure 4.1, was installed in the AGS ring in October 2002. The polarimeter operates by inserting a thin carbon foil target into a circulating polarized proton beam. Scattered carbon nuclei are detected using silicon strip detectors (SSDs), which are mounted directly to the left and to the right of the target. A data acquisition system provides timing and energy information for each event detected in the silicon. The beam polarization can be attained by calculating a left-right asymmetry from the measured carbon yields. The geometric setup and hardware used for the AGS CNI polarimeter are described in further detail in the sections below.

## 4.1 Carbon Targets

The targets used for the AGS CNI polarimeter are very thin carbon ribbon targets developed at the Indiana University Cyclotron Facility [38]. These targets have thicknesses of 3-5 $\mu$g/cm$^2$. The targets are 5 cm long and have widths ranging from 70 $\mu$m to 600 $\mu$m. Up to four different carbon targets can be mounted on a moveable frame inside the AGS CNI polarimeter chamber. A diagram of the target frame and SSDs is shown in Figure 4.2. Each target is mounted on the frame such that the direction along its width is at approximately 45° with respect to the beam direction. This position is a compromise between maximizing

Figure 4.1: The vacuum chamber used for the AGS CNI polarimeter. The frame used to hold the carbon targets can be seen through the large maintenance port, which is closed during polarimeter operation. To the left of this port are three smaller ports, used to mount silicon detectors. Three more detector ports are located on the opposite side of the chamber. To date, only the two detector ports on the horizontal axis have been equipped with silicon detectors.

the geometric cross section of the target exposed to the ∼2 mm wide beam and minimizing the path length through the target of carbon ions scattered near 90°.

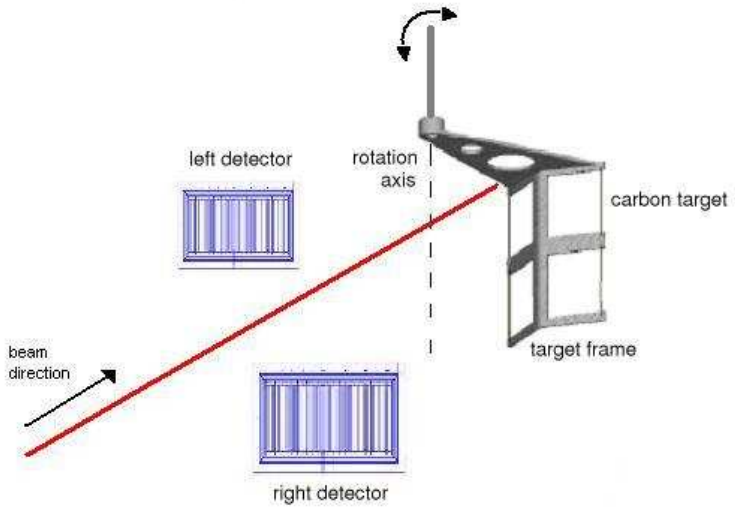


Figure 4.2: Diagram of the carbon target frame and silicon detectors for the AGS CNI polarimeter. Four carbon targets can be mounted on the target frame. The frame is rotated into the beam path during measurements. The silicon detectors are positioned to the left and to the right of the target to detect carbon ions scattered near 90°. This diagram is not to scale.

Only one of the installed targets is used at a given time for an individual measurement. The position of the target frame is adjusted remotely so that the height of the desired target corresponds with the beam position. Then the frame is rotated to place the target in the path of the beam. The rotary position of the target is oscillated in and out of the beam path once every AGS acceleration cycle. The target is only rotated into the beam path when the beam is at the proper energy for the measurement. This is done to minimize unnecessary exposure

of the target to the beam[1]. Prolonged exposure to the beam is suspected to eventually destroy the target.

For the 2003 running period, a total of eight targets were used. Four targets (two with widths of 365 $\mu$m, two with widths of 600 $\mu$m) were installed prior to the start of the run. The RHIC CNI polarimeters had previously been operated with target widths of 5 $\mu$m. Wider targets were chosen for use in the AGS because a larger event rate was desired. On April 9, 2003 the polarimeter vacuum chamber was let up to atmospheric pressure, so that the silicon detectors could be replaced. All four of the installed targets were destroyed during the procedure. Letting up the vacuum too quickly is suspected to have been the cause. Four more targets 70 $\mu$m, 100 $\mu$m, 450 $\mu$m, and 600 $\mu$m wide were installed. Of these the two narrower targets (70 $\mu$m and 100 $\mu$m) were destroyed during the installation procedure. The remaining 450 $\mu$m and 600 $\mu$m wide targets were then used for the rest of the 2003 running period.

For the 2004 running period, four targets were initially installed. Two of these had widths of 250 $\mu$m, and two had widths of 600 $\mu$m. The silicon detectors were replaced on April 29, 2004. An effort was made to let up the vacuum more slowly than the previous year. The targets were initially thought to be undamaged by this procedure. A later visual inspection revealed that three of the four targets appeared to be broken and vibrated when the target frame was moved. Two of the three damaged targets were replaced with new targets of the same widths. A replacement was not available for the third damaged target, and it was no longer used for taking data.

The data taken with one of the broken targets[2] showed large fluctuations in

[1]Rotating the target out of the beam for part of the cycle also prevents unnecessary radiation damage to the silicon detectors

[2]Only about 45 of the more than 1500 measurements taken during the 2004 run were made

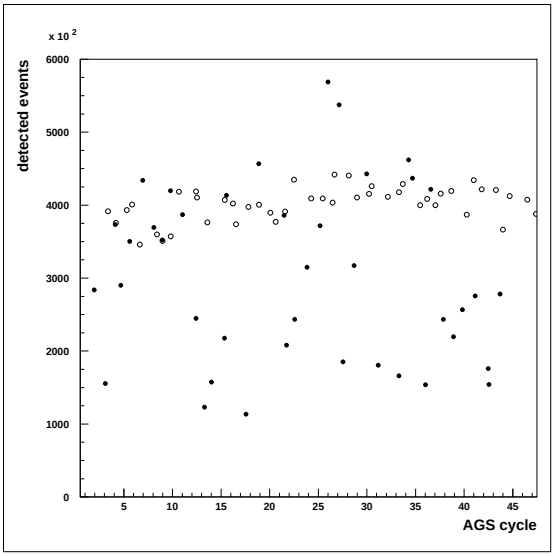


Figure 4.3: Number of total events detected with the AGS CNI polarimeter vs. AGS cycle number. The closed circles represent data taken with a broken target. The open circles were taken after the broken target was replaced by one of the same width (600 $\mu$m). The beam conditions were similar for the two measurements. Also, the measured asymmetries were consistent with one another.

the detected event rate from cycle to cycle. (See Figure 4.3.) The position of the broken target with respect to the beam is expected to have been moving from cycle to cycle. As the target moves away from the center of the beam, the proton-carbon interaction rate drops. Placing the target position near the center of the beam is important not only because it maximizes the event rate, but also because the beam polarization has been observed to decrease at the edge of the beam. Figure 4.4 shows the left-right asymmetry, $\varepsilon$, versus target position as measured by the AGS CNI polarimeter during the 2003 run. The event rate versus target position is also shown. As the target is moved away from the center of the beam, the measured asymmetry and the event rate both decrease.

The optimal target position is determined by adjusting the position until the maximum event rate is achieved. During the running periods, this procedure was done a few times each day or whenever a major change to the beam condition was made. For the data presented in Chapter 6 the target position was carefully set and monitored. However, such care was not taken for all of the thousands of individual polarization measurements made with this device. A method to automate the target positioning procedure is currently being developed in order to ensure that the target is well centered.

## 4.2 Silicon Detectors

The silicon detectors used to detect recoil carbon ions are segmented into 12 strips. Each strip measures 2 mm wide by 10 mm long. The length of the strips are oriented perpendicular to the beam direction. (See Figure 4.2.) Incident

with a broken target. The asymmetries measured with a broken target were not significantly different than those with an undamaged target.

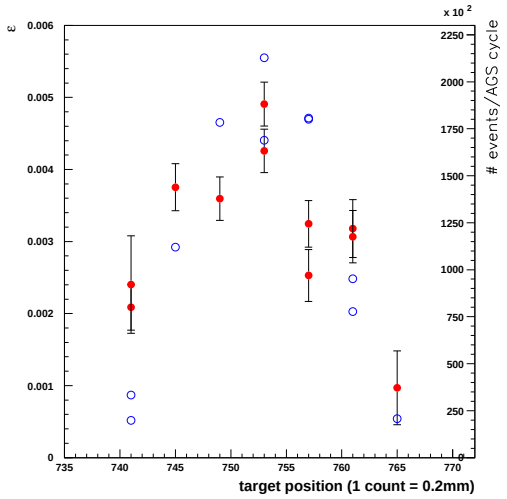


Figure 4.4: The measured asymmetry vs. target position (closed circles). The number of detected events per AGS cycle (open circles) is also plotted. The error bars on the asymmetry only represent the statistical error. These measurements were made during the 2003 running period. The measured asymmetry, $\varepsilon$, is defined in Appendix A.

radiation causes the creation of electron-hole pairs in the semiconductor wafer. The potential across the $p-n$ junctions sweeps the charge out of the so-called depletion region, and the current is read out by small ($\sim 0.5\text{mm}^2$), aluminum pads on the surface of each strip. The SSDs are operated with a 100V reverse bias applied across the silicon wafer. This extends the depletion region through most of the thickness of the wafer. However, there is an inactive, or dead, region, which is expected to be approximately 150 nm ($\approx 35\mu\text{g/cm}^2$) thick. The energy lost in this dead layer cannot be measured. A technique to correct for this energy loss was developed and is described in Section 5.2. The SSDs have a thickness of about 400 $\mu$m; this is sufficient to completely stop recoil carbon ions of energies up to $\sim$100 MeV. Alpha particle sources (americium-241) mounted inside the polarimeter vacuum chamber were used for calibrating the SSDs. The 5.5 MeV

alpha particles from the sources are also completely stopped in the detectors.

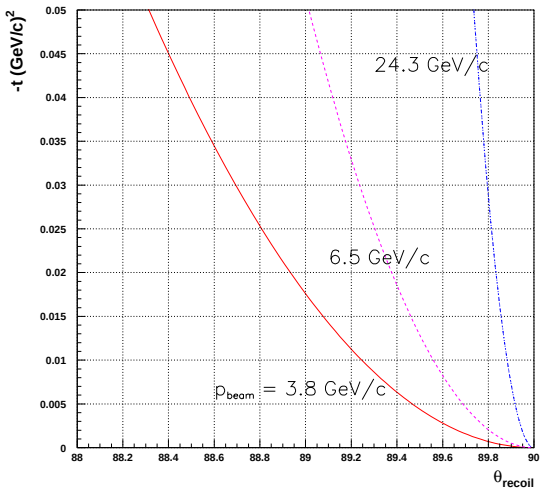


Figure 4.5: Calculation of $-t$ vs. carbon recoil angle (in degrees) for $pC$ elastic scattering. The relationship is plotted for three different proton beam momenta: 3.8, 6.5, and 24.3 Gev/c ($G\gamma$ = 7.5, 12.5, and 46.5).

During the 2003 run, two SSDs were used to make polarimeter measurements, one mounted directly to the left of the target and one directly to the right. The nominal distance between the target and the detectors was 25 cm. The actual flight path distance for carbons scattered from the target to the detectors varied from the nominal distance by a few millimeters as the rotary position of the target was adjusted to account for changes in the beam position. At 25 cm from the target, the SSDs have a recoil angle ($\theta_{recoil}$) acceptance of $90° \pm 2.7°$. At AGS extraction energy (24.3 GeV), the expected recoil angle distribution is well within the detector acceptance. Figure 4.5 shows the calculated $-t$ versus $\theta_{recoil}$ for $pC$ elastic scattering. At the lower beam energies in the AGS, carbon ions are scattered more forward than at extraction energy. When multiple scattering effects are considered the $\theta_{recoil}$ distribution extends near the limit of the SSD acceptance. In anticipation of measurements with lower beam energies, the target

positions were manually shifted backwards by approximately 5 mm during the 2003 run. This ensured that the entire $\theta_{recoil}$ distribution was within the SSD acceptance. Figure 4.6 shows an example of the distribution of detected events versus SSD strip number as measured during the 2003 run.

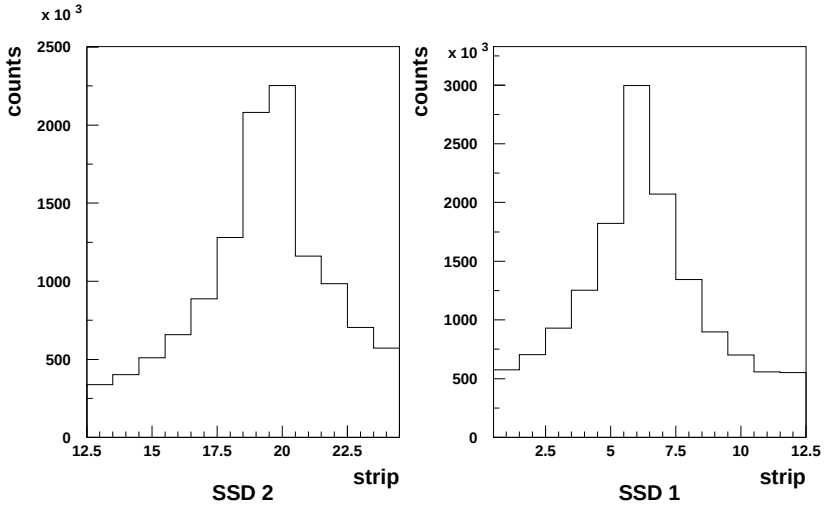


Figure 4.6: The distribution of detected events vs. SSD strip number for the 2003 run. SSD 1 was located to the right of the beam, SSD 2 to the left. Multiple scattering in the target causes a broadening of the distribution. The data shown is taken from an individual measurement taken on May 29, 2003. The beam energy is 24.3 GeV (extraction energy). The kinematic range of the data is $0.005(\mathrm{GeV}/c)^2 < -t < 0.027(\mathrm{GeV}/c)^2$.

For the 2004 running period, the distance from the target to the detectors was increased from 25 cm to 32 cm. This allowed for better separation of carbons from prompt background events and reduced signals induced by the beam. However, the increased distance also reduced the detector acceptance. To compensate for this, another pair of SSDs was added to the setup. Four SSDs were used in the 2004 polarimeter setup, two in the left arm and two in the right arm. The full $\theta_{recoil}$ distribution was still within the SSD acceptance for the AGS extraction energy, but at lower beam energies part of the distribution was outside of the

SSD acceptance. (See Figures 4.7 and 4.8.)

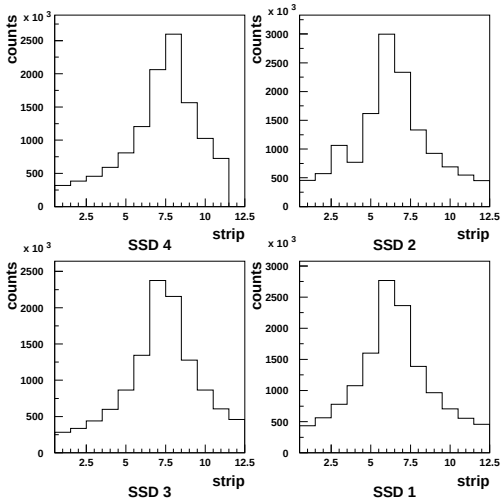


Figure 4.7: Detected event distribution vs. SSD strip number at $E_{beam} = 24.3$ GeV. Four SSD detectors were used for each measurement in the 2004 run. SSD 1 and 2 were positioned to the right of the beam. SSD 3 and 4 were positioned to the left. The $\theta_{recoil}$ acceptance is decreased with respect to the 2003 configuration, but the width of the distribution is still within the acceptance. The kinematic range of the data is $0.009(\mathrm{GeV}/c)^2 < -t < 0.04(\mathrm{GeV}/c)^2$. *Note:* Strip number 12 of SSD 4 was inoperative for most of the 2004 run.

An offset between the left and right carbon recoil distributions was observed for both the 2003 and 2004 runs. The 2004 data suggests that the left-side detectors were positioned $\sim 2$ mm further upstream of the beam than the right-side detectors. The polarimeter chamber and detector positions were surveyed after the 2004 run. The survey found that position of the left-side detectors was shifted by 1.3 mm, and the direction of the shift was consistent with the data. The survey also showed that the chamber was offset by 4-5 mm toward the inner radius of the AGS. This means that the beam was shifted 4-5 mm closer to the right detectors than the left detectors. Measured acceptance asymmetries, $\varepsilon_{acc}$ (defined in Appendix A), are consistent with a shift in that direction. Figure 4.9

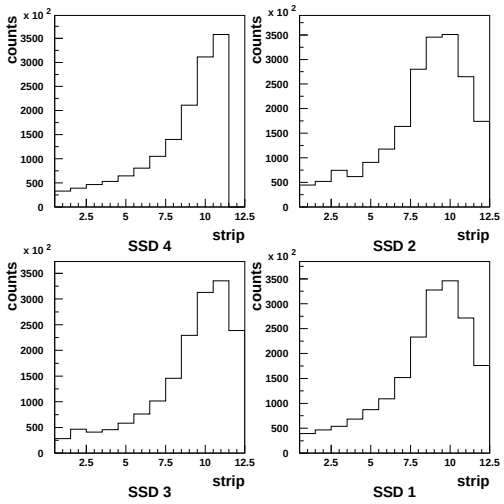


Figure 4.8: Detected event distribution vs. SSD strip number at $E_{beam} = 3.9$ GeV for the 2004 run. At low beam energies in the AGS, the more forward part of the $\theta_{recoil}$ distribution is outside of the SSD acceptance. The kinematic range of the data is $0.009(\mathrm{GeV}/c)^2 < -t < 0.04(\mathrm{GeV}/c)^2$.

shows acceptance asymmetries measured during the 2004 run.

The SSDs used for the 2003 and 2004 runs were replaced midway through each of the runs. The detectors were replaced to avoid excessive exposure to radiation. Large radiation doses can cause significant changes in the detector operation. This is primarily due to the build up of surface charge in the silicon and to silicon atoms being displaced from their lattice sites by incident radiation [39]. Measurments from the alpha sources were made periodically during the running period to account for changes in the detector response. Figure 4.10 shows the alpha source calibration constant, $C_\alpha$, for different measurements throughout the 2004 run. $C_\alpha$ is defined as

$$C_\alpha = C_{atten} \times \frac{E_\alpha}{\mu_{ADC}}, \tag{4.1}$$

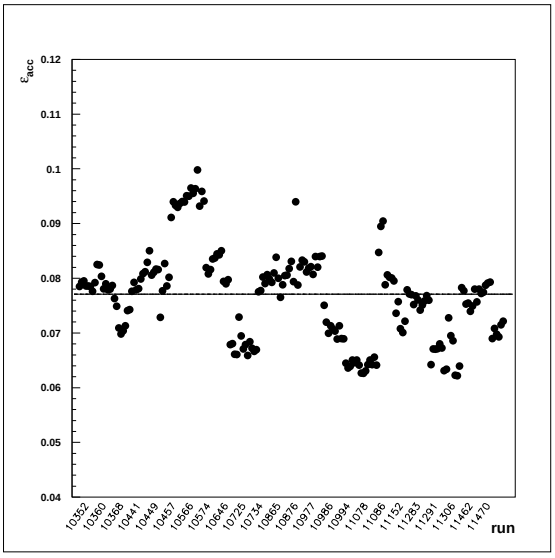


Figure 4.9: Acceptance asymmetry, $\varepsilon_{acc}$, versus polarimeter run number for a selection of runs from April 1 to May 13, 2004. The solid line represents a constant fit to the data with a value of 7.7%. Some of the sudden changes in $\varepsilon_{acc}$ can be attributed to changes in the AGS beam position.

where $E_\alpha$ is the alpha energy, 5486 keV, and $\mu_{ADC}$ is the mean from a gaussian fit to the alpha source ADC distribution. $C_{atten}$ is a factor to correct for the attenuation of the alpha signals. 14 dB attenuators were used to collect the alpha data, no attenuation was used for collecting carbon data for polarization measurements.

The alpha calibration constants show a small increase during the 2004 run. Alpha calibration constants from the 2003 run show a similar trend. The largest increase was observed in the latter part of the 2004 run from April 29, 2004 to May 14, 2004 (run number 90020 to 90023 in Figure 4.10). For this period, the alpha calibration constant increased by approximately 6%. A reliable method of measuring the detector leakage current was not available. Therefore, the change in the SSD leakage current due to radiation damage is not well known.

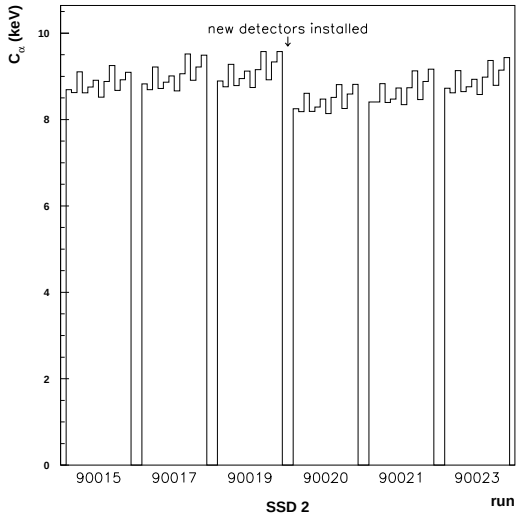


Figure 4.10: Alpha source calibration constant, $C_\alpha$, versus polarimeter run number. $C_\alpha$ for each of the 12 strips for one detector (SSD 2) is plotted for each run number. The SSD was replaced midway through the running period, and this is indicated on the plot.

## 4.3 Data Acquisition System

The signals from the SSDs pass through two stages of amplification before being digitized and stored for analysis. The first stage of amplification occurs on front-end electronics (FEE) boards installed outside the vacuum chamber in the AGS ring. Current pulses from each SSD channel pass through a pre-amplifier. The pre-amplifier produces a $\sim$ 100 mV pulse with a few $\mu$s rise time and a 50 $\mu$s decay time for a typical incident carbon event. The FEE boards are enclosed in an aluminum shielding box to help reduce noise from RF signals and stray fields in the AGS ring. (See Figure 4.11.)

In addition to the current pulses from incident radiation on the SSDs, signals induced by the passing beam current were also observed. During the early part of the 2003 run, large beam-induced pulses at high beam intensities caused problems

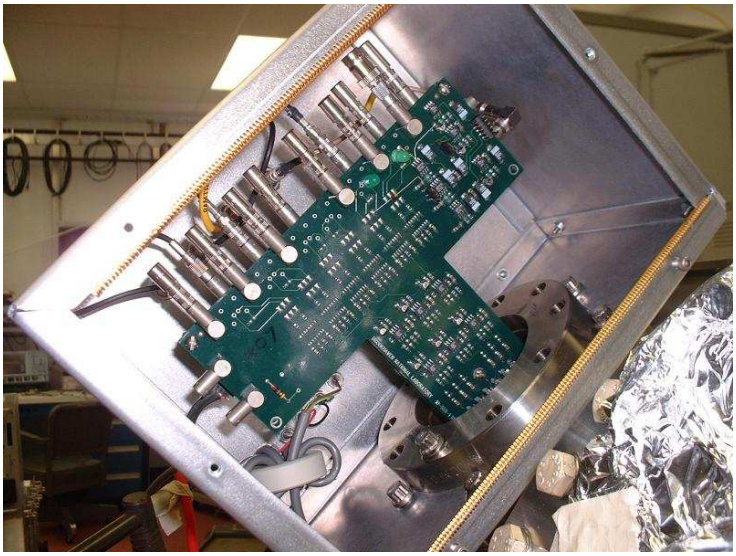

Figure 4.11: AGS CNI polarimeter front-end electronic (FEE) board. The FEE is mounted on the polarimeter chamber during bench tests before installation in the AGS ring. The FEE is enclosed in an aluminum shielding box to reduce noise. The box pictured here has one side open, but the FEEs were completely enclosed during polarimeter operation.

in the polarimeter operation. The large beam-induced pulses saturated the pre-amplifiers and generated noise, which obscured the carbon signals. Figure 4.12 shows an example of noise from beam-induced pulses at high beam intensity. As a result, the polarimeter was limited to operating with beam intensities below $\sim 1 \times 10^{11}$ protons per bunch. For the 2004 run, a new grounding scheme was designed for the SSDs. In addition, the SSDs were moved 7 cm farther away from the beam. These changes virtually eliminated the beam induced pulses, and the polarimeter was operable at larger beam intensities.

The signals from the front-end pre-amplifiers are transmitted over $\sim$ 100 m long cables to the polarimeter counting house. Signals are attenuated, if necessary (*e.g.* attenuators are used for signals from the alpha source). Next, the signals pass through a shaping amplifier. The shaping amplifiers produce a much faster

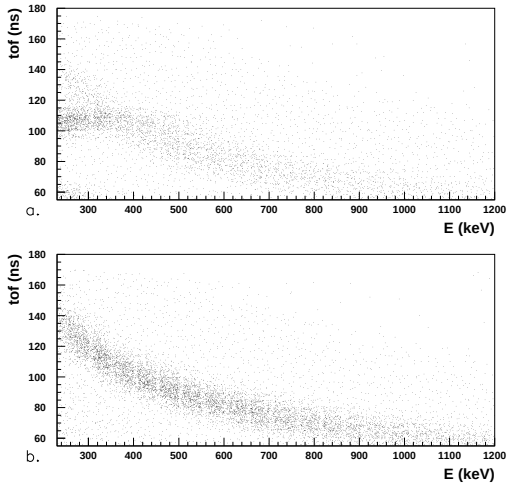


Figure 4.12: a. Time of flight ($tof$) versus energy of detected events for a measurement with beam intensity greater than $1 \times 10^{11}$ protons per bunch. Large beam-induced pulses caused "ringing" in the pre-amplifier electronics, which produced noise seen near 110 ns on the plot. b. Tof vs. energy for a measurement with beam intensity $\sim 0.5 \times 10^{11}$ protons per bunch. The carbon band is clearly seen.

signal with full width at half maximum (FWHM) of $\sim$ 10 ns. The signals from the shaping amplifiers are then processed by a waveform digitizer (WFD) system, which was developed at Yale University [40].

The WFD system consists of CAMAC modules with FPGA processors that are programmed to extract timing, amplitude, and total integrated charge for each input pulse. Each module also has 32 MB of on-board memory to store event information until it is read and stored on a PC. For the AGS CNI polarimeter, events are accumulated and read out once per AGS cycle. Each WFD module has four independent channels. Each channel input is split to three ADCs with 140 MHz sampling rates. (See Figure 4.13.) Two of the ADC inputs are delayed by 1/3 and 2/3 of the sampling period. This gives an effective digitization rate of 420 MHz (3 $\times$ 140 MHz) for each WFD channel. An algorithm is used to extrapolate between each waveform point, giving the WFD modules a timing resolution of $\sim$ 1.2 ns.

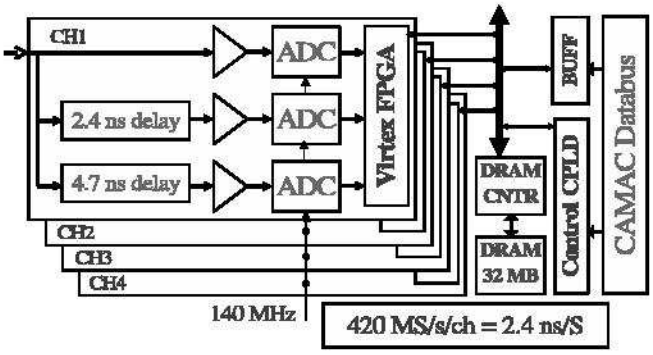


Figure 4.13: Block diagram of the WFD module.

The WFD modules are gated to acquire data during a portion of each AGS cycle. A signal is sent to the WFDs to indicate the start of each cycle. Then, delays are set to start and stop the data acquisition. The start and stop times are

set to coincide with when the beam is at the proper energy for the measurement. Data from all other times during the cycle are inhibited. The data acquisition is also gated to only acquire data when the circulating proton bunch is passing by the polarimeter target. A signal from one of the AGS beam current monitors is used to coordinate timing with the passing proton bunch.

The WFD modules also process external signals, which relay information about the AGS beam state. For each detected event, the WFD records the RF bunch position of the beam and the spin direction (up or down) of the proton bunch. The AGS typically operates with only one proton bunch, and the spin direction is alternated each AGS cycle. Another signal processed by the WFDs is the AGS Gauss Clock Count (GCC). The GCC is derived from a measurement of the magnetic field of a reference magnet in the AGS. The value of the GCC is proportional to the beam momentum. The value of these signals is record for each detected event.

# CHAPTER 5

# Analysis Methods

For each event detected by the AGS CNI polarimeter, several piece of information are available for analysis. These include the event timing, amplitude, and integrated charge. The AGS beam energy, RF bucket position, and polarization direction of the beam are also available for each event. A system of criteria use this information to seperate carbon events from background and to ensure overall data quality. These selection criteria were used by an "on-line" analysis method to quickly provide asymmetry and polarization values for each measurement. Selection criteria and data corrections were later refined for "off-line" analysis. Selection criteria and data corrections used for both the on-line and off-line analysis methods are described in this chapter.

## 5.1 Event Selection Criteria

Before a measured event is included in the event yield, many selection criteria or "cuts" must be passed. Several cuts are defined to check the validity of the AGS beam state. First, a cut is made on the beam energy. Any event with beam energy less than the desired value is cut. This is a redundant cut since the DAQ system is inhibited until the beam is at the proper energy for measurement. A cut is also made on the spin direction of the beam. For each AGS cycle, the spin direction of the beam is read from an external signal. If the spin direction is not recorded to

be in a valid state, then any associated events are cut. A selection criteria is also defined to select events from the proper RF bucket. During standard operation, the proton beam is bunched into a single RF bucket. However, events can occur from stray beam in one of the "empty" RF buckets. (See Figure 5.1.) Only events from the desired RF bucket are selected. These cuts ensure that the AGS beam is in the proper state for polarimeter measurements.

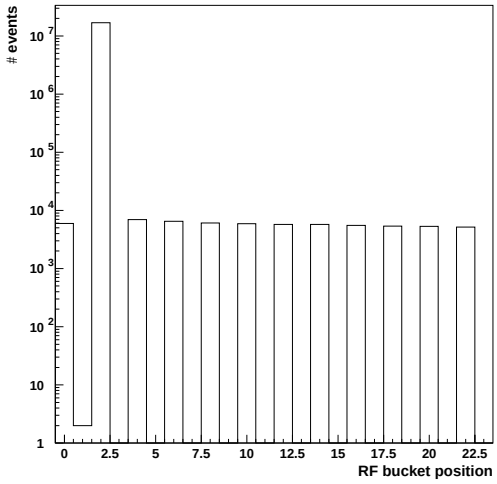


Figure 5.1: Number of detected events vs. RF bucket position for an individual measurement during the 2004 run. For this measurement the beam is located in RF bucket 2. Events from other bucket locations are not used for calculating asymmetries.

Another set of cuts are defined to remove background events from polarimeter data. Scattered carbon events are selected from background events using a cut on the time of flight ($tof$) to kinetic energy ($E_{kin}$) correlation. The kinematics of the recoil carbons that are of interest ($<\sim$2 MeV) can be described non-relativistically.

$$tof = l\sqrt{\frac{m_C}{2E_{kin}}}, \tag{5.1}$$

where $l$ is the distance from the target to the detector and $m_C$ is the carbon

mass, 11.18GeV/$c^2$. The on-line event cut was set to select events between ± 15-20 ns of the expected $tof$-energy correlation. Figure 5.2 shows a graphical representation of the event selection. For off-line analysis, another event selection criterion defined by fitting the carbon mass peak was also used. This is discussed in Section 5.3.2.

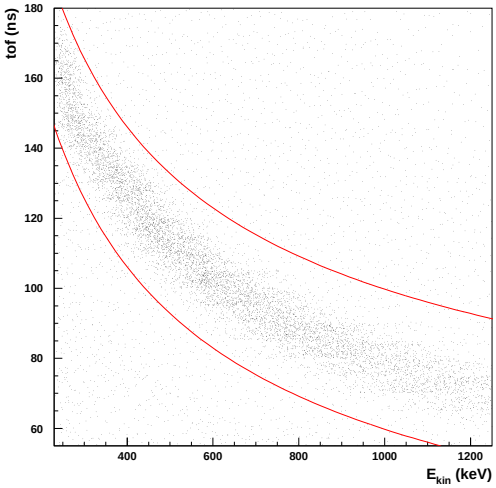


Figure 5.2: Time of flight vs. kinetic energy of detected events from a measurement during the 2004 run. The lines represent the expected $tof$-energy correlation (Equation 5.1) ± 20 ns. Only events between the two lines are selected for calculating asymmetries.

In addition to the $tof$-energy correlation cut, events were also selected for a kinematic range in momentum transfer. For $pC$ elastic scattering, the momentum transfer squared, $-t$, is proportional to the kinetic energy of the scattered carbon,

$$-t = 2m_C E_{kin}, \tag{5.2}$$

where $m_C$ is the carbon mass and $E_{kin}$ is the kinematic energy of the scattered carbon. During the 2003 running period, the kinematic range used for calculat-

ing asymmetries was defined to be $0.009(\mathrm{GeV}/c)^2 \leq -t \leq 0.022(\mathrm{GeV}/c)^2$, which corresponds to approximately $400\mathrm{keV} \leq E_{kin} \leq 1000\mathrm{keV}$. The lower limit of this range was set to avoid the noise from beam induced pulses, as seen in Figure 4.12a. The upper boundary of the $-t$ range was limited by the separation in $tof$ between carbon events and prompt background events. As seen in Figure 5.3, a significant number of relativistic background events are observed with the AGS CNI polarimeter. These events are usually well separated from the slower moving carbon events. However, at energies greater than 1000 keV the carbon events are difficult to distinguish from prompt background events. For the 2004 running period, the beam induced noise was eliminated, and the increased distance to the detectors created greater separation between the carbons and prompt background. These changes allowed the kinematic range of the polarimeter to be broadened. However, the kinematic range used for calculating asymmetries remained the same as the 2003 run. The kinematic range was unchanged because it allowed for an unbiased comparison between the 2003 and 2004 asymmetries.

A few other cuts were defined to ensure that the carbon data was not infiltrated by any unforseen noise or background. These cuts were put in place mainly to reject events from aberrant cycles in which there were unexpected changes to the beam. A cut was defined to rejected spills with an anomalously low number of detected events. Also, spills with a low percentage of events that pass the $tof$-energy correlation cut were rejected. Another cut measured the number of events in a kinematic region where noise was typically observed to occur. These values were usually very constant from cycle to cycle. These cuts were only designed to reject anomalous cycles. Figure 5.4 shows some of the on-line plots used to monitor these parameters.

Several plots, including those shown in Figure 5.4, were produced for each

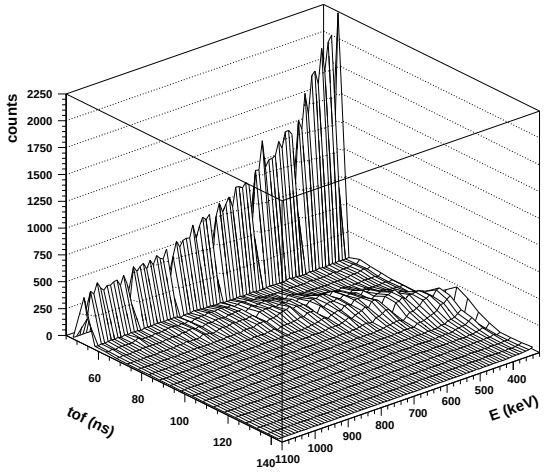


Figure 5.3: A three-dimensional surface plot of time of flight vs. energy. Many prompt background events are seen near $tof = 50$ ns. The carbon events are seen later in $tof$. The carbon $tof$ decreases as energy increases. For energies greater than 1000 keV, the carbon band is difficult to distinguish from the prompt background.

AGS polarimeter measurement. These plots were examined for quality assurance of the polarimeter data, and they served as an invaluable tool during the commissioning of the polarimeter. Some of the plots used for quality assurance include $tof$ vs. $E_{kin}$ for each detector strip, the event distribution vs. strip number, several different asymmetries vs. cycle number, and the $-t$ dependence of $\varepsilon$ and $A_N$. Examples of some of the plots used for on-line quality assurance monitoring are displayed in Figures 5.5 and 5.6.

During the 2003 and 2004 runs, the AGS CNI polarimeter was able to quickly provide many polarization measurements. For a typical measurement time of $\sim 8$ min., the polarimeter produced several quality assurance plots and measured beam polarization with a statistical precision better than 5% ($\Delta P/P < 0.05$). Since its commissioning the AGS CNI polarimeter has been the primary source

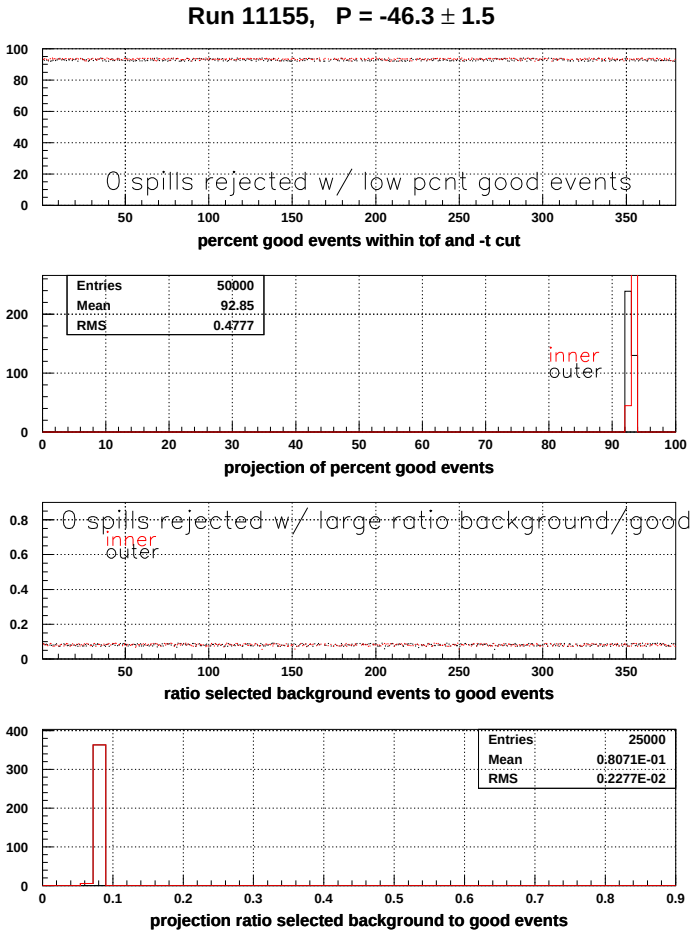


Figure 5.4: On-line plots used for data quality assurance from a measurement during the 2004 run. The top plot shows the percentage of events that pass the event selection cuts versus cycle number. The next plot below shows the projections onto the vertical axis for both the inner (left-side) and outer (right-side) detectors. The plot second from the bottom shows the ratio of background events from a chosen region to selected carbon events. The ratio is plotted versus cycle number. The bottom plot shows the projection of the ratio onto the vertical axis.

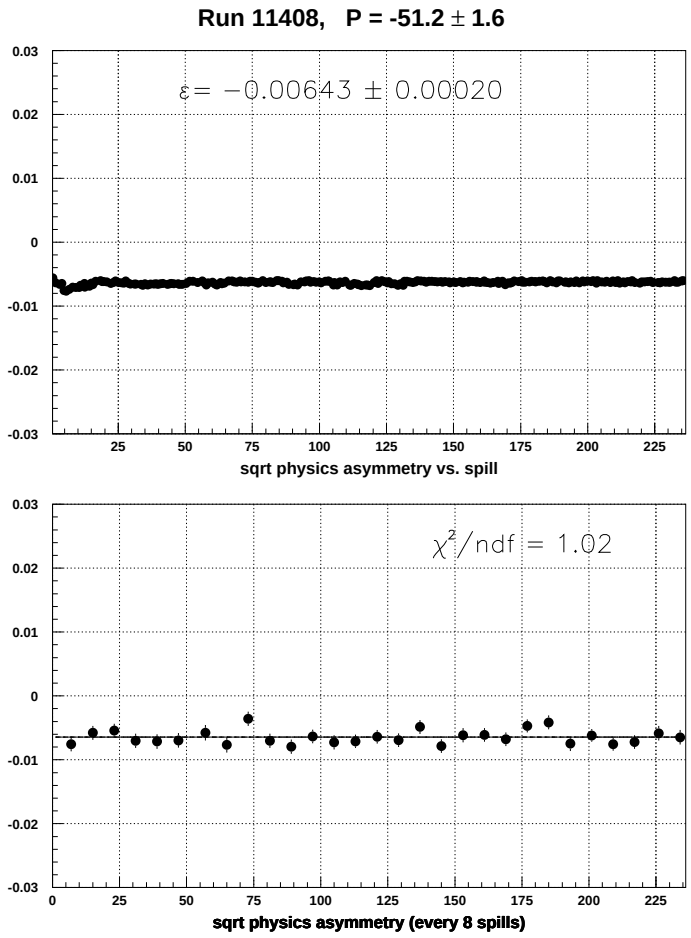


Figure 5.5: Example of on-line quality assurance plots from a measurement during the 2004 run. The top plot shows the asymmetry, $\varepsilon$, for accumulated data vs. cycle. $\varepsilon$ varies for the first $\sim$ 20 cycles, but then converges to a constant value. The bottom plot shows $\varepsilon$ calculated seperately for every eighth cycle (spill). The constant line corresponds to the final accumulated value of $\varepsilon$. $\chi^2$ per number degrees of freedom of the data is calculated and displayed on the plot. The error bars on the bottom plot are statistical only. No error bars are shown on the top plot.

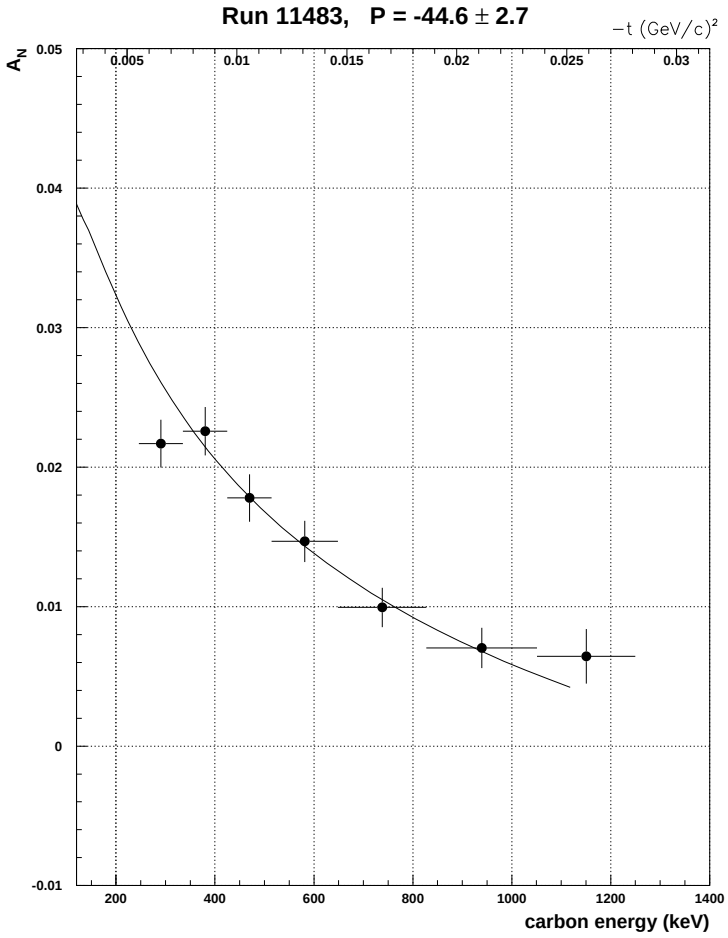


Figure 5.6: $A_N$ vs. carbon energy ($E_{kin}$) and $-t$, an on-line plot from a measurement during the 2004 run. The points are derived from the measured asymmetry, $\varepsilon$. An effective analyzing power, $\langle A_N \rangle$, based on the fit to E950 data is calculated for $400keV \leq E_{kin} \leq 1000keV$. (See Appendix A for definition of $\langle A_N \rangle$.) $\langle A_N \rangle$ is used to calculate polarization, $P = \varepsilon / \langle A_N \rangle$. The points in this plot are then given by $\varepsilon_i / P$, where $\varepsilon_i$ is the measured asymmetry for $i^{th}$ bin in $-t$. The solid line represents the theoretical fit to the E950 data [4]. The vertical error bars are statisical only.

of beam polarization measurements in the AGS and has been an extremely useful tool for AGS accelerator physicists. Accelerator physicists use feedback from the polarimeter to tune the AGS for optimum polarization output. Much improvement to the beam polarization has been made since the AGS CNI polarimeter has been in operation. During the 2004 run, beam polarizations of approximately 50% were regularly measured at AGS extraction energy. In addition to the on-line polarization values provided by the polarimeter, a number of off-line corrections and studies were made to improve the polarization accuracy and understand the systematic effects of the polarimeter. These off-line corrections and studies are described in the sections below.

## 5.2 Energy Calibration and Corrections

As mentioned in Section 4.2 americium alpha sources are used to calibrate the response of the SSDs. However, additional corrections are needed to accurately reconstruct the energy of scattered carbons. A method to account for energy lost in the silicon dead layer is the main correction that is needed. For the 5.5 MeV alphas from the sources, the energy lost in the silicon dead layer is ignored. The energy lost in a 35 $\mu$g/cm$^2$ thick dead layer is $\approx$ 20 keV [42]. However, for the low energy ($<\sim$2 MeV) carbons that are of interest, the energy lost in the dead layer is significant.

The energy deposited in the active silicon region ($E_{dep}$) is measured. Then, a correction for the energy lost in the dead layer must be made to reconstruct the incident kinetic energy ($E_{kin}$) of the carbon. There were two methods used to correct for the dead layer energy loss, a simple method used for on-line analysis and a more refined method used to make off-line corrections. Both methods make

use of the MSTAR program to calculate the stopping power of carbon in silicon [41]. The energy loss in the dead layer ($E_{dead}$) can then be calculated for a given dead layer thickness ($t_{dead}$). The details and differences of both methods are described below.

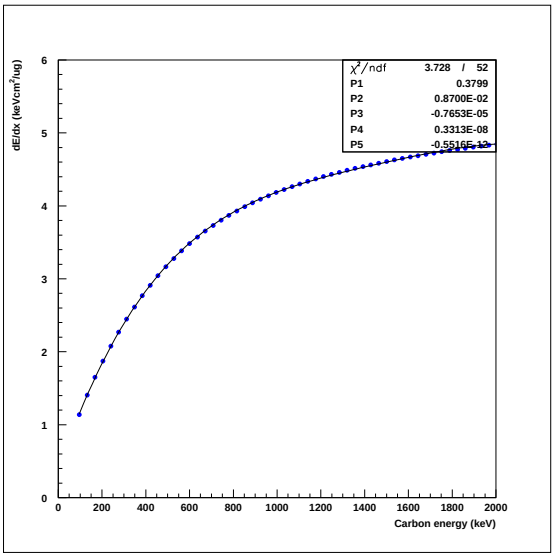


Figure 5.7: Energy loss vs. incident energy for carbon in silicon as generated by MSTAR. The points are fit with a fourth order polynomial. The fit parameters are displayed in the upper-right corner of the plot.

The MSTAR program is used to generate a table of energy loss ($\frac{dE}{dx}$) for carbon ions in silicon for a range of incident energies. Data from the MSTAR table are shown in Figure 5.7. Notice that the energy loss actually increases with carbon energy for this energy range from 0.1 to 2 MeV. The data from the table are fit well with a fourth order polynomial. This function is used to calculate the integrated energy loss for a dead layer of a given thickness. A thickness of 150 nm, or 35 $\mu$g/cm$^2$, is expected for the SSDs used for this polarimeter, but the exact value is unknown.

Energy loss is calculated for a range of dead layer thicknesses from 20 to 100 $\mu$g/cm$^2$. For each thickness the energy deposited in the dead layer, $E_{dead}$, is

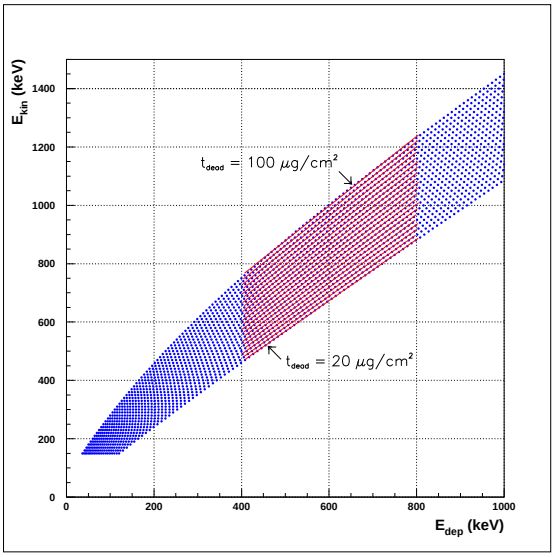


Figure 5.8: Incident carbon energy versus energy deposited in the active silicon region from MSTAR calculations. Data are plotted for different dead layer thickness assumptions ranging from 20 to 100 $\mu$g/cm$^2$. For each thickness the correlation is fit with a linear function for 400 keV $< E_{dep} <$ 800 keV.

calculated for carbon incident kinetic energies between 0.1 and 2 MeV. Figure 5.8 shows the calculated values of $E_{dep}$ ($= E_{kin} - E_{dead}$) plotted versus $E_{kin}$ for several values of $t_{dead}$. For each thickness the points are fit with a linear function from 400 keV to 800 keV in $E_{dep}$. The data are quite linear in this energy range. Also, the slopes of the fits vary little with dead layer thickness.

Again, the goal of this method is to be able to correct the experimentally measured values of $E_{dep}$ to produce the initial kinetic energy, $E_{kin}$. The linear fits in Figure 5.8 relate $E_{dep}$ to $E_{kin}$ by two dead layer thickness dependent parameters.

$$E_{kin} = A(t_{dead}) + B(t_{dead}) \times E_{dep}. \tag{5.3}$$

Two $t_{dead}$ dependent parameters can be reduced to one by fitting the linear relation between $A$ and $B$. The result is shown in Figure 5.9. In this way, $E_{dep}$ is

related to $E_{kin}$ by a single $t_{dead}$ dependent parameter. The relation between $E_{kin}$ and $E_{dep}$ can now be written as

$$E_{kin} = E^0_{dead} + [1.043 + (0.5544 \times 10^{-3})E^0_{dead}] \times E_{dep}, \tag{5.4}$$

where $E^0_{dead}$ is the $t_{dead}$ dependent parameter. $E^0_{dead}$ is equivalent to $A$ in Equation 5.3, but the notation is changed to reflect that $A \approx E_{dead}$ when $B \approx 1$. Note that the slope parameter that relates $A$ to $B$ $(= 0.5544 \times 10^{-3})$ has units of $(\text{keV})^{-1}$. The relation in Equation 5.4 is used to translate the measured quantity $E_{dep}$ to $E_{kin}$. First, a reasonable expectation for $E^0_{dead}$ is used. Then, the correlation between the $E_{kin}$ and time of flight $(tof)$ of subsequent data is fit with $E^0_{dead}$ being a free parameter.

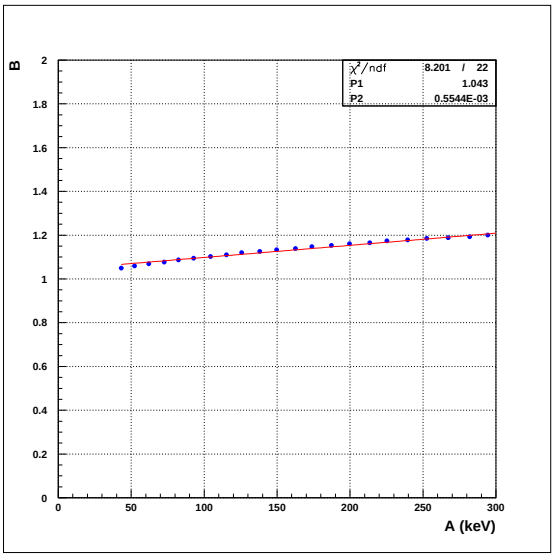


Figure 5.9: The slope versus y-intercept values from the linear fits in Figure 5.8. This correlation is also fit with a line. The fit results are displayed in the upper-right corner of the plot. By relating $A$ and $B$ the relation between $E_{kin}$ and $E_{dep}$ can be written in terms of only one $t_{dead}$ dependent parameter.

The measured time of flight for each event also requires a correction that

must be fit from the data. The timing is measured relative to an electronic clock signal, which is synchronized to the revolution frequency of the proton bunch in the AGS. There is a time offset between this clock and the actual time that the proton bunch interacts with the carbon target, so the time of flight is given by

$$tof = t_{meas} - t_0, \tag{5.5}$$

where $t_{meas}$ is the measured time and $t_0$ is the constant offset. Like $E^0_{dead}$, $t_0$ must be extracted from a fit to the correlation between $E_{kin}$ and $tof$. Also, $t_0$ can vary by a few ns for each channel of the SSDs due to differences in cable length.

Equations 5.4 and 5.5 relate $E_{kin}$ and $tof$ to two directly measured quantities: $E_{dep}$ and $t_{meas}$. The deposited energy, $E_{dep}$, is found by multiplying the measured signal amplitude ($Amp$) by the alpha calibration constant, $C_\alpha$ (defined in Equation 4.1). Substituting Equations 5.4 and 5.5 into the $tof$-energy correlation (Equation 5.1) yields the following relation:

$$t_{meas} = l\sqrt{\frac{m_C}{2}}\frac{1}{\sqrt{E^0_{dead} + [1.043 + (0.5544 \times 10^{-3})E^0_{dead}] \times C_\alpha Amp}} + t_0. \tag{5.6}$$

Equation 5.6 is used to fit the correlation between the measured quantities $t_{meas}$ and $Amp$ while $E^0_{dead}$ and $t_0$ are free parameters.

The correlation between $t_{meas}$ and $Amp$ is clearly seen in the data, as shown in Figure 5.10a. For convenience, the nearly linear correlation between $t_{meas}\sqrt{Amp}$ and $Amp$ is fit. Figure 5.10b. shows $t_{meas}\sqrt{Amp}$ versus $Amp$. To fit the correlation, slices along the $x$-axis are fit with gaussians. The mean values from these fits are then fit using the relationship from Equation 5.6. Such fits are performed for data from each detector strip and each of these fits yield a new set of $E^0_{dead}$ and $t_0$ values. For the on-line results, $E^0_{dead}$ and $t_0$ were fit periodically for selected

polarimeter runs. These $E^0_{dead}$ and $t_0$ values were then used to reconstruct the $E_{kin}$ and $tof$ data of subsequent runs.

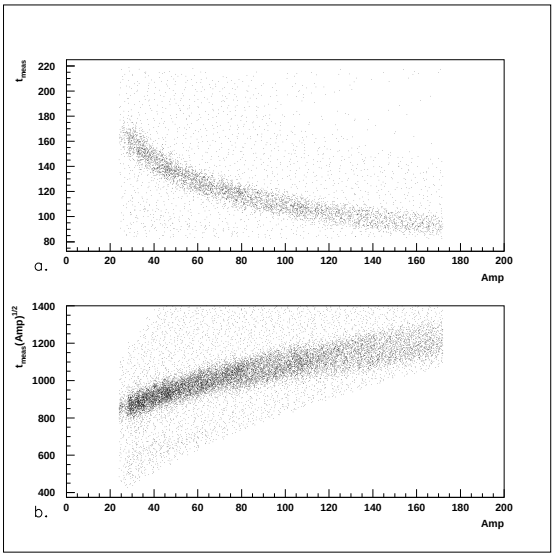


Figure 5.10: a. Example of measured time versus amplitude data from one SSD strip. b. $t_{meas}\sqrt{Amp}$ versus $Amp$ for the same data shown in a.

The dead layer thickness is expected to be fairly constant for a set of detectors. Accordingly, little variation is expected for the $t_{dead}$ dependent parameter $E^0_{dead}$. However, the values of $E^0_{dead}$ from fits to the data do show fluctuations. Figure 5.11 shows the $E^0_{dead}$ values extracted from several polarimeter runs. The $E^0_{dead}$ values show some variation with detector strip. The strip dependence of $E^0_{dead}$ is different for each detector, and the origin of this dependence is unclear. Larger variations in $E^0_{dead}$ occur between individual polarimeter runs. $E^0_{dead}$ varies from run to run by approximately 30% for detectors 3 and 4. Detectors 1 and 2 vary less, but still show some fluctuation. Also, the values of $E^0_{dead}$ for detector 3 are significantly less than the other detectors. The variations in $E^0_{dead}$ cause shifts in the reconstructed $E_{kin}$ spectra and consequently effect the asymmetry and polarization values. After the end of the 2004 running period, a method was

developed to quantify the effects of these variations. This method and other differences in the off-line asymmetry calculations are discussed below.

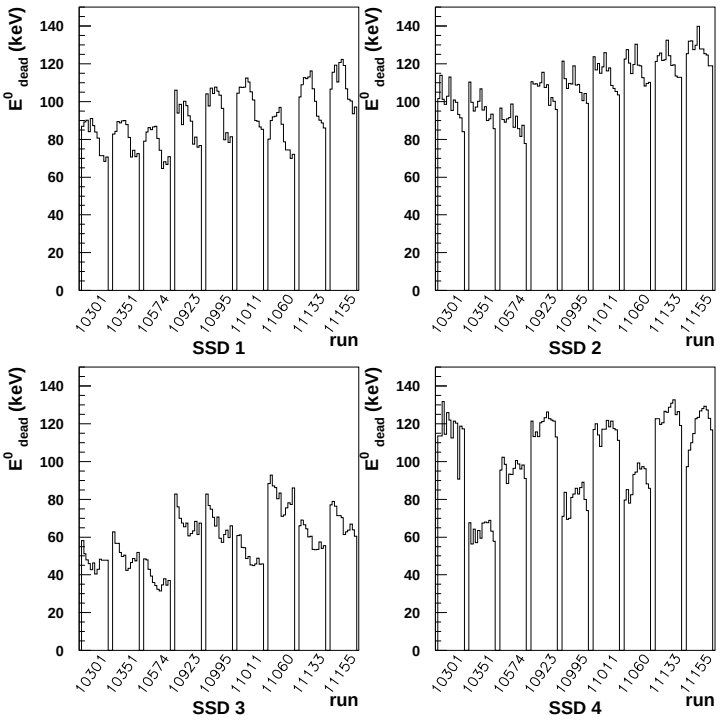


Figure 5.11: The $E^0_{dead}$ values extracted from the data for four SSDs from the 2004 run. The AGS CNI polarimeter run number is plotted on the $x$-axis. For each measurement, the $E^0_{dead}$ value is extracted for each of the 12 SSD strips.

A slightly different way of correcting for dead layer energy loss is used for off-line analysis. Again, the MSTAR program is used to describe the energy loss of carbon in silicon. However, the relation between $E_{kin}$ and $E_{dep}$ is fit using a fourth order polynomial, rather than a line. This gives

$$E_{kin} = p_0 + p_1 E_{dep} + p_2 E^2_{dep} + p_3 E^3_{dep} + p_4 E^4_{dep} \tag{5.7}$$

where the $p_n$ all depend on the dead layer thickness. Several values of $p_n$ are

generated for $20\mu\text{g/cm}^2 \leq t_{dead} \leq 100\mu\text{g/cm}^2$. The $t_{dead}$ dependence of each $p_n$ is then fit with a third order polynomial.

$$p_n(t_{dead}) = C_{n,0} + C_{n,1}t_{dead} + C_{n,2}t_{dead}^2 + C_{n,3}t_{dead}^3. \tag{5.8}$$

The 20 parameters, $C_{n,m}$, resulting from these fits can then be used to express $E_{kin}$ in terms of the measured amplitude, $Amp$, and the dead layer thickness, $t_{dead}$. Just as in the on-line method, the correlation between $t_{meas}$ and $Amp$ is fit from measured data, and parameters are extracted from the fit. For the off-line method, the free parameters extracted from the fit are $t_{dead}$ and $t_0$. The fundamental difference between the on-line and off-line dead layer correction methods is that more terms are used to relate $E_{kin}$ to $Amp$ for the off-line method. This provides a more accurate depiction of the energy loss behavior predicted by MSTAR.

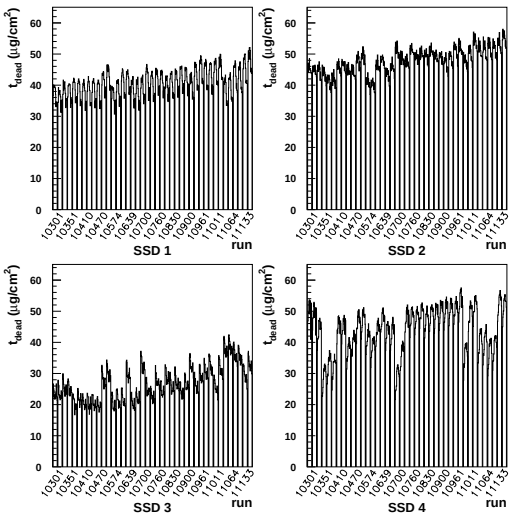


Figure 5.12: $t_{dead}$ versus polarimeter run number for four SSDs used during the 2004 running period. Several runs were selected to represent a sampling of the entire running period history. For the sake of readability not all run numbers are listed. As in Figure 5.11, 12 values corresponding to the 12 detector strips are plotted for each run.

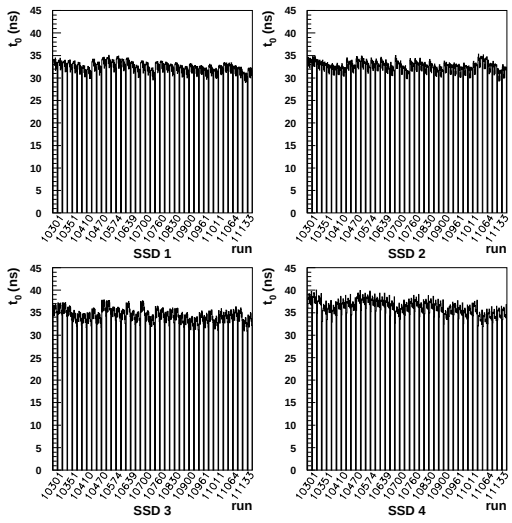


Figure 5.13: $t_0$ versus polarimeter run number. These values are taken from the same runs as those used for the $t_{dead}$ values shown in Figure 5.12. $t_0$ shows much less variation than $t_{dead}$.

Many measurements were studied off-line to determine the proper values for the parameters $t_{dead}$ and $t_0$. Figures 5.12 and 5.13 show $t_{dead}$ and $t_0$ values versus polarimeter run number. $t_0$ is fairly constant throughout the entire running period. While, $t_{dead}$ shows some fluctuations from run to run, particularly for SSD 3 and SSD 4. The root-mean-square (RMS) of the $t_{dead}$ distributions for all detectors vary from 2.5 to 6.5 $\mu$g/cm$^2$, which corresponds to approximately 5% to 14% variation. Another important feature of the $t_{dead}$ data is that $t_{dead}$ values from detector 3 are significantly less than those from the other detectors.

The values shown in Figures 5.12 and 5.13 are from data taken with one set of detectors (set A) used during the 2004 run. These detectors were replaced by another set of four detectors (set B) later in the run. $t_{dead}$ and $t_0$ values from each detector are fit with a constant to attain the best estimate of the parameters to be used in the final analysis. Table 5.1 displays the best estimates of $t_{dead}$ for both sets of detectors. The dead layer thickness is expected to be the similar for all

Table 5.1: $t_{dead}$ Best Estimates ($\mu$g/cm$^2$)

| | **SSD 1** | **S**SD 2 | **SSD 3** | **SSD 4** |
|---|---|---|---|---|
| **Set A** | 43.2 | 49.3 | 27.2 | 46.4 |
| **Set B** | 47.5 | 53.0 | 23.2 | 45.7 |

detectors; however, the estimated $t_{dead}$ values for SSD 3 are significantly less than the other detectors. The anomalously small $t_{dead}$ values for SSD 3 are present for both sets of detectors. This suggests that there may be some mechanism in the electronics or amplification chain, which is biasing the energy measurements in detector 3. However, the exact cause of these anomalously low $t_{dead}$ values is unclear.

To understand the effects of $t_{dead}$ on polarimeter measurements, data were analyzed using the values in Table 5.1 and then analyzed using adjusted values for SSD 3. For the second analysis, the average $t_{dead}$ of SSD 1, 2 and 4 were used for SSD 3. Changing $t_{dead}$ causes a shift in the reconstructed $E_{kin}$ spectra for detector 3. The measured asymmetry, $\varepsilon$, and effective analyzing power, $\langle A_N \rangle$, are both dependent on the $E_{kin}$ distribution, and therefore both are affected by the change in $t_{dead}$. The definitions of $\varepsilon$ and $\langle A_N \rangle$ and how they relate to the beam polarization, $P$, can be found in Appendix A.

The data analyzed using the $t_{dead}$ values shown in Table 5.1 were compared to those analyzed using the adjusted $t_{dead}$ for SSD 3. The relative changes in $P$, $\langle A_N \rangle$, and $\varepsilon$ between the two analyses are shown in Figure 5.14. For each analysis $P$, $\langle A_N \rangle$, and $\epsilon$ were calculated for many individual polarimeter measurements. The mean values of the change in $\langle A_N \rangle$ and $\epsilon$ are each less than 2%. This leads to shift in $P$ mean value of 2.9%. Although the $t_{dead}$ discrepancy for SSD 3 is significant, the overall systematic effect on the polarization is less than 3% for

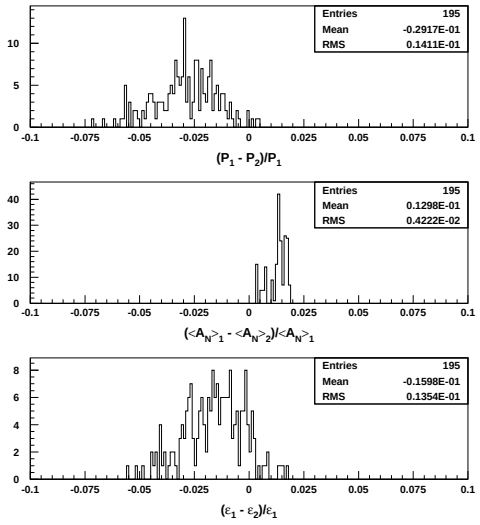


Figure 5.14: The above plots show the relative differences in $P$, $\langle A_N \rangle$, and $\epsilon$ for two different analysis methods. The relative differences are defined beneath each plot. The subscripts in the definitions represent the analysis method used to calculate the given quantity. Subscript 1 represents the analysis using the estimated $t_{dead}$ from Table 5.1. Subscript 2 represents the analysis using an adjusted $t_{dead}$ for SSD 3.

most measurements.

The on-line and off-line methods of correcting for dead layer energy loss both provide a process for reconstucting kinetic energy, $E_{kin}$, from measured event amplitudes, $Amp$. The off-line method provides a better fit to the energy loss behavior from MSTAR. There is also an off-line correction made for energy loss in the carbon target. (See Appendix B for a description.) The off-line method is used to determine the best estimate of the dead layer thicknesses, $t_{dead}$, for each detector used in the 2004 run. Although the estimated value of $t_{dead}$ varies from run to run and differs between the individual detectors, the effects on the measured beam polarization from these variations are small. The overall systematic effect on the polarization from the dead layer energy loss correction is less than 3%.

## 5.3 Off-line Studies and Systematic Effects

Several studies have been performed off-line in order to determine the level of systematic uncertainty in the AGS CNI polarimeter measurements. In order for the AGS CNI polarimeter to be effective, the measured asymmetries must be robust when subjected to a variety of different criteria. The goal of these studies is to determine how much $\varepsilon$ changes for different beam conditions and event selection techniques. These studies have focused mainly on effects from event pileup and non-carbon background contamination.

### 5.3.1 Event Pileup

Event pileup occurs when a proton bunch passes the carbon target and more than one recoil carbon event is incident on a single detector strip. If this occurs,

the WFD algorithm only finds the earliest arriving event. The event(s) arriving later is(are) lost. If event pileup occurs frequently, then the missed events can significantly alter the measured asymmetry. The measured event rates in the AGS CNI polarimeter suggest that the probability of event pileup is small. The event occupancy (*i.e.* number of events per bunch passing) is approximately 5% for the most populated detector strips. This estimate of event occupancy is based on measurements with beam intensity $\approx 1 \times 10^{11}$ protons per bunch. The probability of pileup increases at higher beam intensities. Measurements with a variety of different intensities have been studied to understand effects of event pileup.

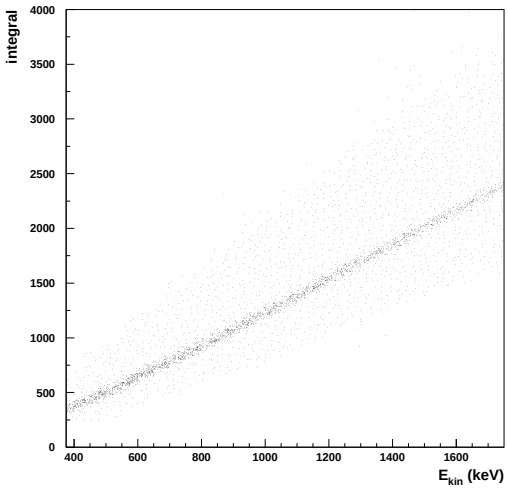


Figure 5.15: The measured charge integral vs. energy for events from a single detector strip. A $tof$-energy correlation cut has been applied to the data. The data are from a measurement taken with a relatively low beam intensity of approximately $0.3 \times 10^{11}$.

For each detected event the integrated charge is calculated by summing the measured amplitude of several adjacent time bins. The integral is well correlated with the event energy, as shown in Figure 5.15. When event pileup occurs, the

value of the integral is enhanced by the presence of multiple events. If significant pileup occurs the integral-energy correlation is affected. The integral-energy correlation was fit with a linear function for each detector strip for a number of measurements with different beam intensities. The slope parameters for each strip from two measurements, one with low intensity and one with high intensity, are plotted in Figure 5.16. Little change in the slope of the fit was observed for different intensities. Also, pileup is most likely to occur in the detector strips with the highest event rates. As seen in Figure 4.7, the central strips of each detector are much more populated than strips on the edges. There is, however, no clear dependence of the slope on strip number. These characteristics suggest that pileup effects are small.

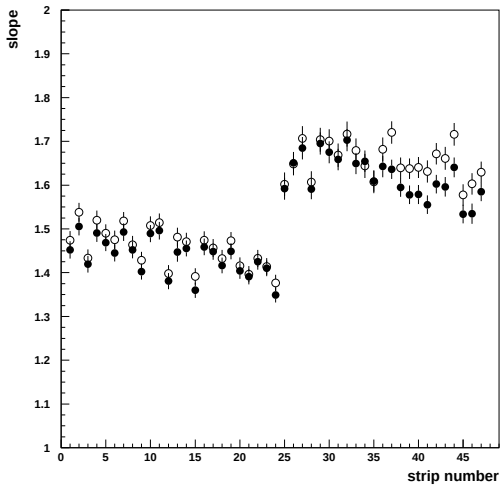


Figure 5.16: The slope from a linear fit to the integral-energy correlation vs. detector strip number. The open points correspond to a measurement with beam intensity of $1.9 \times 10^{11}$. The closed points are from data taken with $0.3 \times 10^{11}$ intensity. The slope is larger for detectors on the inner radius of the AGS (strip no. $\geq 37$). This may be because the inner detectors typically see more background events.

To determine the effect of event pileup on the measured asymmetry, asym-

metries with different strip selection were studied. As mentioned above, event pileup is expected to affect the most populated strips near the center of each detector. Asymmetries were calculated using events from only the two most populated strips from each detector. Asymmetries were also calculated with events from the outer two strips on either side of the central strips. (See Figure 5.17 for an illustration of the strip selection.) The ratio of asymmetries for the outer and central strips are plotted versus beam intensity in Figure 5.18. As beam inensity increases event pileup will affect the asymmetry from the central strips ($\varepsilon_{\text{central}}$) more than the asymmetry from the outer strips ($\varepsilon_{\text{outer}}$). The data in Figure 5.18 shows that the ratio of asymmetries is not strongly dependent on beam intensity. The measurements studied show that there is no significant effect on the asymmetry from event pileup.

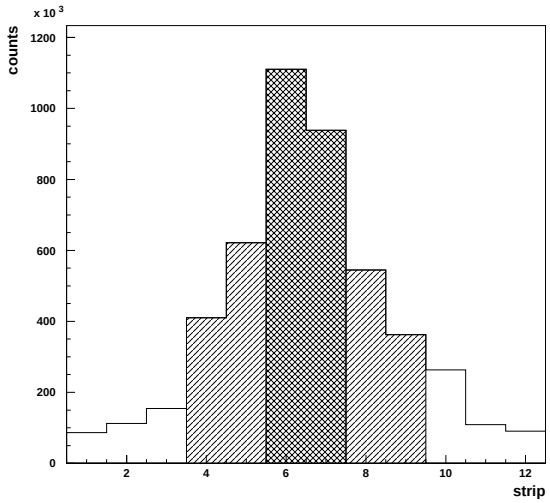


Figure 5.17: Example strip distribution used for pileup study. The shaded strips represent the two most populated strips for this particular detector. These are referred to as the central strips. The lined strips are the outer two strips on either side of the central strips. These are the outer strips.

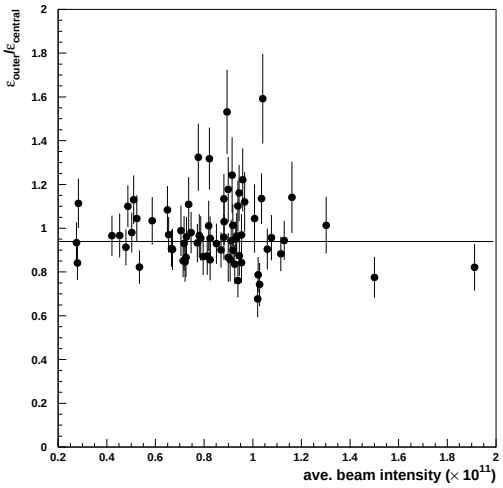


Figure 5.18: Ratio of asymmetries for the outer and central strips vs. the average beam intensity for each measurement. There is no obvious dependence on beam intensity. The number of measurements studied was limited because intensity was logged electronically only during the latter part of the 2004 run, and there were few measurements taken at high intensities. The line represents a constant fit to the data points.

### 5.3.2 Background Studies

To study the effect from non-carbon background, the mass of each detected particle is determined. The event mass, $m$, can be calculated from the measured energy, $E_{kin}$, and $tof$.

$$m = 2E_{kin}\left(\frac{tof}{l}\right)^2, \tag{5.9}$$

where $l$ is the distance from the target to the detector. Figure 5.19 shows an example of a mass distribution measured by one SSD. The carbon peak is clearly seen near 11 GeV/$c^2$. There is also a small peak near 4 GeV/$c^2$ from alpha particles. Although the amount of non-carbon background is low, studies have been performed to quantify the effects of the background on polarimeter measurements.

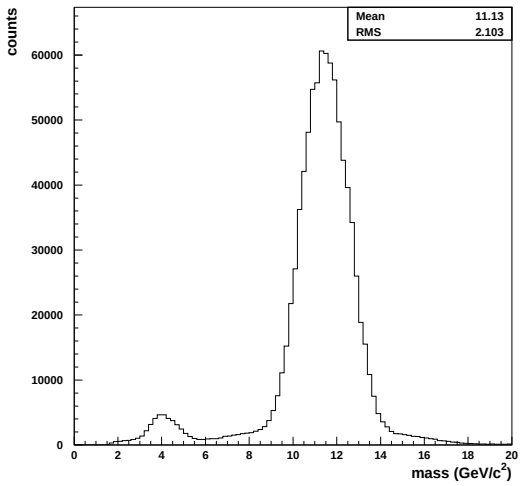


Figure 5.19: Mass distribution measured by one SSD during the 2004 run. The carbon peak is centered near the expected mass of 11.18 GeV/$c^2$. The mean and RMS of the distribution are displayed in the upper-right corner of the plot.

The level of background contamination beneath the carbon peak can be interpolated by fitting the entire mass distribution. The carbon peak can be fit well

with a gaussian funtion, but several functional forms have been used in attempts to accurately fit the non-carbon background. The best results were achieved using the following nine parameter function, $f(m)$, to fit the distribution:

$$f(m) = a_1 \exp\left(-\frac{1}{2}\left(\frac{m-a_2}{a_3}\right)^2\right) + a_4 \exp\left(-\frac{1}{2}\left(\frac{m-a_5}{a_6}\right)^2\right) + a_7 + \frac{a_8}{m} + \frac{a_9}{m^2}, \tag{5.10}$$

where the $a_n$ are the parameters of the fit. The first six parameters, $a_1$ through $a_6$, characterize two gaussian functions. Reasonable bounds are placed on these parameters so that they correspond to the alpha and carbon peaks. The background distribution is then given by subtracting the gaussian corresponding to the carbon peak. The background is given by the function, $b(m)$, below

$$b(m) = a_1 \exp\left(-\frac{1}{2}\left(\frac{m-a_2}{a_3}\right)^2\right) + a_7 + \frac{a_8}{m} + \frac{a_9}{m^2}. \tag{5.11}$$

$b(m)$ is integrated over the range of the carbon peak, from $\sim$ 8GeV/$c^2$ to $\sim$ 14GeV/$c^2$. The value of this integral is then subtracted from the integrated carbon peak, which gives an approximation to the background-free carbon yield.

The background subtraction technique described above was applied to several measurements from the 2003 and 2004 runs. The differences between asymmetries calculated with and without background subtraction was typically very small ($< 0.1\%$). The asymmetries from the subtracted background events were also calculated. These background asymmetries were usually small, but inconsistent results were found for some measurements. The size and shape of the background varies for different measurements and for different $-t$ bins within a measurement. These variations make the background difficult to fit and drive the inconsistencies in the background asymmetries. Because consistent results could not be achieved, the background subtraction technique was not applied to the final data analysis,

but results of this study suggest that the effect of the background is small.

Besides background subtraction other techniques were used to study background effects. These techniques compare asymmetries from different event selection cuts. The event selection was based on the values of $\mu$ and $\sigma$ from gaussian fits to the carbon mass peak. The usual cut selected events with mass between $\mu$-$2\sigma$ and $\mu$+$2\sigma$. Narrower and wider mass cuts were also studied. The mass distributions suggest that the concentration of background increases with cut width. Therefore, comparing asymmetries with different cut widths affords some information regarding background effects. Figure 5.20 shows the difference between asymmetries with widths of $\pm 1\sigma$, $\pm 2\sigma$, and $\pm 3\sigma$. The difference is small ($\sim 2\%$) for $|t| < 0.03(\mathrm{GeV}/c)^2$. At higher $|t|$, the asymmetry differences are larger and are as high as 30%. Also, asymmetries with narrower cuts are generally larger than those with wider cuts, suggesting that the background dilutes the asymmetry.

Another background study exploited the fact that the distribution of background events tends to decrease with mass. Asymmetries were calculated for events from a high mass region, $\mu < \text{mass} < \mu$+$2\sigma$, and a low mass region, $\mu - 2\sigma < \text{mass} < \mu$. These asymmetries were then compared to the asymmetry for the entire region, $\mu$-$2\sigma < \text{mass} < \mu$+$2\sigma$. Figure 5.21 shows an example of results from this study. The results are similar to those shown in Figure 5.20. These two studies suggest that non-carbon background events affect the asymmetry by a few percent for $|t| < 0.03(\mathrm{GeV}/c)^2$, and the effect is as high as 30% in the larger $|t|$ bins. Note that polarization values are calculated for the range $0.009(\mathrm{GeV}/c)^2 \leq -t \leq 0.022(\mathrm{GeV}/c)^2$. This study shows that the systematic effects from background are quite reasonable in this kinematic region.

The effects from background events can also be studied by comparing asymmetries from different detector strips. The number of detected carbon events

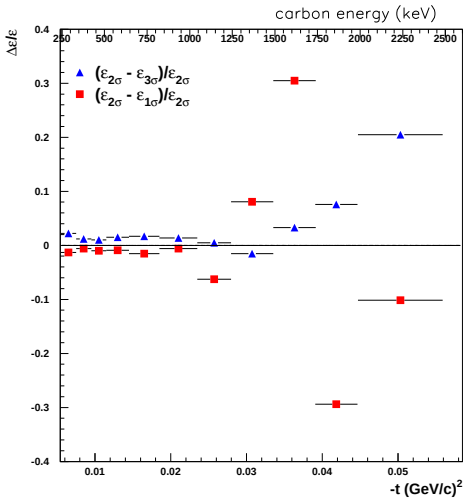


Figure 5.20: The relative difference between asymmetries with different width cuts vs. $-t$. Asymmetries with cut widths of $\pm 1\sigma$, $\pm 2\sigma$, and $\pm 3\sigma$ were calculated. The differences are small ($\sim 2\%$) for $|t| < 0.03(\mathrm{GeV}/c)^2$. For the higher $|t|$ bins, the difference is as large as 30%. The asymmetries were calculated from a group of $\sim 15$ adjacent measurements from the 2004 run. Other data studied exhibit similar trends.

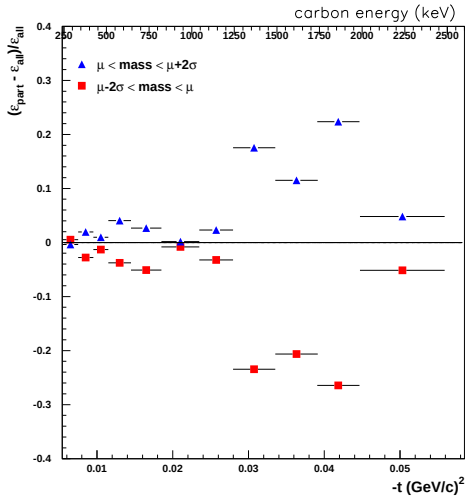


Figure 5.21: The relative difference between asymmetries from different mass regions vs. $-t$. In the $y$-axis label, $\varepsilon_{part}$ represents the asymmetry from one of the two mass regions defined in the plot key. $\varepsilon_{all}$ is the asymmetry for the entire mass region. The results are similar to those shown in Figure 5.20. The data are summed over a group of $\sim 25$ individual measurements. Other data studied have comparable results.

varies significantly for central strips compared to outer strips. Accordingly, the ratio of carbon to background events is expected to vary with strip. By comparing asymmetries with different strip selection the effects of background contamination can be determined. This technique is also sensitive to event pileup since pileup primarily occurs in central strips.

Asymmetries with several different strip selection criteria were studied. When compared to previous background studies or dead layer thickness studies, the asymmetry was found to be more sensitive to the strip selection criteria. To determine the systematic effect on the asymmetry two different strip selection criteria were compared. The first criterion selected events from the three most populated strips of each detector, and the second extended the selection to include events from the seven most populated strips of each detector.

The relative difference in $\varepsilon$ for the two strip selection techniques varied for the many individual measurements studied, but the mean difference was approximately 3.6%. This difference corresponds to $\varepsilon$ calculated for the range $0.009(\mathrm{GeV}/c)^2 \leq -t \leq 0.022(\mathrm{GeV}/c)^2$. Asymmetries at lower and higher $-t$ showed larger differences. Figure 5.22 shows the relative difference in $\varepsilon$ versus $-t$. The differences were fit with constant functions for different ranges in $-t$. The values of these fits are taken as the level of systematic uncertainty for the corresponding $-t$ range. The data shown in Figure 5.22 represents the sum of several measurements taken with beam energy of 24.3 GeV. The same procedure was used to determine systematic uncertainty of measurements at other beam energies.

The asymmetries measured by the AGS CNI polarimeter have been shown to be robust under different event selection criteria. The asymmetry is most sensitive to strip selection criteria. The data suggests that there is little effect on

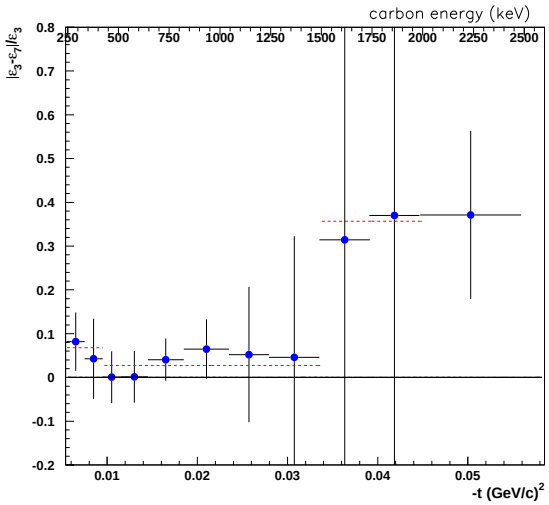


Figure 5.22: Relative difference in $\varepsilon$ vs. $-t$ for two different strip selection criteria. $\varepsilon_{3(7)}$ represents the asymmetry using only events from the three (seven) most populated detector strips. The dashed lines represent constant fits to the data at different $-t$ ranges. The measurements represented by the data in this plot were taken to study the $-t$ dependence of $A_N$ at beam energy 24.3 GeV. These results are discussed further in Section 6.2.

$\varepsilon$ from event pileup, but the dead layer energy correction and background events both contribute to the systematic uncertainty of the polarimeter. These effects produce a $\sim 4\%$ systematic uncertainty in the measured asymmetry.

# CHAPTER 6

# Results

During the 2003 and 2004 running periods, the AGS CNI polarimeter provided thousands of individual measurements of the beam polarization. Using the feedback from these measurements accelerator physicists were able to tune various magnet strengths and frequencies for optimal polarization output. Significant improvement to the beam polarization was made during the 2003 run. On-line polarization values from the 2003 and 2004 runs are plotted in Figure 6.1 and Figure 6.2 respectively. The beam polarization increased from less than 20% at the time of installation of the polarimeter to consistently being near 50% during the 2004 run. In addition to providing polarization measurements at AGS extraction energy, the CNI polarimeter was used to measure asymmetries while the beam was accelerated. These data were used to study the evolution of the beam polarization during the AGS acceleration cycle. The polarimeter was also used to study the proton-carbon analyzing power at a number of beam energies. These results are presented in the sections below.

## 6.1 Asymmetry Measurement during AGS Acceleration

For a typical polarization measurement, the AGS CNI polarimeter detects scattered carbon events only after the proton beam has been accelerated and held at a particular flattop energy. However, the polarimeter was also used to characterize

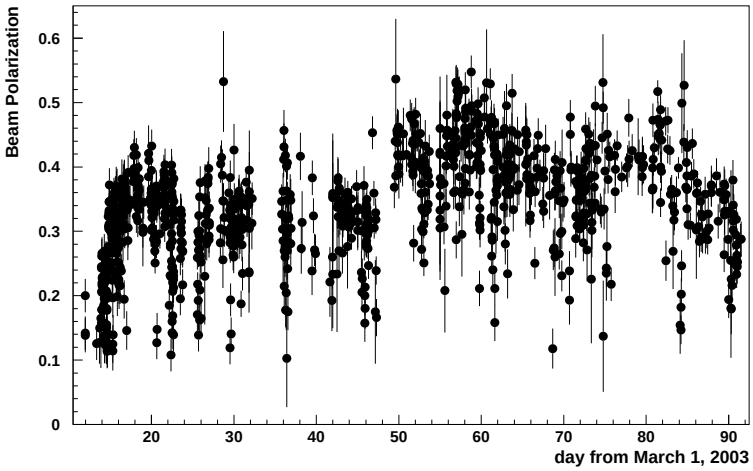


Figure 6.1: On-line beam polarization measurements for the 2003 running period as measured by the AGS CNI polarimeter. The polarization generally increased throughout the run. Rapid improvement in the polarization was seen in the first week after the polarimeter commisioning (March 13 - 19, 2003).

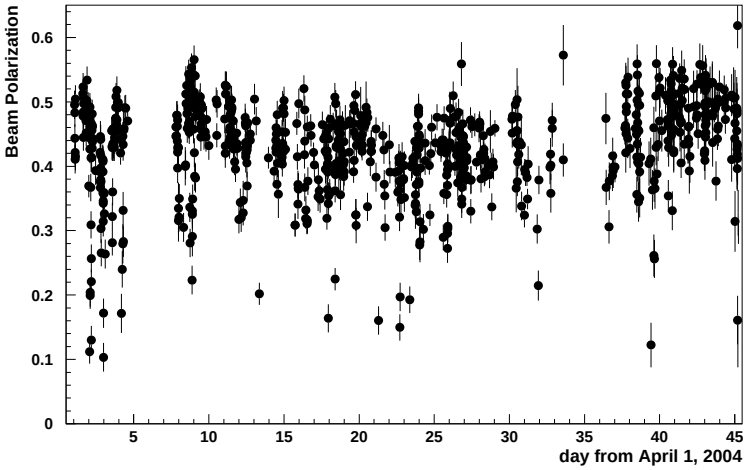


Figure 6.2: On-line beam polarization measurements for the 2004 running period as measured by the AGS CNI polarimeter. Polarization values increased relative to the 2003 run. This increase is even more pronounced when considering that the revised analyzing power used in 2004 increased by $\sim 10\%$. (See Appendix A.2.)

the polarization of the beam as it was being accelerated. For these measurements the polarimeter target was inserted into the beam during the early part of acceleration cycle, and the target remained in the beam throughout the acceleration up to AGS extraction energy. As mentioned in Section 4.3, each detected event is associated with a Gauss Clock Count, which is proportional to the beam momentum. Detected events are collected into narrow momentum bins (50 MeV/$c$ wide). Asymmetries are then calculated for each bin. The asymmetries provide information about the behavior of the beam polarization relative to the momentum of the beam.

Figure 6.3 shows the measured asymmetry versus the parameter $G\gamma$ ($G\gamma \approx 1.9\times$ beam energy in GeV). The sign of the asymmetry changes each time $G\gamma$ is equal to an integer. This is consistent with the proton spin direction behavior described in Section 3.2. The spin direction flips when each imperfection resonance is crossed at $G\gamma =$ integer. The data in Figure 6.3 also shows that the spin direction flips when three strong intrinsic resonances are crossed at $G\gamma = 12+\nu_z$, $36-\nu_z$, and $36+\nu_z$ (where $\nu_z \approx 8.7$). The early part of the acceleration cycle could not be measured with the AGS CNI polarimeter. This was due to changes in the beam position at lower energies. The polarimeter target was stationary during the measurements, but the beam position usually moves as the beam is accelerated. An acceleration cycle was designed so that the beam position was held stable during acceleration, but this was only achievable for beam energies $>\sim 10$ GeV.

The data in Figure 6.3 shows that the magnitude of the asymmetry decreases as the beam energy increases. To better illustrate this dependence, the asymmetries measured during acceleration were averaged for each spin flip. Data taken during or very near a resonance crossing was not included in the average value.

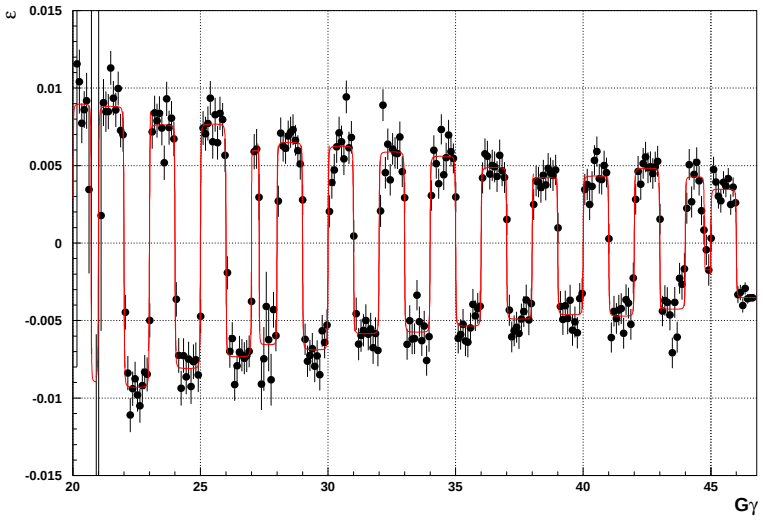


Figure 6.3: Measured asymmetry versus $G\gamma$. The sign of the asymmetry changes when resonance conditions are crossed. The solid line is a model of the expected behavior of the beam polarization. The amplitude of the model is fit to the data. The error bars are statistical only. These data were accumulated during three eight-hour shifts from April 13 to April 16, 2003. The data comprise measurements from approximately 5000 individual acceleration cycles.

The magnitude of the average $\varepsilon$ versus beam energy from both 2003 and 2004 data is shown in Figure 6.4. The decrease in $\varepsilon$ is only partially due to loss of polarization as the beam is accelerated. Measurements at various beam energies in the AGS have shown that the analyzing power also decreases with beam energy. The exact energy dependence of the analyzing power is not known, but an estimate can be determined by interpolating between the energies where the analyzing power has been measured.

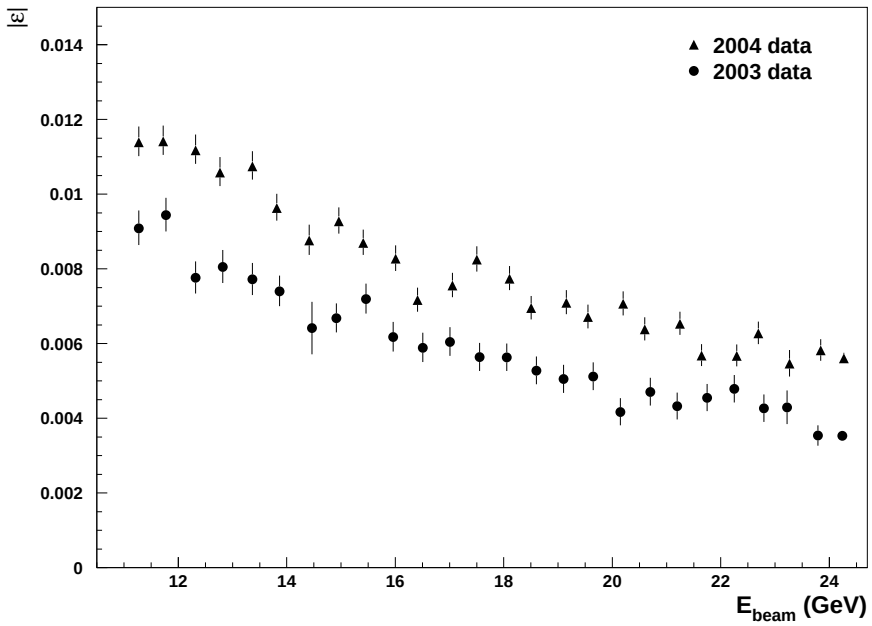


Figure 6.4: The magnitude of $\varepsilon$ versus beam energy. Data from the 2003 run (circles) and the 2004 run (triangles) are shown. The decrease in $\varepsilon$ with beam energy is due to polarization loss as well as the decreasing analyzing power. The error bars include an estimate of systematic error based on variations from strip selection and carbon energy corrections. $\varepsilon$ is measured over the range $0.009(\mathrm{GeV}/c)^2 \leq -t \leq 0.022(\mathrm{GeV}/c)^2$.

Using the E880 polarimeter for an independent measure of beam polarization, the analyzing power of the AGS CNI polarimeter was determined at beam ener-

gies of 9.7, 12.8, 16.0, 21.7, and 24.3 GeV. For each beam energy, an effective analyzing power, $(A_N)_{eff}$, is calculated by dividing $\varepsilon$ measured for $0.009(\mathrm{GeV}/c)^2 \leq -t \leq 0.022(\mathrm{GeV}/c)^2$ by the beam polarization. A simple model of the energy dependence of $(A_N)_{eff}$ is used to estimate the polarization during the AGS acceleration. The $(A_N)_{eff}$ is assumed to decrease linearly with beam energy from about 10 GeV to 18.5 GeV. For energies greater than 18.5 GeV, $(A_N)_{eff}$ is taken to be constant. A graphical representation of this model of $(A_N)_{eff}$ is shown in Figure 6.5. Using the model of $(A_N)_{eff}$, the asymmetries shown in Figure 6.4 can be translated to beam polarizations. The beam polarization versus beam energy is plotted in Figure 6.6. The polarization shows a general trend of decreasing with beam energy. An exact interpretation of the polarization behavior cannot be made due to the large uncertainty in $(A_N)_{eff}$. The uncertainty in $(A_N)_{eff}$ translates to uncertainties in $P$ of $\pm 10\%$ to $\pm 20\%$.

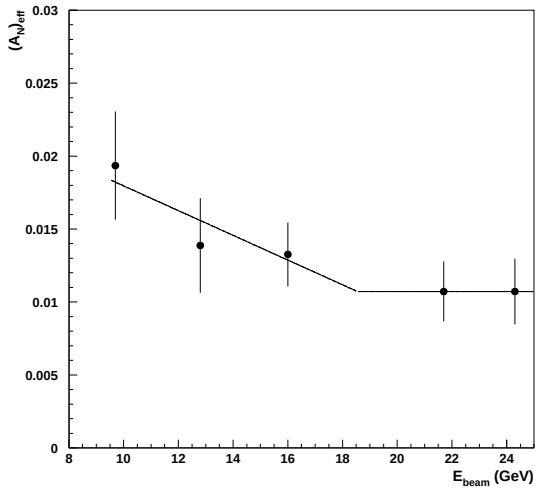


Figure 6.5: $(A_N)_{eff}$ versus beam energy. The line represents a simple model of the beam energy dependence of $(A_N)_{eff}$. The points are measurements of $(A_N)_{eff}$ with the AGS CNI polarimeter. The E880 polarimeter was used to provide an independent measure of beam polarization. The large error bars are primarily due to the error in the calibration of the E880 polarimeter.

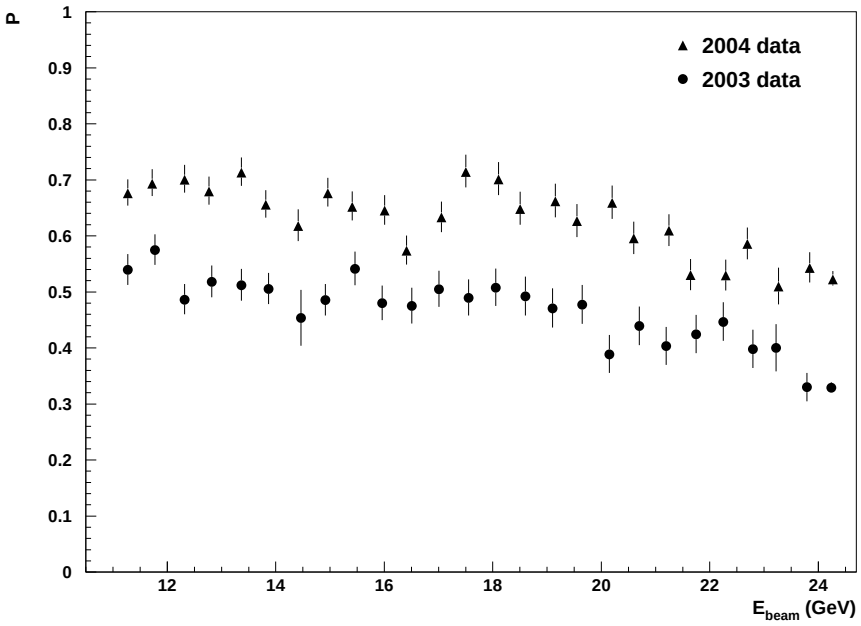


Figure 6.6: Beam polarization versus beam energy. Both the 2003 and 2004 data show a gradual decrease of polarization with beam energy. The error bars do not include the uncertainty from the analyzing power. The large uncertainty in the analyzing power produces a large uncertainty in polarization. $\Delta P$ varies from $\pm 10\%$ to $\pm 20\%$.

## 6.2 $-t$ Dependence of $A_N$

The AGS CNI polarimeter has provided a wealth of data used to study the analyzing power for $pC$ elastic scattering at low momentum transfer. For both the 2003 and 2004 running periods, several measurements were made at various beam energies using the AGS CNI polarimeter and the E880 polarimeter concurrently. The E880 polarimeter provided an independent monitor of the beam polarization, which made it possible to extract the analyzing power, $A_N$, from the CNI polarimeter measured asymmetries. For these measurements, both polarimeters sampled the beam for a portion of each AGS cycle. The beam was accelerated to the desired energy. The CNI polarimeter would acquire date for a given time period. Then, the E880 polarimeter would acquire data during the remainder of the cycle. The CNI and E880 targets were only moved into the beam when the respective polarimeter was acquiring data.

For the 2004 running period, measurements in parallel with the E880 polarimeter were made at four beam energies: 3.9 GeV, 6.5 Gev, 16.0 GeV, and extraction energy 24.3 GeV. The asymmetries from these measurements are plotted versus $-t$ in Figure 6.7. These data incorporate the corrections discussed in Chapter 5. The non-linear correction to the dead layer energy loss is used. A correction for energy lost while scattered carbons exit the target is also made. The event selection was based on a fit to the carbon mass peak. A $2\sigma$ cut was used for most of the data. (See Section 5.3.2 for a description of cuts.) The proton beam at 3.9 GeV has a longer bunch length than at the higher beam energies. This results in a widening of the mass distributions for the 3.9 GeV data. For these data, narrower cuts of $1.5\sigma$ and $1\sigma$ were used.

To understand the systematic effects of the AGS CNI polarimeter, the sensi-

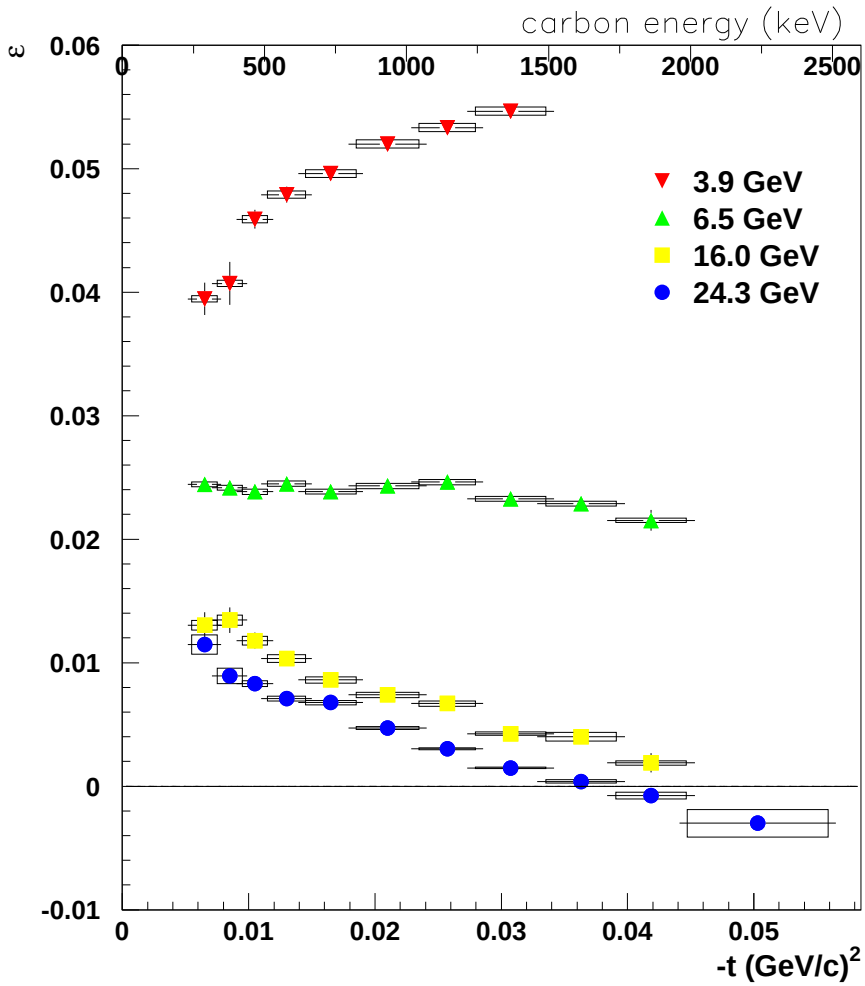


Figure 6.7: Measured asymmetry, $\varepsilon$, versus $-t$ from the 2004 run. The asymmetries were measured at four different beam energies, which are indicated on the plot. The vertical error bars represent the statistical error. For most points the statistical error is smaller than the size of the marker. The error rectangles represent the systematic error in the asymmetries (vertical) and the bin width in $-t$ (horizontal). The error in the bin width is represented by the horizontal error bars.

tivity to several parameters and event selection criteria were studied. The measured asymmetries were found to be most sensitive to the selection of different detector strips. The systematic errors of the data shown in Figure 6.7 are based on the variation in $\varepsilon$ to different strip selection. Asymmetries were calculated using data from only the three most populated strips from each detector. These were compared to asymmetries using the seven most populated strips from each detector. The systematic error is based on the ratio of the two asymmetries. (See Figure 5.22.) For the lower beam energy data (3.9 GeV and 6.5 GeV), part of the strip distribution was outside of the detector acceptance. For these data, narrower strip selection criteria were defined.

For $pC$ elastic scattering, the momentum transfer squared, $-t$, is proportional to the kinetic energy of the scattered carbon, as in Equation 5.2. The uncertainty in the carbon energy, and consequently in $-t$, is primarily due to the correction for energy lost in the silicon dead layer. The value of the dead layer thickness extracted from data varied by as much as $\pm 6.5$ $\mu$g/cm$^2$. This uncertainty in the dead layer thickness can be translated to an uncertainty in $E_{kin}$. At $E_{kin} = 300$ keV, the uncertainty is $\pm 15$ keV. At higher energies, the error increases. For $E_{kin} = 2200$ keV, the uncertainty is approximately $\pm 30$ keV. This uncertainty in $E_{kin}$ is used to determine the width of the horizontal error bars in Figure 6.7.

The analyzing power is determined by dividing the asymmetries in Figure 6.7 by the beam polarization measured by the E880 polarimeter. The measured beam polarizations are displayed in Table 6.1. The analyzing power, $A_N$, is plotted versus $-t$ in Figure 6.8. Both the scale of the analyzing power and the $-t$ dependence shape show a dependence on the beam energy. The $A_N$ peaks at approximately 6.5% at beam energy of 3.9 GeV. Within the measured $-t$ range, the maximum value of $A_N$ only reaches 2% at extraction energy, 24.3

Table 6.1: Measured Beam Polarizations and Analyzing Powers for the E880 Polarimeter used during the 2004 Run.

| $E_{beam}$ [GeV] | Date | $P[\times 10^{-2}]$ | $A_N^{E880}[\times 10^{-2}]$ | $A_N^{E880}$ Reference |
|---|---|---|---|---|
| 3.9 | May 10,11, 2004 | 83.24 ± 5.30 | 4.56 ± 0.29 | [34] |
| 6.5 | May 2,14 2004 | 63.58 ± 7.34 | 3.12 ± 0.36 | [43] |
| 16.0 | May 7,8, 2004 | 66.81 ± 10.74 | 0.94 ± 0.15 | [36] |
| 24.3 | May 11,13, 2004 | 58.03 ± 12.07 | 0.58 ± 0.12 | [36] |

GeV. At 3.9 GeV, $A_N$ increases with $-t$, and $A_N$ is nearly constant with $-t$ at 6.5 GeV. At larger beam energies, $A_N$ decreases with $-t$, which is consistent with the behavior observed in the E950 experiment [2]. The values of $A_N$ and errors plotted in Figure 6.8 can be found in Appendix C.

The analyzing power was also measured during the 2003 running period for a number of beam energies. Measurements were made at 3.9, 6.5, 21.7, and 24.3 GeV. The systematic errors were attained in the same way as described above for the 2004 data. $A_N$ versus $-t$ from the 2003 running period is shown in Figure 6.9. The polarization values used to extract $A_N$ from the measured asymmetries are shown in Table 6.2. The measurements of the analyzing powers at energies 3.9, 6.5, and 24.3 GeV are consistent with those measured during the 2004 run.

While $A_N$ changes very rapidly with beam energy at low energies in the AGS, the energy dependence of $A_N$ becomes quite small as the beam energy increases. The data in Figure 6.9 suggests that there is no difference in $A_N$ at 21.7 GeV and 24.3 GeV. The 24.3 GeV measurement was limited to $-t < 0.0235(\mathrm{GeV}/c)^2$ during 2003, but the range was extended to $-t$ of 0.05 $(\mathrm{GeV}/c)^2$ for 2004. A comparison of the 2003 21.7 data and the 2004 24.3 data shows that the two are consistent over the entire measured range in $-t$. The $A_N$ at 24.3 GeV from the

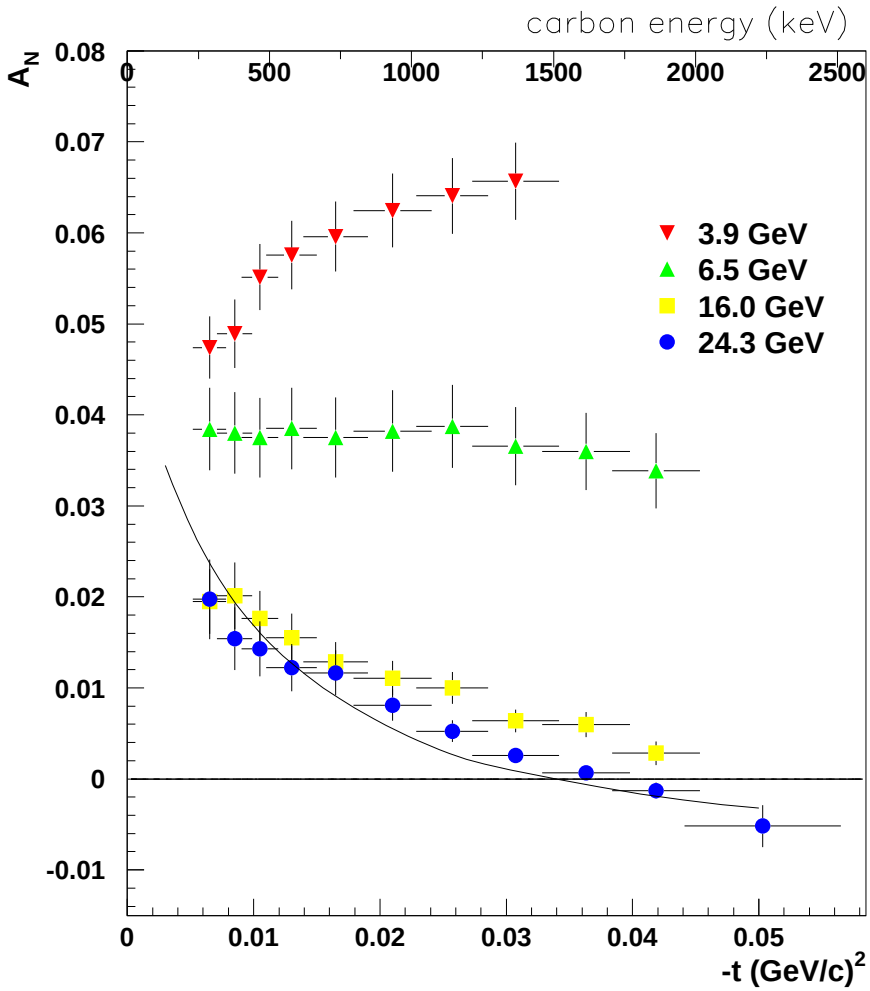


Figure 6.8: Analyzing power, $A_N$, versus $-t$ from the 2004 run. The beam energies of each measurement are indicated on the plot. The solid line represents a theoretical fit to the E950 data [4]. The error bars are given by the statistical error and systematic error added in quadrature.

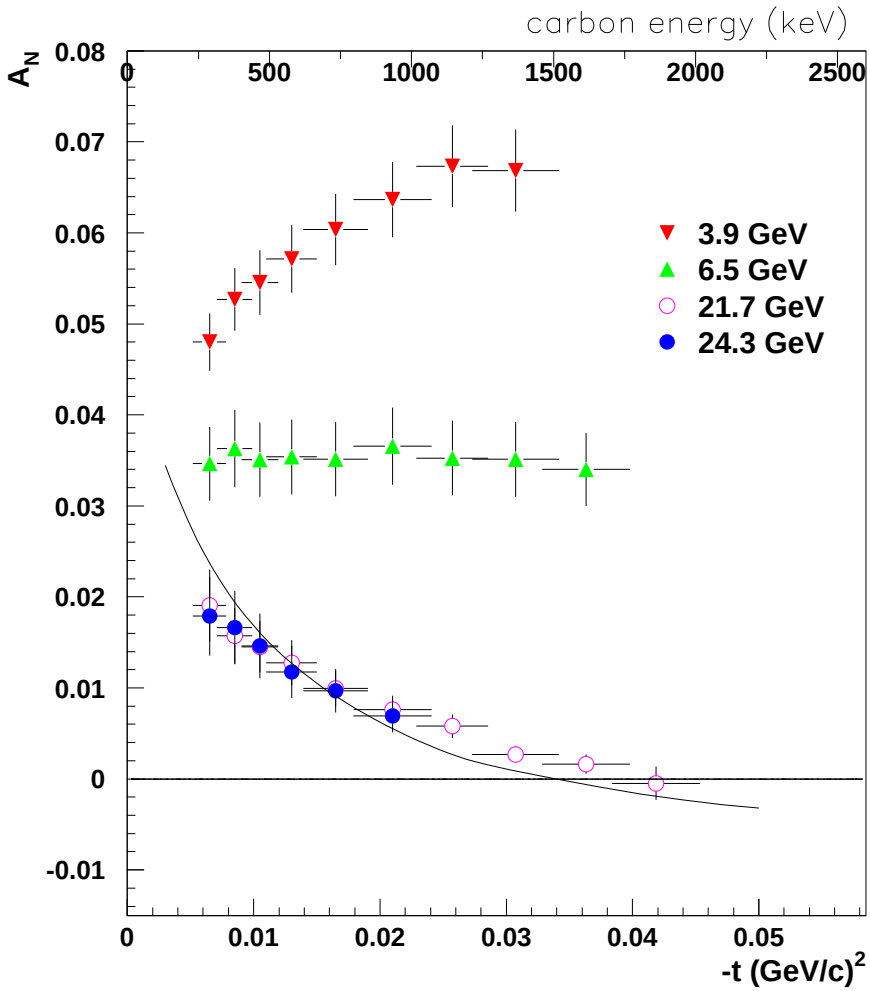


Figure 6.9: Analyzing power, $A_N$, versus $-t$ from the 2003 run. The beam energies of each measurement are indicated on the plot. The solid line represents a theoretical fit to the E950 data [4]. The error bars are given by the statistical error and systematic error added in quadrature.

Table 6.2: Measured Beam Polarizations and Analyzing Powers for the E880 Polarimeter used during the 2003 Run.

| $E_{beam}$ [GeV] | Date | $P[\times 10^{-2}]$ | $A_N^{E880}[\times 10^{-2}]$ | $A_N^{E880}$ Reference |
|---|---|---|---|---|
| 3.9 | May 15, 2003 | 73.62 ± 4.69 | 4.56 ± 0.29 | [34] |
| 6.5 | May 17,21 2003 | 57.05 ± 6.60 | 3.12 ± 0.36 | [43] |
| 21.7 | May 27,28, 2003 | 48.84 ± 9.39 | 0.69 ± 0.13 | * |
| 24.3 | May 29, 2003 | 31.03 ± 7.06 | 0.58 ± 0.12 | [36] |

* *The analyzing power at this energy was interpolated from the measurements at other energies.*

2004 run and the $A_N$ at 21.7 GeV and 24.3 GeV from the 2003 run are plotted in Figure 6.10. The points from the E950 measurement are also plotted in the figure. The measurements of $A_N$ with the AGS CNI polarimeter are consistent with the E950 result.

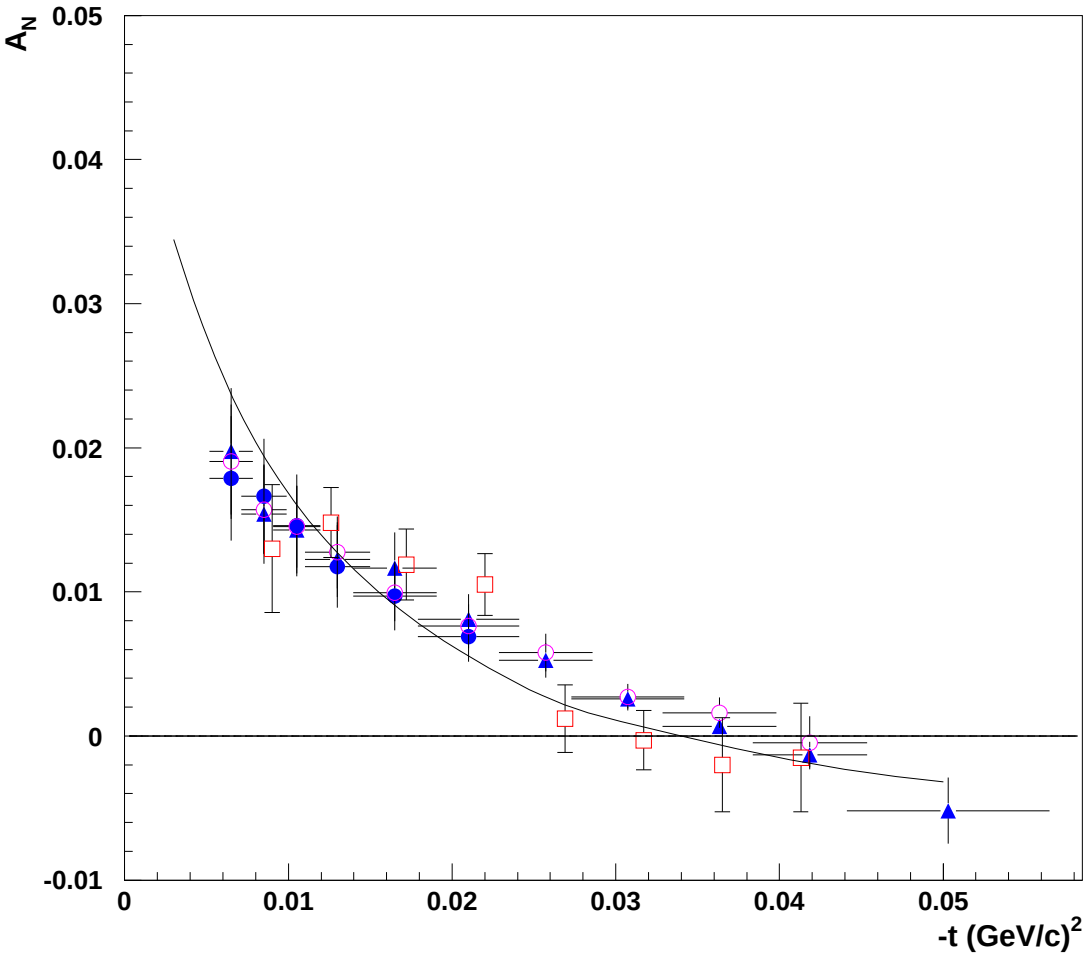


Figure 6.10: $A_N$ vs. $-t$. The circles represent the $A_N$ from the CNI polarimeter measured during the 2003 run at beam energies of 21.7 GeV (open circles) and 24.3 GeV (closed circles). The 2004 measurement at 24.3 GeV (triangles) is also shown. The open square points are the E950 data. There error bars on the E950 data are from statistical and systematic errors added in quadrature. The solid line represents a fit to the E950 data [4].

# CHAPTER 7

# Conclusions

We have successfully built and operated an AGS CNI polarimeter, which has served and continues to serve as a valuable diagnostic tool, helping to advance the RHIC Spin Program toward the goal of measuring the gluon polarization. Several types of useful measurements are provided by the polarimeter. The polarimeter is used to monitor the polarization output to RHIC. A few thousand measurements of the beam polarization at AGS extraction energy have been made. The polarimeter is also used to study polarization at lower beam energies in the AGS, including measurements during acceleration of the beam. In addition, the AGS CNI polarimeter is used to measure the analyzing power of proton-carbon elastic scattering at a number of beam energies ranging from 3.9 GeV to 24.3 GeV. The information provided by these measurements is essential to the continued progress of the RHIC Spin Program.

The primary function of the AGS CNI polarimeter is to measure and monitor the beam polarization prior to injection into RHIC. The polarimeter can measure the polarization to within 5% statistical uncertainty for a reasonable measurement time of $\sim$ 8 min. A robust system of quality assurance criteria helps to ensure the accuracy of polarization measurements. Off-line studies have also shown that the measured asymmetry shows little variation with different event selection cuts. The main contributions to the asymmetry systematic error are due to background

events and corrections to the recoil carbon energy. Estimates of the systematic uncertainty in the measured asymmetry are small, approximately 4%. These qualities make CNI polarimetry an effective method of polarimetry for the AGS.

Besides monitoring the polarization at extraction energy, the CNI polarimeter is also useful for characterizing the beam polarization at lower beam energies. Although the analyzing power may not be known at a given beam energy, the polarimeter can still provide relative polarization information. This enables accelerator physicists to tune the acceleration cycle for maximum polarization output. Also, the polarimeter is able to measure asymmetries while the beam is being accelerated. This novel technique allows one to see the evolution of the polarization as the beam is ramped from $\sim$ 10 GeV to 24.3 GeV. Because the AGS CNI polarimeter can provide polarization information at several beam energies quickly and accurately, it has been vital to the significant polarization improvement achieved in the AGS.

The CNI polarimeter is also used to measure the proton-carbon elastic scattering analyzing power, $A_N$, at a number of beam energies. Using the E880 polarimeter for an independent measure of the beam polarization, $A_N$ has been measured at: 3.9 GeV, 6.5 GeV, 9.7 GeV, 12.8 GeV, 16.0 GeV, 21.7 GeV, and 24.3 GeV. These measurements will allow beam polarizations to be extracted from future asymmetry measurements at these energies. In addition to this practical use of $A_N$ for polarimetry, the $-t$ dependence of $A_N$ has been studied for the different beam energies.

The $A_N$ measured by this experiment was compared to the measurement from the E950 experiment. The $A_N$ at beam energies 21.7 GeV and 24.3 GeV are consistent with E950 and also are consistent with a model of $A_N$ that includes a nonzero hadronic spin-flip contribution [18]. With respect to the E950

measurement, the measurements with the CNI polarimeter have extended the kinematic range and improved the statistical and systematic uncertainties of $A_N$, with the largest contribution to the uncertainty coming from the measurement of polarization.

The measured $A_N$ at 21.7 GeV and 24.3 GeV exhibits a $-t$ dependence that decreases with $-t$. At lower beam energies, both the magnitude and shape of the $-t$ dependence change significantly. As beam energy decreases, the magnitude of $A_N$ increases and the $-t$ dependence flattens. At 6.5 GeV, $A_N$ is nearly constant in $-t$, and measurements at 3.9 GeV show $A_N$ increasing with $-t$.

In summary, the measurements of the AGS CNI polarimeter provide valuable information for the RHIC Spin Program. The polarimeter is used as a monitor of the beam polarization injected to RHIC. The measurements of the polarimeter have small systematic uncertainty and good statistical precision for a reasonable measurement time. The asymmetry measurements have been shown to be robust. Measurements at various beam energies and during beam acceleration are extremely useful diagnostic tools for improving the polarization output to RHIC. The polarimeter has provided measurements of the $-t$ dependence of $A_N$ at several beam energies. The AGS CNI polarimeter has improved the knowledge of the proton-carbon elastic scattering analyzing power at low momentum transfer and has become an indispensable tool for the advancement of the RHIC Spin Program.

# APPENDIX A

# Asymmetry and Analyzing Power Formulae

The asymmetries and effective analyzing power used for the AGS CNI polarimeter are defined here. The so-called *square-root formula*, as first described in Reference [44], is used to calculate asymmetries.

## A.1 Square-root Asymmetries

The asymmetries are calculated from the number of measured events, which are measured directly using left and right detector arms. The number of measured events can be related to properties of the beam, the detectors, and the analyzing power for the process as follows:

$$\begin{aligned} N_L^{\uparrow} &= B^{\uparrow} d\Omega_L (1 + P^{\uparrow} A_{NL}) \\ N_L^{\downarrow} &= B^{\downarrow} d\Omega_L (1 - P^{\downarrow} A_{NL}) \\ N_R^{\uparrow} &= B^{\uparrow} d\Omega_R (1 - P^{\uparrow} A_{NR}) \\ N_R^{\downarrow} &= B^{\downarrow} d\Omega_R (1 + P^{\downarrow} A_{NR}), \end{aligned} \tag{A.1}$$

where $N_{L(R)}^{\uparrow(\downarrow)}$ is the number of events detected in the left (right) detector arm with the beam in the up (down) polarization state. The integrated beam intensity is $B^{\uparrow(\downarrow)}$, and the beam polarization is $P^{\uparrow(\downarrow)}$ for the up (down) polarization state. $d\Omega_{L(R)}$ is the solid angle times efficiency, and $A_{NL(R)}$ is the analyzing power for the

left (right) detector arm. The mean values and asymmetries of these quantities are given by the expressions:

$$\begin{aligned} B &= (B^{\uparrow} + B^{\downarrow})/2 \\ \varepsilon_B &= \frac{B^{\uparrow} - B^{\downarrow}}{B^{\uparrow} + B^{\downarrow}} \\ P &= (P^{\uparrow} + P^{\downarrow})/2 \\ \varepsilon_P &= \frac{P^{\uparrow} - P^{\downarrow}}{P^{\uparrow} + P^{\downarrow}} \\ d\Omega &= (d\Omega_L + d\Omega_R)/2 \\ \varepsilon_\Omega &= \frac{d\Omega_L - d\Omega_R}{d\Omega_L + d\Omega_R} \\ A_N &= (A_{NL} + A_{NR})/2 \\ \varepsilon_A &= \frac{A_{NL} - A_{NR}}{A_{NL} + A_{NR}}. \end{aligned} \tag{A.2}$$

The measured asymmetry used for the AGS CNI polarimeter is defined as

$$\varepsilon = \frac{\sqrt{N_R^{\uparrow} N_L^{\downarrow}} - \sqrt{N_R^{\downarrow} N_L^{\uparrow}}}{\sqrt{N_R^{\uparrow} N_L^{\downarrow}} + \sqrt{N_R^{\downarrow} N_L^{\uparrow}}}. \tag{A.3}$$

Two other asymmetries, $\varepsilon_{acc}$ and $\varepsilon_{lum}$, are also calculated. These are used to study the systematic effects from differences in the left and right detector acceptances and from differences in up and down polarization states. $\varepsilon_{acc}$ and $\varepsilon_{lum}$ are defined as

$$\varepsilon_{acc} = \frac{\sqrt{N_R^{\uparrow} N_R^{\downarrow}} - \sqrt{N_L^{\uparrow} N_L^{\downarrow}}}{\sqrt{N_R^{\uparrow} N_R^{\downarrow}} + \sqrt{N_L^{\uparrow} N_L^{\downarrow}}}, \tag{A.4}$$

$$\varepsilon_{lum} = \frac{\sqrt{N_R^{\uparrow} N_L^{\uparrow}} - \sqrt{N_R^{\downarrow} N_L^{\downarrow}}}{\sqrt{N_R^{\uparrow} N_L^{\uparrow}} + \sqrt{N_R^{\downarrow} N_L^{\downarrow}}}. \tag{A.5}$$

The statistical error of the asymmetries in Equations A.3, A.4, and A.5 is given

by

$$\sigma_\varepsilon = \frac{\sqrt{N_R^\uparrow N_L^\downarrow (N_R^\downarrow + N_L^\uparrow) + N_R^\downarrow N_L^\uparrow (N_R^\uparrow + N_L^\downarrow)}}{\left(\sqrt{N_R^\uparrow N_L^\downarrow} + \sqrt{N_R^\downarrow N_L^\uparrow}\right)^2}. \tag{A.6}$$

Note that if the asymmetries are small then the four event yields are all approximately equal, $N_R^\uparrow \approx N_R^\downarrow \approx N_L^\uparrow \approx N_L^\downarrow$. In this case, Equation A.6 reduces to

$$\sigma_\varepsilon \approx \frac{1}{\sqrt{N_{tot}}}, \tag{A.7}$$

where $N_{tot} = N_R^\uparrow + N_R^\downarrow + N_L^\uparrow + N_L^\downarrow$.

The measured asymmetries (Equations A.3, A.4, and A.5) are related to the quantities in Equations A.2 as follows:

$$\begin{aligned}
\varepsilon &= PA_N[1 - 2(PA_N)\varepsilon_P\varepsilon_A] + h.o.t. && \text{(A.8)}\\
&\approx PA_N, && \text{(A.9)}\\
\varepsilon_{acc} &= \varepsilon_\Omega + (PA_N)\varepsilon_P + h.o.t. && \text{(A.10)}\\
&\approx \varepsilon_\Omega, && \text{(A.11)}\\
\varepsilon_{lum} &= \varepsilon_B + (PA_N)\varepsilon_A + h.o.t. && \text{(A.12)}\\
&\approx \varepsilon_B. && \text{(A.13)}\\
& && \text{(A.14)}
\end{aligned}$$

## A.2 Effective Analyzing Power

The analyzing power used for the AGS CNI polarimeter is based on a measurement from the E950 experiment [2]. E950 measured the analyzing power for $pC$ elastic scattering for a polarized proton beam of energy 21.7 GeV. The data from the E950 measurement are fit with theoretical constraints as described in Refer-

Table A.1: Analyzing Power used for the AGS CNI Polarimeter during the 2003 Run for $E_{beam} = 24.3$ GeV.

| $A_N^{th}$ | 0.03445 | 0.02634 | 0.02039 | 0.01605 | 0.01271 |
|---|---|---|---|---|---|
| $\|t\|$ $[(\mathrm{GeV}/c)^2]$ | 0.0030 | 0.0055 | 0.0080 | 0.0105 | 0.0130 |
| $A_N^{th}$ | 0.01001 | 0.00778 | 0.00588 | 0.00423 | 0.00280 |
| $\|t\|$ $[(\mathrm{GeV}/c)^2]$ | 0.0155 | 0.0180 | 0.0205 | 0.0230 | 0.0255 |

ence [4]. The values from this fit are extrapolated to predict the analyzing power for beam energies of 24.3 GeV and 100 GeV. The model predicts a very small beam energy dependence for energies greater than 21.7 GeV.

The theoretical value of the analyzing power at 24.3 GeV is used to determine an effective analyzing power, $\langle A_N \rangle$, for the AGS CNI polarimeter. The effective analyzing power is calculated by weighting the theoretical values by the measured event yields.

$$\langle A_N \rangle = \frac{\sum_{i=1}^{n_{bin}} (A_N^{th})_i N_i}{\sum_{i=1}^{n_{bin}} N_i}, \tag{A.15}$$

where $(A_N^{th})_i$ is the theoretical value of the analyzing power for the $i^{th}$ $-t$ bin. $N_i$ is the measured yield for the $i^{th}$ bin, and $n_{bin}$ is the number of $-t$ bins used for the measurement. The beam polarization, $P$, measured by the AGS CNI polarimeter is given by

$$P = \varepsilon / \langle A_N \rangle. \tag{A.16}$$

The theoretical values of the analyzing power and $-t$ values used for the 2003 run are displayed in Table A.1. For the 2004 run, the analyzing power calculation was revised, resulting in a $\sim 10\%$ change in the effective analyzing power. The revised analyzing power for beam energy 24.3 GeV are shown in Table A.2. The theoretical values from the fit to the E950 data for beam energy 21.7 GeV are shown in Table A.3.

Table A.2: Analyzing Power used for the AGS CNI Polarimeter during the 2004 Run for $E_{beam} = 24.3$ GeV.

| | | | | | |
|---|---|---|---|---|---|
| $A_N^{th}$ | 0.03252 | 0.04021 | 0.03778 | 0.03399 | 0.03044 |
| $\|t\|$ $[(\mathrm{GeV}/c)^2]$ | 0.001 | 0.002 | 0.003 | 0.004 | 0.005 |
| $A_N^{th}$ | 0.02734 | 0.02466 | 0.02234 | 0.02030 | 0.01849 |
| $\|t\|$ $[(\mathrm{GeV}/c)^2]$ | 0.006 | 0.007 | 0.008 | 0.009 | 0.010 |
| $A_N^{th}$ | 0.01687 | 0.01541 | 0.01407 | 0.01285 | 0.01173 |
| $\|t\|$ $[(\mathrm{GeV}/c)^2]$ | 0.011 | 0.012 | 0.013 | 0.014 | 0.015 |
| $A_N^{th}$ | 0.01069 | 0.00973 | 0.00882 | 0.00798 | 0.00719 |
| $\|t\|$ $[(\mathrm{GeV}/c)^2]$ | 0.016 | 0.017 | 0.018 | 0.019 | 0.020 |
| $A_N^{th}$ | 0.00644 | 0.00574 | 0.00507 | 0.00444 | 0.00384 |
| $\|t\|$ $[(\mathrm{GeV}/c)^2]$ | 0.021 | 0.022 | 0.023 | 0.024 | 0.025 |

Table A.3: Analyzing Power from fit to E950 Data for $E_{beam} = 21.7$ GeV.

| | | | | | |
|---|---|---|---|---|---|
| $A_N^{th}$ | 0.03248 | 0.04011 | 0.03773 | 0.03400 | 0.03049 |
| $\|t\|$ $[(\mathrm{GeV}/c)^2]$ | 0.001 | 0.002 | 0.003 | 0.004 | 0.005 |
| $A_N^{th}$ | 0.02743 | 0.02479 | 0.02249 | 0.02047 | 0.01868 |
| $\|t\|$ $[(\mathrm{GeV}/c)^2]$ | 0.006 | 0.007 | 0.008 | 0.009 | 0.010 |
| $A_N^{th}$ | 0.01708 | 0.01564 | 0.01432 | 0.01311 | 0.01201 |
| $\|t\|$ $[(\mathrm{GeV}/c)^2]$ | 0.011 | 0.012 | 0.013 | 0.014 | 0.015 |
| $A_N^{th}$ | 0.01098 | 0.01002 | 0.00913 | 0.00830 | 0.00752 |
| $\|t\|$ $[(\mathrm{GeV}/c)^2]$ | 0.016 | 0.017 | 0.018 | 0.019 | 0.020 |
| $A_N^{th}$ | 0.00678 | 0.00609 | 0.00543 | 0.00481 | 0.00422 |
| $\|t\|$ $[(\mathrm{GeV}/c)^2]$ | 0.021 | 0.022 | 0.023 | 0.024 | 0.025 |

# APPENDIX B

## Target Energy Loss Correction

The AGS CNI polarimeter was designed to detect recoil carbon nuclei of energies from a few hundred keV to about 2 MeV. At these energies multiple scattering within the carbon target can significantly effect a scattered carbon ion's energy as it escapes the target. Extremely thin targets are used in order to minimize energy loss in the target and the effects of multiple scattering. Corrections to the data to account for the energy loss in the target are made during off-line analysis.

A computer program called MSTAR is used to predict the stopping power for scattered carbon ions in the target. The MSTAR prediction is based on data for carbon ions incident on carbon targets [41]. Figure B.1 shows the predicted energy loss versus carbon energy. Using the MSTAR prediction, the total energy lost in the target can be calculated for a given path length. The typical path length for a scattered carbon ion escaping from the target is estimated to be 3.5 $\mu$g/cm$^2$. This estimate is based on a 5 $\mu$g/cm$^2$ thick target oriented at 45° with respect to the beam direction. The thickness of the target perpendicular to the beam direction is $\sim 7\mu$g/cm$^2$. The typical path length is taken to be half of this thickness. This estimate assumes that interactions with the beam occur uniformly throughout the thickness of the target. The addition of this correction causes an approximately 2% relative increase in the measured beam polarization.

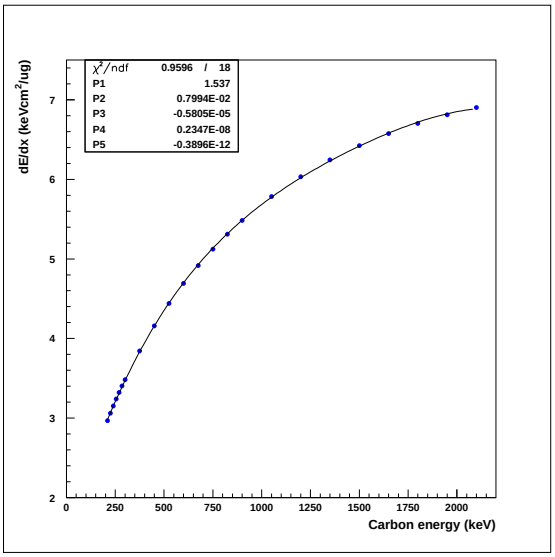


Figure B.1: Energy loss vs. kinetic energy for scattered carbon ions in carbon. The points are from MSTAR tables. The line is a fourth order polynomial fit to the points. The fit parameters are shown in the upper-left corner of the plot.

# APPENDIX C

## Tables of Measured $A_N$

The tables below contain the measured analyzing power for proton-carbon elastic scattering, $A_N$, in the Coulomb-Nuclear Interference region of momentum transfer. The first column of the tables gives the value of $-t$, the width of the $-t$ bin, and the error in $-t$, respectively. The other columns contain the value of $A_N$, the statistical error, the systematic error from the asymmetry measurement, and the error from the polarization measurement. The beam energy of the measurement is indicated in the heading of each column.

Table C.1: $A_N$ Measured during the 2004 Run at Beam Energies 3.9 GeV and 6.5 GeV.

| $-t[\times 10^{-2}]$ | $A_N[\times 10^{-2}]$ at 3.9 GeV | $A_N[\times 10^{-2}]$ at 6.5 GeV |
|---|---|---|
| 0.65 ± 0.10 ± 0.03 | 4.74 ± 0.16 ± 0.03 ± 0.30 | 3.84 ± 0.09 ± 0.03 ± 0.44 |
| 0.85 ± 0.10 ± 0.04 | 4.89 ± 0.21 ± 0.03 ± 0.31 | 3.80 ± 0.08 ± 0.03 ± 0.44 |
| 1.05 ± 0.10 ± 0.04 | 5.51 ± 0.09 ± 0.03 ± 0.35 | 3.75 ± 0.06 ± 0.03 ± 0.43 |
| 1.30 ± 0.15 ± 0.05 | 5.75 ± 0.08 ± 0.04 ± 0.37 | 3.85 ± 0.05 ± 0.03 ± 0.44 |
| 1.65 ± 0.20 ± 0.06 | 5.96 ± 0.05 ± 0.04 ± 0.38 | 3.75 ± 0.05 ± 0.03 ± 0.43 |
| 2.10 ± 0.25 ± 0.06 | 6.25 ± 0.06 ± 0.04 ± 0.40 | 3.82 ± 0.05 ± 0.03 ± 0.44 |
| 2.57 ± 0.22 ± 0.06 | 6.41 ± 0.07 ± 0.04 ± 0.41 | 3.87 ± 0.08 ± 0.03 ± 0.45 |
| 3.07 ± 0.28 ± 0.07 | 6.57 ± 0.06 ± 0.04 ± 0.42 | 3.66 ± 0.07 ± 0.03 ± 0.42 |
| 3.63 ± 0.28 ± 0.07 | | 3.60 ± 0.09 ± 0.03 ± 0.42 |
| 4.19 ± 0.28 ± 0.07 | | 3.39 ± 0.13 ± 0.03 ± 0.39 |

Table C.2: $A_N$ Measured during the 2004 Run at Beam Energies 16.0 GeV and 24.3 GeV.

| $-t[\times 10^{-2}]$ | $A_N[\times 10^{-2}]$ at 16.0 GeV | $A_N[\times 10^{-2}]$ at 24.3 GeV |
|---|---|---|
| 0.65 ± 0.10 ± 0.03 | 1.95 ± 0.16 ± 0.06 ± 0.31 | 1.97 ± 0.07 ± 0.13 ± 0.41 |
| 0.85 ± 0.10 ± 0.04 | 2.01 ± 0.15 ± 0.06 ± 0.32 | 1.54 ± 0.07 ± 0.10 ± 0.32 |
| 1.05 ± 0.10 ± 0.04 | 1.76 ± 0.10 ± 0.05 ± 0.28 | 1.43 ± 0.04 ± 0.04 ± 0.30 |
| 1.30 ± 0.15 ± 0.05 | 1.55 ± 0.08 ± 0.05 ± 0.25 | 1.22 ± 0.04 ± 0.03 ± 0.25 |
| 1.65 ± 0.20 ± 0.06 | 1.29 ± 0.05 ± 0.04 ± 0.21 | 1.17 ± 0.03 ± 0.03 ± 0.24 |
| 2.10 ± 0.25 ± 0.06 | 1.11 ± 0.05 ± 0.03 ± 0.18 | 0.81 ± 0.03 ± 0.02 ± 0.17 |
| 2.57 ± 0.22 ± 0.06 | 1.00 ± 0.06 ± 0.03 ± 0.16 | 0.52 ± 0.04 ± 0.01 ± 0.11 |
| 3.07 ± 0.28 ± 0.07 | 0.64 ± 0.07 ± 0.02 ± 0.10 | 0.26 ± 0.04 ± 0.01 ± 0.05 |
| 3.63 ± 0.28 ± 0.07 | 0.60 ± 0.08 ± 0.05 ± 0.10 | 0.07 ± 0.04 ± 0.02 ± 0.01 |
| 4.19 ± 0.28 ± 0.07 | 0.28 ± 0.12 ± 0.03 ± 0.05 | -0.13 ± 0.07 ± 0.05 ± 0.03 |
| 5.03 ± 0.56 ± 0.06 | | -0.52 ± 0.07 ± 0.19 ± 0.11 |

Table C.3: $A_N$ Measured during the 2003 Run at Beam Energies 3.9 GeV and 6.5 GeV.

| $-t[\times 10^{-2}]$ | $A_N[\times 10^{-2}]$ at 3.9 GeV | $A_N[\times 10^{-2}]$ at 6.5 GeV |
|---|---|---|
| 0.65 ± 0.10 ± 0.03 | 4.80 ± 0.07 ± 0.04 ± 0.31 | 3.46 ± 0.05 ± 0.02 ± 0.40 |
| 0.85 ± 0.10 ± 0.04 | 5.27 ± 0.07 ± 0.05 ± 0.34 | 3.63 ± 0.05 ± 0.02 ± 0.42 |
| 1.05 ± 0.10 ± 0.04 | 5.45 ± 0.06 ± 0.05 ± 0.35 | 3.51 ± 0.04 ± 0.02 ± 0.41 |
| 1.30 ± 0.15 ± 0.05 | 5.71 ± 0.05 ± 0.05 ± 0.36 | 3.54 ± 0.03 ± 0.02 ± 0.41 |
| 1.65 ± 0.20 ± 0.06 | 6.04 ± 0.05 ± 0.05 ± 0.38 | 3.51 ± 0.03 ± 0.02 ± 0.41 |
| 2.10 ± 0.25 ± 0.06 | 6.37 ± 0.05 ± 0.06 ± 0.41 | 3.66 ± 0.03 ± 0.02 ± 0.42 |
| 2.57 ± 0.22 ± 0.06 | 6.73 ± 0.12 ± 0.06 ± 0.43 | 3.53 ± 0.06 ± 0.02 ± 0.41 |
| 3.07 ± 0.28 ± 0.07 | 6.68 ± 0.13 ± 0.06 ± 0.43 | 3.51 ± 0.06 ± 0.02 ± 0.41 |
| 3.63 ± 0.28 ± 0.07 | | 3.40 ± 0.07 ± 0.02 ± 0.39 |

Table C.4: $A_N$ Measured during the 2003 Run at Beam Energies 21.7 GeV and 24.3 GeV.

| $-t[\times 10^{-2}]$ | $A_N[\times 10^{-2}]$ at 21.7 GeV | $A_N[\times 10^{-2}]$ at 24.3 GeV |
|---|---|---|
| 0.65 ± 0.10 ± 0.03 | 1.90 ± 0.05 ± 0.14 ± 0.37 | 1.79 ± 0.09 ± 0.11 ± 0.41 |
| 0.85 ± 0.10 ± 0.04 | 1.57 ± 0.04 ± 0.04 ± 0.30 | 1.66 ± 0.08 ± 0.10 ± 0.38 |
| 1.05 ± 0.10 ± 0.04 | 1.45 ± 0.04 ± 0.04 ± 0.28 | 1.46 ± 0.08 ± 0.09 ± 0.33 |
| 1.30 ± 0.15 ± 0.05 | 1.27 ± 0.04 ± 0.03 ± 0.25 | 1.18 ± 0.07 ± 0.07 ± 0.27 |
| 1.65 ± 0.20 ± 0.06 | 0.99 ± 0.03 ± 0.03 ± 0.19 | 0.97 ± 0.07 ± 0.06 ± 0.22 |
| 2.10 ± 0.25 ± 0.06 | 0.76 ± 0.03 ± 0.02 ± 0.15 | 0.69 ± 0.07 ± 0.04 ± 0.16 |
| 2.57 ± 0.22 ± 0.06 | 0.58 ± 0.06 ± 0.01 ± 0.11 | |
| 3.07 ± 0.28 ± 0.07 | 0.27 ± 0.07 ± 0.03 ± 0.05 | |
| 3.63 ± 0.28 ± 0.07 | 0.16 ± 0.10 ± 0.02 ± 0.03 | |
| 4.19 ± 0.28 ± 0.07 | -0.05 ± 0.12 ± 0.14 ± 0.01 | |

# References


[1] E. Hughes and R. Voss. *Annu. Rev. Nucl. Part. Sci.* **49**, 303 (1999).

[2] J. Tojo, et al. *Phys. Rev. Lett.* **89**, 052302 (2002) [arXiv:hep-ex/0206057].

[3] O. Jinnouchi, et al. BNL C-AD note C-A/AP/171 (2004).

[4] T.L. Trueman. hep-ph/0305085 (2003).

[5] B.Z. Kopeliovich and B.G. Zakharov. *Phys. Lett. B* **226**, 156 (1989).

[6] O. Jinnouchi. $X^{th}$ *Workshop on High Energy Spin Physics* Conf. Proc. (2003).

[7] C. Bourrely, E. Leader and J. Soffer. *Phys. Rep.* **59**, 95 (1980).

[8] P.D.B. Collins. *An Introduction to Regge Theory and High Energy Physics* Cambridge University Press, Cambridge (1977).

[9] N. Akchurin, et al. *Phys. Rev. D* **48**, 3026 (1993).

[10] N.H. Buttimore, E. Gotsman and E. Leader. *Phys. Rev. D* **18**, 694 (1978).

[11] M. Jacob and G.C. Wick. *Annals Phys.* **7**, 404 (1959).

[12] R. Cahn. *Z. Phys. C* **15**, 253 (1982).

[13] N.H. Buttimore, et al. *Phys Rev. D* **59**, 114010 (1999).

[14] N. Akchurin, et al. *Phys. Lett.* **29B**, 299 (1989).

[15] J.H. Snyder, et al. *Phys. Rev. Lett.* **41**, 781 (1978).

[16] M. Corcoran, et al. *Phys. Rev. D* **22**, 2624 (1980).

[17] G. Fidecaro, et al. *Phys. Lett.* **76B**, 369 (1978); G. Fidecaro, et al. *ibid.* **105B**, 309 (1981).

[18] B.Z. Kopeliovich and T.L. Trueman. *Phys. Rev. D* **64**, 034004 (2001).

[19] E.L. Berger, A.C. Irving, and C. Sorensen. *Phys. Rev. D* **17**, 2971 (1978).

[20] B.Z. Kopeliovich and A.V. Tarasov. *Phys. Lett. B* **497**, 44 (2001).

[21] J. Tojo. PhD thesis, Kyoto University (2004).

[22] C. Bourrely, J. Soffer, and D. Wray. *Nucl. Phys.* **B91**, 33 (1975).

[23] P.G. Sona. *Energia Nucl.* **14**, 295 (1967).

[24] A.R. Berdoz, et al. *Phys. Rev. Lett.* **87**, 272301 (2001).

[25] S.D. Reitzner. MSc thesis, University of Manitoba (1996).

[26] T. Takeuchi, et al. RHIC Spin Note AGS/RHIC/SN No. 077 (1998).

[27] L.H. Thomas. *Philos. Mag.* **3**, 1 (1927); V. Bargmann, L. Michel and V.L. Telegdi. *Phys. Rev. Lett.* **2**, 435 (1959).

[28] H. Huang, et al. *Phys. Rev. Lett.* **73**, 2982 (1994).

[29] M. Froissart and R. Stora. *Nucl. Instrum. Meth.* **7**, 297 (1960).

[30] M. Bai, et al. *Phys. Rev. Lett.* **80**, 4673 (1998).

[31] V.H. Ranjbar, et al. *Phys. Rev. STAB* **7**, 051001 (2004).

[32] H. Huang, et al. *Workshop on Increasing the AGS Polarization* AIP Conf. Proc. **667**, 40 (2003).

[33] C.E. Allgower, et al. *Phys. Rev. D* **65**, 092008 (2002).

[34] H. Huang, R. Cadman, H. Spinka, and D. Underwood. BNL C-AD Note C-A/AP/93 (2003).

[35] H. Spinka, et al. *Nucl. Instrum. Methods* **211**, 239 (1983).

[36] H. Spinka, et al. BNL C-AD Note C-A/AP/108 (2003).

[37] S.Y. Lee and E.D. Courant. RHIC Note AD/RHIC-63 (1990).

[38] W.R. Lozowski and J.D. Hudson. *Nucl. Instrum. Meth. A* **303**, 34 (1991).

[39] C.J.S. Damerell. Rutherford Appleton Laboratory Preprints RAL-P-95-008 (1995).

[40] D. Svirida, et al. *Spin 2004, 16th International Spin Physics Symposium* Conf. Proc. (2004).

[41] H. Paul and A. Schinner. *Nucl. Instrum. Meth. B* **195**, 166-174 (2002). [Online] Available: http://www.exphys.uni-linz.ac.at/Stopping/MstarWWW/MSTARInstr.htm.

[42] M.J. Berger, J.S. Coursey, and M.A. Zucker. (2000), *ESTAR, PSTAR, and ASTAR: Computer Programs for Calculating Stopping-Power and Range Tables for Electrons, Protons, and Helium Ions* (version 1.2.2). [Online] Available: http://physics.nist.gov/Star [2004, July 14]. National Institute of Standards and Technology, Gaithersburg, MD.

[43] H. Spinka, et al. BNL C-AD Note to be filed (2005).

[44] H. Spinka. Argonne Nat. Lab. Report ANL-HEP-PR-80-02 (1980).